

Yiming Abulaiti

Search for Pair-Produced Supersymmetric Top Quark
Partners with the ATLAS Experiment



Department of Physics
Stockholm University

2016

Doctoral Dissertation 2016
Department of Physics
Stockholm University
Roslagstullsbacken 21
106 91 Stockholm

© Yiming Abulaiti, Stockholm University 2016
Cover image: Timothy Tompkins, Super Collider
ISBN 978-91-7649-475-2
Printer: Holmbergs, Malmö 2016
Distributor: Department of Physics, Stockholm University

Abstract

Searches for the supersymmetric partner of the top quark (stop) are motivated by natural supersymmetry, where the stop has to be light to cancel the large radiative corrections to the Higgs boson mass. This thesis presents three different searches for the stop at $\sqrt{s} = 8$ TeV and $\sqrt{s} = 13$ TeV using data from the ATLAS experiment at CERN's Large Hadron Collider. The thesis also includes a study of the primary vertex reconstruction performance in data and simulation at $\sqrt{s} = 7$ TeV using $t\bar{t}$ and Z events. All stop searches presented are carried out in final states with a single lepton, four or more jets and large missing transverse energy. A search for direct stop pair production is conducted with 20.3 fb^{-1} of data at a center-of-mass energy of $\sqrt{s} = 8$ TeV. Several stop decay scenarios are considered, including those to a top quark and the lightest neutralino and to a bottom quark and the lightest chargino. The sensitivity of the analysis is also studied in the context of various phenomenological MSSM models in which more complex decay scenarios can be present. Two different analyses are carried out at $\sqrt{s} = 13$ TeV. The first one is a search for both gluino-mediated and direct stop pair production with 3.2 fb^{-1} of data while the second one is a search for direct stop pair production with 13.2 fb^{-1} of data in the decay scenario to a bottom quark and the lightest chargino. The results of the analyses show no significant excess over the Standard Model predictions in the observed data. Consequently, exclusion limits are set at 95% CL on the masses of the stop and the lightest neutralino.

Sammanfattning

Sökandet efter den supersymmetriska partnern till toppkvarken (stop) är motiverat av så kallade naturliga supersymmetriska modeller, där stop måste vara lätt för att upphäva de betydande korrektionerna till Higgsbosonens massa. I den här avhandlingen presenteras tre olika analyser som söker efter stop vid både $\sqrt{s} = 8$ TeV och $\sqrt{s} = 13$ TeV med data från ATLAS-experimentet vid CERN:s stora hadronkolliderare LHC. Avhandlingen inkluderar också en studie av prestandan hos den algoritm som rekonstruerar kollisionspunkten, utförd vid $\sqrt{s} = 7$ TeV i både data och simulerade kollisioner som innehåller ett $t\bar{t}$ -par eller en Z-boson. De sökningar efter stop som presenteras i avhandlingen är alla utförda i kanaler där sluttillståndet utgörs av en laddad lepton, fyra eller fler jets och en stor obalans i den transversella energin. En sökning efter direkt produktion av stop är utförd med en datamängd som svarar mot 20.3 fb^{-1} vid $\sqrt{s} = 8$ TeV. Analysen inkluderar flera olika sönderfallskanaler, bl.a. den där stop sönderfaller till en toppkvark och den lättaste neutralinon samt den där stop sönderfaller till en bottenkvark och den lättaste charginon. Analysens känslighet för olika fenomenologiska MSSM-modeller, där mer komplexa sönderfallskanaler kan förekomma, undersöks också. Två olika analyser är utförda med data vid $\sqrt{s} = 13$ TeV. Den första är en sökning efter både stop-produktion via gluoner och direkt stop-produktion med en datamängd motsvarande 3.2 fb^{-1} , medan den andra är en sökning efter direkt stop-produktion i kanalen där stop sönderfaller till en bottenkvark och den lättaste charginon med data som svarar mot 13.2 fb^{-1} . Resultaten visar inga överskott av kollisioner i data med avseende på bakgrunden från processer i Standardmodellen. Datan används därmed för att erhålla nedre gränser på stop- och netralinomassorna som svarar mot 95%-iga konfidensintervall.

Contents

Acknowledgements	1
Preface	5
About this Thesis	5
Author's Contributions	7
 I Theoretical Overview	 9
 1 The Standard Model	 11
1.1 Elementary Particles of the Standard Model	11
1.1.1 Leptons	12
1.1.2 Quarks	13
1.1.3 Gauge Bosons	13
1.1.4 Higgs Boson	13
1.2 Fundamental Interactions of the Standard Model	14
1.2.1 Electromagnetic and Weak Interactions	14
1.2.2 Strong Interaction	14
1.3 Higgs Mechanism	14
1.4 Limitations of the Standard Model	14
 2 Supersymmetry	 17
2.1 Introduction	17
2.2 Minimal Supersymmetric Standard Model	18
2.3 Soft Breaking of Supersymmetry	19
2.4 Mass Spectrum of Supersymmetric Particles	20
2.4.1 Neutralinos and Charginos	20
2.4.2 Top Squark	21
2.5 Minimal Supergravity	21
2.6 Simplified Stop Models	22
2.6.1 Direct Stop Pair Production	22
2.6.2 Gluino-Mediated Stop Production	24
2.7 Phenomenological MSSM Models	25
2.7.1 pMSSM Models with Fixed Stop and LSP Masses	25
2.7.2 3 rd Generation-Enriched pMSSM Models	26

2.7.3	General pMSSM Models	30
2.8	Sparticle Pair Production Cross Sections in pp Collisions	31
2.9	Search for Supersymmetry at ATLAS	31
II	Experimental Overview	37
3	The Large Hadron Collider	39
3.1	LHC and the Accelerator Chain	39
3.2	LHC Parameters	40
3.2.1	Center of Mass Energy and Luminosity	40
3.2.2	Pileup Conditions	43
4	The ATLAS Detector	45
4.1	Detector Overview	45
4.2	ATLAS Coordinate System	47
4.3	Inner Detector	48
4.4	Calorimeters	51
4.5	Muon Spectrometer	52
4.6	Trigger and Data Acquisition	53
5	Data Sets and Simulated Samples	55
5.1	Data Sets	55
5.2	Monte Carlo Simulation	56
5.2.1	Standard Models Samples	56
5.2.2	Signal Samples	57
6	Event Reconstruction	59
6.1	Tracks	59
6.2	Primary Vertex	60
6.3	Jets	61
6.4	Electrons	62
6.5	Muons	63
6.6	Hadronically Decaying τ Leptons	63
6.7	Photons	63
6.8	Missing Transverse Energy	64
6.9	Overlap Removal	64
III	Primary Vertex Studies	67
7	Primary Vertex Reconstruction Performance in Dimuon Events	69
7.1	Vertex Classification Methods	69

7.1.1	The Dimuon Method	69
7.1.2	The Truth-Matching Method	70
7.2	Object and Event Selection	71
7.2.1	Jet Selection	71
7.2.2	Muon Selection	71
7.2.3	$t\bar{t}$ Event Selection	72
7.2.4	Z Event Selection	72
7.3	Comparison of the Dimuon and Truth-Matching Methods	73
7.4	Results	75
7.4.1	$t\bar{t}$ Events	76
7.4.2	Z Events	76
7.5	Conclusions	76

IV Search for the Supersymmetric Partner of the Top Quark in Final States with One Isolated Lepton 79

8	Analysis Strategies and Methods	81
8.1	Analysis Strategies	81
8.2	Discriminating Variables	82
8.3	Signal, Control and Validation Regions	85
8.4	Background Estimation Techniques	86
8.5	Statistical Methods	87
9	Search for Direct Stop Pair Production with Run 1 Data	91
9.1	Signal Models and Analysis Strategies	91
9.2	Event Selection	92
9.2.1	Preselection Criteria	92
9.2.2	Signal Regions	93
9.3	Control and Validation Regions	98
9.4	Systematic Uncertainties	99
9.5	Results	101
9.6	Conclusion	104
10	Interpretation of the Stop Search Results in the pMSSM	107
10.1	Signal Models and Analysis Strategies	108
10.2	Analysis Methods	108
10.2.1	Reco-Level Analysis	108
10.2.2	Truth-Level Analysis	108
10.3	Validation of the Truth-Level Analysis Method	110
10.4	Results	111
10.4.1	Branching Ratio Dependence of the Stop Search	111

10.4.2	Interpretation in the 3 rd Generation-Enriched pMSSM Models .	112
10.4.3	Interpretation in the General pMSSM Models	115
10.5	Conclusions	122
11	Search for Gluino-Mediated and Direct Stop Pair Production with Run 2 Data	123
11.1	Signal Models and Analysis Strategies	123
11.2	Event Selection	124
11.2.1	Preselection Criteria	124
11.2.2	Signal Regions	124
11.3	Control and Validation Regions	125
11.4	Systematic Uncertainties	129
11.4.1	Experimental Uncertainties	129
11.4.2	Theoretical Uncertainties	129
11.5	Results	133
11.6	Conclusions	135
12	Search for Direct Stop Production with Run 2 Data	137
12.1	Signal Models and Analysis Strategies	137
12.2	Event Selection	138
12.2.1	Preselection Criteria	138
12.2.2	Signal Regions	138
12.3	Control and Validation Regions	138
12.3.1	$t\bar{t}$ Control Regions	138
12.3.2	Single top Wt Control Regions	139
12.3.3	W +jets Control Regions	140
12.3.4	$t\bar{t} + Z$ Control Regions	141
12.3.5	Validation Regions	141
12.4	Systematic Uncertainties	142
12.5	Results	142
12.6	Conclusions	143
	Conclusions	147
	Bibliography	149

Acknowledgements

Firstly, I would like to express my special appreciation and thanks to my advisor Sara Strandberg. Sara, you guided me during all the time of my research and writing of this thesis. Without your continuous support throughout my Ph.D. studies, this thesis would not be completed. I would like to thank you for encouraging me to grow as a research scientist. I would also like to thank my second supervisor Kerstin Jon-And who always supported me during my work.

I would like to thank the entire ATLAS group at Stockholm University. All of you have been there to help me when I needed it. Many thanks to Sten Hellman, David Milstead, Christophe Clément, Torbjörn Moa, Barbro Åsman, Jörgen Sjölin, Hyeon Jin Kim, Hovhannes Khandanyan, Valerio Rossetti, Ruth Pöttgen, Priscilla Pani, Michaël Ughetto, Karl Gellerstedt. I also would like to thank the IceCube group members, Per-Olof Hulth, Christian Walck, Klas Hultqvist, Chad Finley, and Jonathan Dumm.

Many thanks to the stop one lepton research group at CERN for their help with my studies and my work. I have had a great time working with you.

I would like to thank Pawel Klimek, Katarina Bendtz, Olle Lundberg, Simon Molander. I appreciated your help. Apart from them, I would like to thank the rest of my fellow Ph.D. students both from the ATLAS and IceCube groups, Christian Ohm, Olga Bessidskaia Bylund, Wayne Cribbs, Gabriele Bertoli, Anna Shcherbakova and Nabila Shaikh, Marcel Zoll, Samuel Flis, Martin Wolf and Maryon Ahrens.

Finally, special thanks to my family, Mom, Dad, and my true love and wife Mainur and my lovely daughter Minever. Many thanks for the support and the sacrifices that you have made on my behalf. Without your encouragement and sacrifices, I would not have crossed the long distance to study in Stockholm. No words can express how grateful I am to you.

List of Acronyms

ALICE	A Large Ion Collider Experiment
ATLAS	A Toroidal LHC Apparatus
BDT	Boosted Decision Tree
BR	Branching Ratio
BSM	Beyond the Standard Model of particle physics
CB	Combined Muon
CL	Confidence Level
CMS	Compact Muon Solenoid
CL_s	Statistical method for setting upper limits
CR	Control Region
CSC	Cathode Strip Chamber
CT	Calorimeter-Tagged muons
DCS	Detector Control System
EM	ElectroMagnetic
EW	ElectroWeak interaction
FCal	Forward Calorimeter
FCNC	Flavor-Changing Neutral Current
FSR	Final State Radiation
GUT	Grand Unified Theory
HEC	Hadronic End-cap Calorimeter
HLT	Highly Level Trigger
IBL	Insertable B-Layer
ID	Inner Detector
IP	Interaction Point
ISR	Initial State Radiation
JER	Jet Energy Resolution
JES	Jet Energy Scale
JVT	Jet Vertex Fraction
L1	Level 1 (trigger)
L2	Level 2 (trigger)
LAr	The (ATLAS) Liquid Argon (electromagnetic) calorimeter
LEP	Large Electron-Positron collider
LHC	Large Hadron Collider
LHCb	Large Hadron Collider beauty
LINAC 2	Linear Accelerator 2
LO	Leading Order
LSP	Lightest Supersymmetric Particle
MC	Monte Carlo
MDT	Monitored Drift Tube
MS	Muon Spectrometer
MSSM	Minimal Supersymmetric Standard Model
mSUGRA	minimal SuperGravity
NLL	Next-to-Leading-Logarithm
NLO	Next-to Leading Order
NNLL	Next-to-Next-to-Leading-Logarithm
NNLO	Next-to-Next-to Leading Order
OR	Overlap Removal
PDF	Parton Distribution Function
pMSSM	phenomenological MSSM
PS	Proton Synchrotron
PSB	Proton Synchrotron Booter

QCD	Quantum ChromoDynamics
QED	Quantum ElectroDynamics
RoI	Region of Interest (trigger)
SA	Stand-Alone muons
SCT	SemiConductor Tracker
SM	Standard Model
SPS	Super Proton Synchrotron
SR	Signal Region
ST	Segment-Tagged muons
STCR	Single-Top Wt Control Region
Stop	Supersymmetric partner of the top quark
SUSY	Supersymmetry
TCR	Top Control Region
TDAQ	Trigger and Data Acquisition
TF	Transfer Factor
TRT	Transition Radiation Tracker
TVR	Top Validation Region
UL	Upper Limit
VR	Validation Region
WCR	W +jets Control Region
WVR	W +jets Validation Region

Preface

The constituents of the universe that we have observed so far are fundamental particles grouped into so-called leptons, quarks and bosons. The Standard Model of particle physics (SM) is built to describe the properties of these particles and the relations between them. The SM does not only describe the fundamental properties of the particles but has also made many precise predictions which have already been tested in collider experiments to very high accuracy. The most prominent example is the discovery of the Higgs boson which was predicted by the SM, at the Large Hadron Collider (LHC) experiments in 2012.

However, not all phenomena are described by the SM. One of its limitations is that it does not include gravity. Furthermore, it does not contain or predict any dark matter candidate. From the theoretical point of view, the mass hierarchy of the Higgs boson does not have a natural explanation in the SM.

To address the limitations of the SM, various new theoretical frameworks of so-called beyond the Standard Model physics are developed. Among them, the supersymmetric extension of the Standard Model is one of the best-studied examples of such a model. The supersymmetric Standard Model does not only solve several of the SM shortcomings but also makes many predictions that can be tested at collider and non-collider experiments.

In 2011 and 2012, the LHC operated at a center of mass energy of $\sqrt{s} = 7$ TeV and $\sqrt{s} = 8$ TeV respectively, and is now operated at $\sqrt{s} = 13$ TeV since 2015. During this time, the two general purpose detectors, ATLAS and CMS, have collected proton-proton collision data for a variety of physics programs including the searches for supersymmetric particles. If particles beyond the Standard Model exist at the available energy scale (\sim TeV), the LHC experiments should be able to find them.

About this Thesis

The thesis consists of four parts. Part I describes the theory of particle physics. Chapter 1 introduces the Standard Model of particle physics and its limitations. Chapter 2 presents the theory of supersymmetry, and describes the supersymmetric models which are considered in the searches in this thesis.

Part II describes the experimental facilities. Chapter 3 describes the LHC accelerator and its parameters. Chapter 4 describes the ATLAS experiment and its various sub-detectors. Chapter 5 describes the data and MC simulations which are used in the analyses presented in this thesis. Chapter 6 presents the methods of reconstructing physics objects such as electrons, muons, jets and missing transverse energy.

Part III consists of Chapter 7 which includes the studies of the primary vertex reconstruction performance in the ATLAS experiment. The quality of the primary vertex reconstruction is studied using pairs of muons originating from $t\bar{t}$ and Z events both in data and MC simulation.

Part IV includes searches for the supersymmetric partner of the top quark (stop). Chapter 8 describes analysis strategies and statistical methods which are commonly used in the analyses presented in this thesis. Chapter 9 describes a search for direct stop pair production using ATLAS data at $\sqrt{s} = 8$ TeV. Chapter 10 includes interpretations of the stop search in various phenomenological Minimal Supersymmetric SM (pMSSM) scenarios. Chapter 11 presents a search for both gluino-mediated and direct stop pair production with ATLAS data at $\sqrt{s} = 13$ TeV collected in 2015. Chapter 12 presents a search for direct pair-production of stops decaying into a chargino and a b quark with 2015 and 2016 data. This decay is an important example of a scenario where more than one SUSY particle has a mass below the stop mass. This decay was not considered in the previous analysis at $\sqrt{s} = 13$ TeV.

The natural units, $c = \hbar = 1$ are commonly used in elementary particle physics, where c and \hbar are the speed of light and the reduced Planck constant respectively. Under this convention, the masses and momenta of the particles have the same units as the energy, and the time and length have units that are the inverse of the energy. The same conventions are followed in this thesis.

Main publications

The author of this thesis has made significant contributions to, and is an author of, the following publications:

- ATLAS Collaboration, Search for top squark pair production in final states with one isolated lepton, jets, and missing transverse momentum in $\sqrt{s} = 8$ TeV pp collisions with the ATLAS detector, JHEP 11 (2014) 118, arXiv:1407.0583 [hep-ex] [1].
- A. Yiming, Search for top squark pair production in final states with one isolated lepton, jets, and missing transverse momentum in pp collisions with the ATLAS detector, Nuclear and Particle Physics Proceedings 273–275 (2016) 2415 – 2417 [2].
- ATLAS Collaboration, ATLAS Run 1 searches for direct pair production of third-generation squarks at the Large Hadron Collider, Eur. Phys. J. C75 (2015) no.10, 510, erratum: Eur. Phys. J.C76 (2016) no.4, 153, arXiv:1506.08616 [hep-ex] [3].

ATLAS Collaboration, Summary of the ATLAS experiment's sensitivity to supersymmetry after LHC Run 1 - interpreted in the phenomenological MSSM, JHEP 10 (2015) 134, arXiv:1508.06608 [hep-ex] [4].

ATLAS Collaboration, Search for top squarks in final states with one isolated lepton, jets, and missing transverse momentum in $\sqrt{s} = 13$ TeV pp collisions with the ATLAS detector, CERN-EP-2016-113, arXiv:1606.03903 [hep-ex], submitted to PRD [5].

Search for top squarks in final states with one isolated lepton, jets, and missing transverse momentum in $\sqrt{s} = 13$ TeV pp collisions with ATLAS data, ATLAS-CONF-2016-050 [6].

Author's Contributions

I started as a doctoral student at Stockholm University in November 2011. In the first year, I focused on the performance of the primary vertex reconstruction. I used events with two muons originating from the decay of a pair of top quarks or a Z boson to study the primary vertex reconstruction performance in both data and simulated events. This method is complementary to the standard method used in the ATLAS experiment which can only be applied to simulated events. My study is described in detail in Chapter 7 and also documented in an ATLAS internal note.

In my second year of studies, I joined the group in ATLAS searching for the supersymmetric partner of the top quark in events with one isolated lepton. Within this group, I performed a study of the sensitivity of the stop search to the pMSSM scenario. In this study, I studied the properties of a large set of pMSSM models. To address the sensitivity dependence of the analysis described in Chapter 9, I selected a total of 27 pMSSM models from a paper in which many pMSSM models were produced. In these 27 models, the stop and neutralino masses are almost identical while the branching ratios of the stop decay channels are different in each model. Then, I simulated these models using the ATLAS simulation software. Using these models, I carried out a study of the branching ratio dependence of the exclusion limits on the masses of the stop and the neutralino. The result of this study is included in [1]. I presented the results including my studies at the ICHEP 2014 conference and the poster proceedings are published in [2].

All 3rd generation squark searches in the ATLAS experiment are used to determine ATLAS' sensitivity to the 3rd generation squark enriched pMSSM as described in Chapter 10. In this context, I studied the properties of various pMSSM models. Then, from the 19-dimensional parameter space, I created well-tempered neutralino pMSSM scenarios in which each signal model satisfy the constraints from dark matter relic density measurements. This scenario became one of the 3rd generation squark-enriched pMSSM models used in [3]. In this analysis, my main task was to apply the analysis described in

Chapter 9 to all the 3rd generation squark-enriched pMSSM models and obtain the exclusion limits on each type of pMSSM scenario. The results of the analysis are included in [3].

In [4], the impact of the ATLAS SUSY searches in constraining models generated from the general phenomenological MSSM (19 parameters) is investigated (see Chapter 10). In this analysis, I performed the statistical interpretation of the analysis described in Chapter 9 in the context of the general pMSSM. A total of 500 million models, sampled from the 19-dimensional parameter space are considered. After experimental constraint have been applied, a total of 310327 models are left. These are passed through a full simulation of the ATLAS detector. My main task was the statistical interpretation of the stop search in these models. The study shows that the stop search is sensitive to several thousands of models, which are then subsequently used to derive exclusion limits. The relevant work and results are included in [4].

In 2015, with the first ATLAS Run 2 data, our analysis group performed an analysis searching for both gluino-mediated and direct stop pair production at $\sqrt{s} = 13$ TeV. As a member of the group I also contributed to the analysis. My main contribution was to estimate the theoretical systematic uncertainties on the SM backgrounds. The analysis is described in Chapter 11 and the results are included in the [5].

With the data collected up until June 2016, our team carried out an analysis searching for direct stop pair production. I am responsible for the channel in which the stop decays into a chargino and a b quark. The chargino further decays into a neutralino and a W boson. In this analysis, I optimized two signal regions. I also contributed to the background estimation by constructing the control regions for the dominant SM backgrounds. The analysis is described in Chapter 12 and the results are included in [6].

Notes

Some part of this thesis have already been published in my licentiate thesis [7].

- The theory part described in Chapters 1 and 2 are taken from my licentiate thesis with some extensions made to Chapter 2.
- Chapter 7 is published in my licentiate thesis and re-included in this thesis.
- The sensitivity studies with the 27 phenomenological MSSM models are published in my licentiate thesis. The results are also included in this thesis as a part of Chapter 10. Sections 8.2 and 8.5, describing some of the analysis methods, are also taken from my licentiate thesis with some modifications.
- Some formulas and figures from my licentiate thesis are re-used in this thesis.

Part I

Theoretical Overview

1 The Standard Model

The Standard Model [8–10] of particle physics (SM) is a theory of fundamental particles comprising electromagnetic, weak and strong nuclear interactions. It was established in the early 1970s, and describes the universe in terms of fermions and bosons. The SM explains almost all observed phenomena in particle physics and precisely predicts a wide variety of phenomena. It is the most successful theory in particle physics.

The SM is a relativistic quantum field theory [11] in which particles are quanta of their corresponding fields. Matter particles are quanta of spin $\frac{1}{2}$ fermion fields and gauge bosons are quanta of spin 1 vector fields (gauge fields). The SM theory involves the global Poincare Symmetry¹⁾ and the local $SU(3) \otimes SU(2) \otimes U_Y(1)$ ²⁾ symmetry. The strong interaction of colored particles is mathematically described by the $SU(3)$ gauge group. The $SU(2) \otimes U_Y(1)$ gauge group describes the electroweak interaction which is a unification of the electromagnetic and weak interactions.

In the SM, the $SU(2) \otimes U_Y(1)$ symmetry holds if all particles are massless. However most particles in nature are massive. Therefore the $SU(2) \otimes U_Y(1)$ symmetry is broken. The electroweak symmetry breaking in the SM occurs via the Higgs mechanism in which a massive scalar field is introduced.

However the SM is not a complete theory. The theory of gravity is for example not included in the SM and it lacks a dark matter candidate. These problems are keeping the SM from being "the theory of everything".

1.1 Elementary Particles of the Standard Model

The SM particles include 12 fermions which have $\frac{1}{2}$ -integer spin, four gauge bosons which have integer spin and a Higgs boson which is a spinless particle as shown in Table 1.1. The fermions are divided into quarks and leptons and further grouped into three generations. Each generation of quarks includes two quarks, which differ in their electric charge and mass. Each generation of leptons includes a charged lepton and an electrically neutral neutrino. Quarks and leptons are known as matter particles. Gauge bosons are referred to as force-carrying particles, responsible for the electromagnetic,

¹⁾Global Poincare symmetry is postulated for all relativistic quantum field theories.

²⁾ $SU(n)$ is the special unitary group of dimension n .

weak and strong interactions between the elementary particles.

In the SM, the fermions have their associated anti-fermions (also called anti-matter) particles. The matter and anti-matter particles have opposite charges so they can annihilate each other and also be created in pairs. The electrically neutral gauge bosons are their own anti-bosons, while the W^+ and W^- bosons are each other's anti-particles.

	Symbols	Name	Mass (MeV)	Charge (e)	Generation
Quarks (Spin = $\frac{1}{2}$)	u	up	2.3	$+\frac{2}{3}$	I
	d	down	4.8	$-\frac{1}{3}$	
	c	charm	1275	$+\frac{2}{3}$	II
	s	strange	95	$-\frac{1}{3}$	
	t	top	173.21×10^3	$+\frac{2}{3}$	III
	b	bottom	4180	$-\frac{1}{3}$	
Leptons (Spin = $\frac{1}{2}$)	ν_e	electron neutrino	$< 2 \text{ eV}$	0	I
	e	electron	0.51	-1	
	ν_μ	muon neutrino	< 0.19	0	II
	μ	muon	105.65	-1	
	ν_τ	tau neutrino	< 18.2	0	III
	τ	tau	1776.82	-1	
Gauge bosons (Spin = 1)	g	gluon	0	0	—
	γ	photon	0	0	
	W	W boson	80.38×10^3	± 1	
	Z	Z boson	91.19×10^3	0	
Higgs boson (Spin = 0)	H	Higgs boson	125.09×10^3	0	

Table 1.1: The elementary particles in the Standard Model [12].

1.1.1 Leptons

Leptons are fermions, and do not take part in the strong interaction. They can be subdivided into two classes: charged leptons and neutral leptons. The electron (e), muon (μ) and tau (τ) have electric charge $-e$, and interact via both electromagnetic and weak interactions whereas the neutrinos (ν_e , ν_μ , ν_τ) are electrically neutral and therefore only interact via the weak interaction. The electron, muon and tau are massive particles. The muon and tau have the same properties as the electron except for their larger mass. The

neutrinos are massless in the SM³⁾.

The anti-lepton of a charged lepton has the same spin and mass but is positively charged. The anti-neutrino is massless and electrically neutral like the neutrino but has opposite handedness [10]. It was in 1932 that a fermion with the same mass as the electron but with positive electric charge was experimentally discovered. It was named the positron and is the anti-particle of the electron.

1.1.2 Quarks

The six quarks, up (u), down (d), charm (c), strange (s), top (t) and bottom (b) are all massive fermions. Up, charm and top quarks carry electric charge $\frac{2}{3}e$ while down, strange and bottom quarks carry electric charge $-\frac{1}{3}e$. Unlike leptons quarks also carry the additional quantum number color charge which can take on the three values red, blue and green. Quarks participate in electromagnetic, weak and strong interactions. The isolated quarks have never been observed in nature because of color confinement which is a phenomenon implying that color charged particles cannot be isolated singularly. Naturally, they exist only in bound systems called hadrons which are color-neutral [14], either as mesons which consist of a quark and an anti-quark or as baryons which consist of three quarks. Anti-quarks have the same mass and spin as their corresponding quarks but have opposite electric and color charges.

1.1.3 Gauge Bosons

Gauge bosons are force-carrying particles which have spin 1. The four gauge bosons are the gluon (g), the photon (γ), the W boson and the Z boson. The gluon and photon are massless and electrically neutral particles, which mediate the strong nuclear and electromagnetic forces respectively. The W and Z bosons are massive and mediate the weak nuclear force. The W boson is electrically charged and exists in two variants, one with positive (W^+) and one with negative (W^-) charge. The Z boson is electrically neutral.

1.1.4 Higgs Boson

The Higgs boson is a massive spinless particle. It was theoretically predicted to be part of the SM in 1964. On 4 July 2012, the ATLAS and CMS experiments at CERN's Large Hadron Collider announced that they had each observed a new particle in the mass region around 126 GeV [15, 16]. This new particle is consistent with a SM-like Higgs boson. The Higgs boson is the only elementary scalar particle discovered in nature.

³⁾The observation of neutrino oscillations however show that neutrinos in fact do have a small mass [13].

1.2 Fundamental Interactions of the Standard Model

1.2.1 Electromagnetic and Weak Interactions

In the SM, electromagnetic and weak interactions [17] are unified into a single electroweak interaction. The gauge theory of electroweak interactions is described by a local $SU(2) \otimes U_Y(1)$ gauge group. The gauge bosons associated with the $SU(2)$ group are the W_1, W_2 and the W_3 and the gauge boson for the $U_Y(1)$ group is the B^0 , all of which are massless. In reality the $SU(2) \otimes U_Y(1)$ gauge symmetry is broken down to the $U_Q(1)$ gauge symmetry via the Higgs mechanism, where Q is the electric charge. Through the spontaneous symmetry breaking in the theory the two neutral bosons W_3 and B^0 mix to form the photon and the Z^0 , while the W_1 and W_2 mix to form the W^\pm . Through the Higgs mechanism Z and W bosons become massive while the photon remains massless since the $U_Q(1)$ gauge symmetry is unbroken.

The photon itself is electrically neutral and is mediating the electromagnetic force between electrically charged particles. The electromagnetic interaction has long (infinite) range. The weak interaction is caused by the exchange of Z and W bosons. The weak force is short-ranged because of the larger masses of Z and W bosons. All known fermions interact via the weak nuclear force.

1.2.2 Strong Interaction

The strong nuclear force acts between colored particles. It is described by Quantum Chromodynamics (QCD) [11] which is mathematically equivalent to an $SU(3)$ gauge group describing the strong interaction of colored particles. The group has eight generators since the theory has eight types of gluons. In the SM the colored particles are the quarks and gluons. The strong interaction of the quarks is mediated by gluons. The gluons are also carrying color charge, and therefore interact with each other.

1.3 Higgs Mechanism

The Higgs mechanism [18,19] is essential to formulate a theory involving massive gauge bosons. In the Higgs mechanism a complex doublet scalar field is introduced which couples to the gauge fields of the electroweak force. The non-zero vacuum energy of the scalar field causes spontaneous symmetry breaking of the theory. Three of the four degrees of freedom introduced with the doublet are absorbed by the weak gauge fields, giving masses to the W and Z bosons. The remaining degree of freedom corresponds to the Higgs field for which the quanta are the Higgs bosons.

1.4 Limitations of the Standard Model

Despite being the most successful theory in particle physics, the Standard Model is incomplete. From the point of view of phenomena, the SM describes interactions of

particles using strong, weak and electromagnetic forces while gravity is missing. Furthermore, cosmological observations of dark matter [20] and dark energy show that the SM explains only around 5% of the energy in the universe as the SM does not provide a good candidate for the dark matter. Another shortcoming is that the neutrinos in the SM are massless while neutrino oscillation experiments show that neutrinos do have mass [13]. Also, the matter/anti-matter asymmetry of the universe is not understood in the SM. Moreover according to QCD, the violation of CP symmetry exists in the strong interactions, but such phenomena have not been observed experimentally.

Another shortcoming of the SM is the need for a large fine-tuning of the Higgs boson mass. The Higgs boson mass in the SM gets large quantum corrections. In order to cancel these quantum corrections, the bare Higgs boson mass must be tuned to about the 30th decimal place, but this level of tuning is thought to be unnatural.

Because of these limitations, the most pressing issue in particle physics today is to find the correct extension of the SM.

2 Supersymmetry

2.1 Introduction

The square of the Higgs boson mass receives large radiative corrections from fermionic loop diagrams. The left diagram in Figure 2.1 shows the correction to the squared mass of the Higgs boson (Higgs squared mass) from a fermion loop. If the Higgs field (H) and the fermionic field (f) couple with a Lagrangian form, $-\lambda_f H \bar{f} f$ (where λ_f is a coupling constant), then the loop correction is

$$\Delta m_H^2 = -\frac{\|\lambda_f\|^2}{8\pi^2} \Lambda_{UV}^2 + \dots \quad (2.1)$$

where Λ_{UV} is the ultraviolet cutoff i.e. the energy scale up to which the SM is valid.

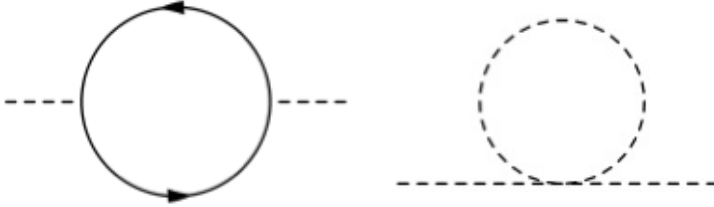


Figure 2.1: One loop quantum corrections from a fermion (left solid line) and boson (right dashed line) to the Higgs squared mass.

In the absence of new physics, Λ_{UV} can be taken to be the Planck scale, resulting in a correction to the Higgs squared mass that is of the order of Λ_{UV} itself. To get a Higgs mass of about 126 GeV there must be a cancellation between such a huge correction and the bare Higgs squared mass. This cancellation requires incredible fine-tuning of the bare Higgs squared mass which violates the naturalness [21] principle. This is commonly referred to as the hierarchy problem [22–25].

A solution to this problem is that a cancellation of the fermion-type corrections can be obtained by boson-type loop corrections [26–31] (right diagram of Figure 2.1). If the

bosonic field (S) couples to the Higgs field in the form of $-\lambda_S \|H\|^2 \|S\|^2$ (where λ_S is a coupling constant), then the radiative correction from the boson-type loop diagrams is

$$\Delta m_H^2 = \frac{\lambda_S}{16\pi^2} [\Lambda_{UV}^2 - 2m_S^2 \ln(\Lambda_{UV}/m_s) + \dots]. \quad (2.2)$$

The quadratically divergent part of the corrections from the fermion and boson loop diagrams cancel each other if $\lambda_S = \lambda_f^2$. This type of cancellation is automatic if a new symmetry relating the fermions and bosons, called supersymmetry (SUSY) [32–40], is introduced.

Supersymmetry is a theoretical extension of the SM based on the supersymmetric transformation between fermions and bosons. The supersymmetric transformations transform particles into supersymmetric particles. The particles and their supersymmetric partners are referred to as each other's superpartners. The superpartners of fermions are spinless particles called scalar fermions (sfermions). The superpartners of gauge bosons are spin $\frac{1}{2}$ particles called gauginos. The superpartner of the Higgs boson is also a spin $\frac{1}{2}$ particle called the Higgsino.

If supersymmetry holds between the particle and its superpartner then they must have the same mass. E.g. if a superpartner of the electron exists, it must have a mass that is equal to the electron mass. Since no such particle has been found, supersymmetry must be broken. The supersymmetry breaking terms are explicitly added to the supersymmetric model.

2.2 Minimal Supersymmetric Standard Model

One carefully studied supersymmetric model is the Minimal Supersymmetric Standard Model (MSSM) [41], which is a minimal phenomenologically viable supersymmetric model. The MSSM predicts that all the elementary particles of the SM have their corresponding superpartners (see Table 2.1).

In the MSSM, the electroweak symmetry breaking is more complicated than in the SM. The Higgs mechanism contains two complex Higgs doublets, $H_u = (H_u^+, H_u^0)$ and $H_d = (H_d^-, H_d^0)$, which have a total of eight degrees of freedom and non-zero vacuum expectation values. In the spontaneous electroweak symmetry breaking three degrees of freedom give the masses to the weak gauge bosons, while five degrees of freedom correspond to the five mass eigenstates of the Higgs bosons: two CP -even electrically neutral scalars h^0 and H^0 , one CP -odd electrically neutral scalar A^0 , and two electrically charged scalars H^\pm . The h^0 is lighter than the others and has properties similar to the Higgs boson in the SM.

In the MSSM supersymmetry is related to a new conserved quantity, named R parity (P_R). The P_R is defined as

$$P_R = (-1)^{2S+3(B-L)}, \quad (2.3)$$

SM particle	Spin	superpartner	Spin
l (lepton) q (quark)	$\frac{1}{2}$	\tilde{l} (slepton) \tilde{q} (squark)	0
B^0 (B boson) W_1, W_2, W_3 (W bosons) g (gluon)	1	\tilde{B} (bino) $\tilde{W}_1, \tilde{W}_2, \tilde{W}_3$ (winos) \tilde{g} (gluino)	$\frac{1}{2}$
$H_u^+, H_u^0, H_d^-, H_d^0$ (Higgs bosons)	0	$\tilde{H}_u^+, \tilde{H}_u^0, \tilde{H}_d^-, \tilde{H}_d^0$ (Higgsinos)	$\frac{1}{2}$

Table 2.1: Superpartners of the SM particles in the MSSM. The B^0 and $W_{1,2,3}$ are the gauge eigenstates which correspond to the $U(1)$ and $SU(2)$ local gauge symmetry respectively.

where S is the spin, B is the baryon number and L is the lepton number. In the R-parity conserved MSSM models the supersymmetric particles are always produced in pairs and they decay into lighter supersymmetric particles plus the SM particles. The lightest supersymmetric particle (the LSP) is stable and thought to be a candidate of dark matter. Thus, supersymmetry does not only provide a solution to the hierarchy problem but also provides solutions to other problems like the origin of the dark matter.

2.3 Soft Breaking of Supersymmetry

As discussed above, supersymmetry is explicitly broken by introducing soft breaking terms into the supersymmetry Lagrangian. In the MSSM the Lagrangian can be written as

$$\mathcal{L} = \mathcal{L}_{\text{SUSY}} + \mathcal{L}_{\text{soft}} \quad (2.4)$$

Here $\mathcal{L}_{\text{SUSY}}$ is invariant under supersymmetric transformation while $\mathcal{L}_{\text{soft}}$ violates supersymmetry. The soft breaking terms include only sfermions and gauginos, not their superpartners. If m_{soft} is the largest mass scale in the soft breaking terms, the remaining radiative correction to the Higgs squared mass is

$$\Delta m_H^2 = m_{\text{soft}}^2 \left[\frac{\lambda}{16\pi^2} \ln(\Lambda_{UV}/m_{\text{soft}}) + \dots \right]. \quad (2.5)$$

Since the m_{soft} term is related to the mass splitting between the fermion and its superpartner, the mass splitting cannot be arbitrarily large in order to arrive at the observed Higgs boson mass.

The soft breaking terms of the MSSM introduce many new free parameters into the model, e.g. the mass terms of the gauginos, sfermions and other coupling parameters. There are in total 105 free parameters in the Lagrangian of the MSSM.

2.4 Mass Spectrum of Supersymmetric Particles

In the MSSM, the electroweak gauginos and Higgsinos mix. Their masses are given in terms of mass matrices. However these mass matrices can be diagonalized using unitary matrices. The diagonal elements are the physical masses of the particles. This means that the electroweak gauginos and Higgsinos can be transformed into mass eigenstates. The mass eigenstates are the neutralinos which are mixed states of the electrically neutral Higgsinos, the electrically neutral wino and the bino, and the charginos which are mixed states of the electrically charged Higgsinos and winos. The neutralinos and charginos are described in Section 2.4.1 in more detail.

The mass eigenstates of the sfermions are also mixed states of the supersymmetric partners of the left- and right-handed fermions (referred to as left- and right-handed sfermions). The mixing matrices are unitary matrices which can diagonalize the mass matrices of the left- and right-handed sfermions. As an example the top squark mixing is given in Section 2.4.2.

2.4.1 Neutralinos and Charginos

The neutralino mixing [42] is described by a $N(4 \times 4)$ unitary matrix as shown in Equation 2.6. There are four neutralinos ($\tilde{\chi}_i^0$) which are electrically neutral fermions. The $\tilde{\chi}_1^0$ is the lightest one ($m_{\tilde{\chi}_1^0} < m_{\tilde{\chi}_2^0} < m_{\tilde{\chi}_3^0} < m_{\tilde{\chi}_4^0}$). Therefore in the R-parity conserved MSSM, it is the LSP and thought to be the candidate of the dark matter [43, 44].

$$\begin{pmatrix} \tilde{\chi}_1^0 \\ \tilde{\chi}_2^0 \\ \tilde{\chi}_3^0 \\ \tilde{\chi}_4^0 \end{pmatrix} = N(4 \times 4) \begin{pmatrix} \tilde{B} \\ \tilde{W}^0 \\ \tilde{H}_u^0 \\ \tilde{H}_d^0 \end{pmatrix} \quad (2.6)$$

The $N(4 \times 4)$ matrix is called the neutralino mixing matrix, which rotates the gauge eigenstates (gauginos and Higgsinos) into the physical mass eigenstates. The square of the matrix element N_{ij} gives the corresponding fraction of the j th gaugino state in the i th neutralino state. e.g. the square of N_{i1} gives the bino content of $\tilde{\chi}_i^0$.

$$\begin{pmatrix} \tilde{\chi}_1^+ \\ \tilde{\chi}_2^+ \end{pmatrix} = V(2 \times 2) \begin{pmatrix} \tilde{W}^+ \\ \tilde{H}_u^+ \end{pmatrix}, \quad \begin{pmatrix} \tilde{\chi}_1^- \\ \tilde{\chi}_2^- \end{pmatrix} = U(2 \times 2) \begin{pmatrix} \tilde{W}^- \\ \tilde{H}_d^- \end{pmatrix} \quad (2.7)$$

The chargino mixing is described by the two unitary matrices $V(2 \times 2)$ and $U(2 \times 2)$ as shown in Equation 2.7. The square of the matrix elements of the unitary matrices gives

the wino content $(U \text{ or } V)_{i1}$ and the Higgsino content $(U \text{ or } V)_{i2}$, where i is 1 for $\tilde{\chi}_1^\pm$ and 2 for $\tilde{\chi}_2^\pm$.

2.4.2 Top Squark

As the top quark gives the dominant contribution to the radiative corrections to the Higgs squared mass, the supersymmetric partner of the top quark, (top squark or stop) needs to be relatively light ($\lesssim 1$ TeV [45, 46]) for SUSY to solve the hierarchy problem.

The superpartners of the left- and right-handed top quarks (\tilde{t}_L and \tilde{t}_R , referred to as left- and right-handed stops) mix into the light and heavy stops [42] (\tilde{t}_1 and \tilde{t}_2) as shown in Equation 2.8. There is a convention that $m_{\tilde{t}_1} < m_{\tilde{t}_2}$, therefore \tilde{t}_1 always denotes the lightest of the two mass eigenstates.

$$\begin{pmatrix} \tilde{t}_1 \\ \tilde{t}_2 \end{pmatrix} = \mathfrak{R}(2 \times 2) \begin{pmatrix} \tilde{t}_L \\ \tilde{t}_R \end{pmatrix} \quad (2.8)$$

The stop mixing matrix $\mathfrak{R}(2 \times 2)$ is a unitary matrix and the square of its matrix elements gives the left- or right-handed fraction of the stop mass eigenstates. E.g. the square of \mathfrak{R}_{11} gives the \tilde{t}_L fraction of the \tilde{t}_1 and the square of \mathfrak{R}_{12} gives the \tilde{t}_R fraction of the \tilde{t}_1 . If \mathfrak{R}_{11} is equal to 1, the light stop is purely the partner of the left-handed top quark.

2.5 Minimal Supergravity

In the minimal supergravity model [47, 48] (mSUGRA), many free parameters of the MSSM are related to basic parameters at the Grand Unification (GUT) scale. The symmetry in this model is broken via the super-Higgs mechanism which is called gravity-mediated SUSY breaking in a hidden sector of SUSY. The theoretical assumption of this model is the GUT scale universality which assumes all scalars to have a common mass m_0 , all gauginos to have a common mass $m_{1/2}$, the theory to have a common trilinear scalar coupling A_0 , the superpotential Higgs mass parameter μ , and a bilinear mass term B . The soft SUSY-breaking parameters are evaluated from the GUT scale down to the electroweak scale using renormalization group equations.

Taking the radiative electroweak symmetry breaking into account, only five independent free parameters are left in the theory. The five parameters are m_0 , $m_{1/2}$, A_0 , $\tan\beta$ and $\text{sign}(\mu)$. The parameter B can be determined from $\tan\beta$ which is the ratio of the two Higgs vacuum expectation values. The parameter $|\mu|$ can also be determined but its sign remains free.

2.6 Simplified Stop Models

Simplified models are built with the minimum number of particles required to produce a final state of interest. In these models, all SUSY particles except those directly involved in the particular decay mode studied, are put at a very high scale. In this way, the free parameters of the model can be greatly reduced. As an example, direct squark pair production models normally have two to four sparticle masses and branching ratios as free parameters. One advantage of this approach is that it allow scanning the sparticle mass space without imposing any relations between sparticle masses.

In this section, two simplified models, describing direct and gluino-mediated stop pair production, used in the stop searches presented in this thesis are described. The free parameters in these models are the gluino, stop, neutralino, and chargino masses. The $\tilde{\chi}_1^0$ is considered to be the LSP, and it also stable due to the assumed R-parity conservation. In each model, only one decay mode (except in the case of mixed decay), with 100% branching ratio, is considered.

2.6.1 Direct Stop Pair Production

The searches described in Chapters 9, 10 and 12 all target direct stop pair production. In these models it is assumed that the stop is pair produced in the proton-proton collisions, and that $\tilde{\chi}_1^0$ is the only SUSY particle which is lighter than the stop. If the stop mass is greater than the sum of the t quark and the $\tilde{\chi}_1^0$ masses, the decay $\tilde{t}_1 \rightarrow t\tilde{\chi}_1^0$ is kinematically allowed (Figure 2.2(a)). A stop can undergo a three-body decay (Figure 2.2(b)), $\tilde{t}_1 \rightarrow bW\tilde{\chi}_1^0$, via an off-shell t quark if the mass difference between the \tilde{t}_1 and the $\tilde{\chi}_1^0$ is less then the t quark mass but still above the W boson mass ($m_W \lesssim m_{\tilde{t}_1} - m_{\tilde{\chi}_1^0} \lesssim m_t$). For a stop whose mass is nearly degenerate with the $\tilde{\chi}_1^0$ mass, $m_{\tilde{t}_1} - m_{\tilde{\chi}_1^0} \lesssim m_W$, the decay proceeds via a four-body process (Figure 2.2(c)), $\tilde{t}_1 \rightarrow bff'\tilde{\chi}_1^0$, where f and f' are two different fermions, or via a flavour-changing neutral current (FCNC) processes, such as the loop-suppressed $\tilde{t}_1 \rightarrow c\tilde{\chi}_1^0$ process.

If supersymmetric particles other than the $\tilde{\chi}_1^0$ have masses below that of the stop, then additional decay modes can be allowed. One important scenario is when the $\tilde{\chi}_1^\pm$ is lighter than the stop. Then the stop can decay to a bottom quark and the lightest chargino (Figure 2.2(d)), $\tilde{t}_1 \rightarrow b\tilde{\chi}_1^\pm$, where the $\tilde{\chi}_1^\pm$ further decays into the $\tilde{\chi}_1^0$ by emitting an on- or off-shell W boson ($\tilde{\chi}_1^\pm \rightarrow W^{(*)}\tilde{\chi}_1^0$).

The kinematic properties of this signal model depend on the mass of the $\tilde{\chi}_1^\pm$ relative to the \tilde{t}_1 and $\tilde{\chi}_1^0$ masses. In this thesis the following mass spectra are considered:

- $m_{\tilde{\chi}_1^\pm} = 2 \times m_{\tilde{\chi}_1^0}$: inspired by gauge universality at the Grand Unification scale. In this scenario, the $\tilde{\chi}_1^0$ mass starts at 50 GeV resulting in $\tilde{\chi}_1^\pm$ masses above 100 GeV consistent with the LEP exclusion limits [49–53]. The phenomenology of this

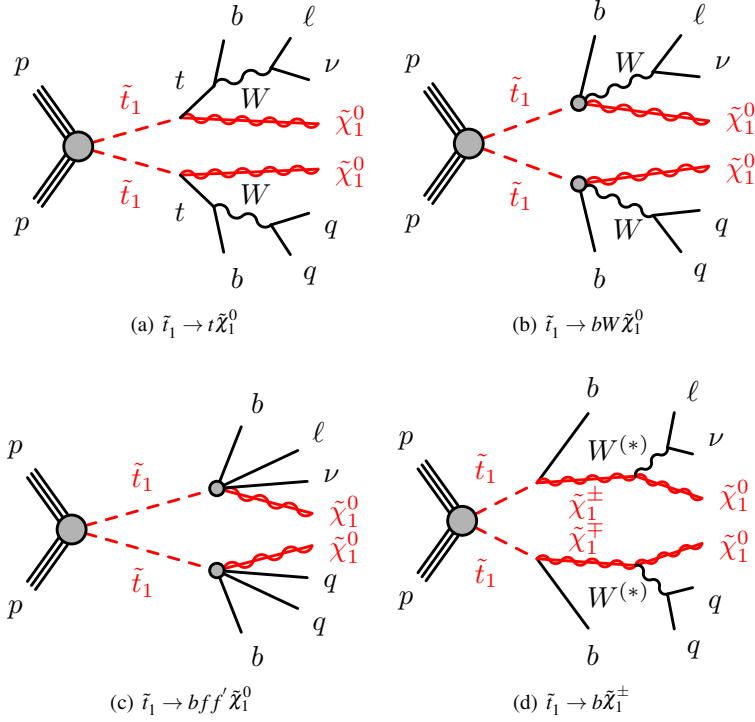


Figure 2.2: Diagrams of stop pair production and its possible decay scenarios. The charge-conjugate symbols are omitted for simplicity. The $W^{(*)}$ indicates the possible with decays with on- or off-shell W boson [1].

signal model depends on the chargino mass. In the regions where the $\tilde{\chi}_1^\pm$ and $\tilde{\chi}_1^0$ have a small mass difference ($m_{\tilde{\chi}_1^\pm} - m_{\tilde{\chi}_1^0} \lesssim m_W$) the $\tilde{\chi}_1^\pm$ decays via an off-shell W boson. If the $\tilde{\chi}_1^\pm$ mass is degenerate with the \tilde{t}_1 mass, $m_{\tilde{t}_1} - m_{\tilde{\chi}_1^\pm} \lesssim m_b$, the b -jet from the stop decay is too soft to be reconstructed in the detector. In the region of intermediate mass difference of the $\tilde{\chi}_1^\pm$ relative to the \tilde{t}_1 and $\tilde{\chi}_1^0$, the W is on-shell and the b -jet from the stop decay is above the reconstruction threshold.

- $m_{\tilde{t}_1} - m_{\tilde{\chi}_1^\pm} = 10$ GeV: The stop and the chargino are nearly mass degenerate resulting in a low-energy b -jet from the stop decay. In this scenario, there is no assumption on the relation between the $\tilde{\chi}_1^\pm$ and $\tilde{\chi}_1^0$ masses.

In addition, a mixed-decay scenario is also considered in the stop search. In this

scenario, both the $\tilde{t}_1 \rightarrow t\tilde{\chi}_1^0$ and the $\tilde{t}_1 \rightarrow b\tilde{\chi}_1^\pm$ decay modes are allowed. One stop is assumed to decay via $\tilde{t}_1 \rightarrow t\tilde{\chi}_1^0$ while the other stop can decay via $\tilde{t}_1 \rightarrow b\tilde{\chi}_1^\pm$. The branching ratio of the $\tilde{t}_1 \rightarrow b\tilde{\chi}_1^\pm$ decay of the second \tilde{t}_1 varies from 0 to 100%. Also here the mass of the $\tilde{\chi}_1^\pm$ is assumed to be $m_{\tilde{\chi}_1^\pm} = 2 \times m_{\tilde{\chi}_1^0}$.

2.6.2 Gluino-Mediated Stop Production

The analysis described in Chapter 11 includes a search for gluino-mediated stop production. In these models, a pair of gluinos are produced. It is assumed that the stop is the only colored SUSY particle which has a mass below the gluino mass. The gluino will therefore decay into a stop and a t quark with 100% branching ratio. The stop further decays into a $\tilde{\chi}_1^0$ and SM particles. The decays mainly depend on the mass splitting between the stop and the $\tilde{\chi}_1^0$. In the gluino-mediated stop scenario considered in this thesis, the mass splitting between the \tilde{t}_1 and $\tilde{\chi}_1^0$ is less than 5 GeV. Considering such a small mass splitting, the most dominant stop decay channel is $\tilde{t} \rightarrow c + \tilde{\chi}_1^0$. However, due to the small mass splitting between the \tilde{t}_1 and $\tilde{\chi}_1^0$, the visible particles (e.g. the c quarks) from the stop decays generally below the reconstruction threshold and cannot be detected. Consequently, the entire energy carried by the stop is lost in the detector and thus becomes missing energy. From the experimental point of view, the decay products of the gluino pair are $t\bar{t} + E_T^{\text{miss}}$ as shown in Figure 2.3 (left). It is effectively the same final state as in the direct stop pair production scenario shown in Figure 2.3 (right). However, the gluino-mediated stop scenario has larger production cross-section at the LHC.

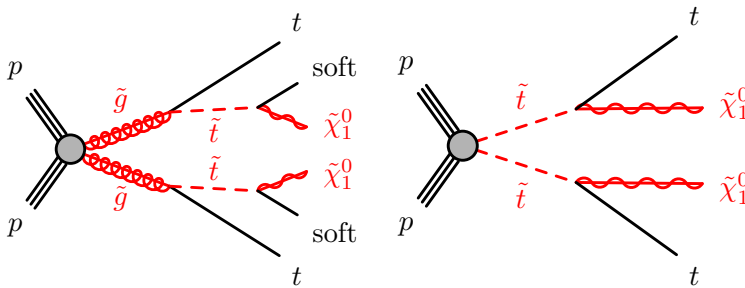


Figure 2.3: Gluino-mediated stop pair production (left) and direct stop pair production (right). The \tilde{t}_1 and $\tilde{\chi}_1^0$ in the left diagram have degenerate masses, therefore all the decay products of the \tilde{t}_1 are invisible to the detector. The charge-conjugate symbols are omitted [5].

2.7 Phenomenological MSSM Models

The phenomenological MSSM (pMSSM) [54] is a variant of the MSSM which is subject to a minimal set of phenomenological assumptions: (i) CP-conservation, (ii) minimal flavor violation at the electroweak scale, (iii) first and second generation sfermion mass universality, (iv) negligible Yukawa-couplings and A-terms (trilinear couplings) for the first two generations. Compared to the mSUGRA model, the pMSSM is less theoretically constrained. In particular, no assumptions about physics at the GUT scale are made in the pMSSM. Imposing the phenomenological assumptions, there are 19 (20) free parameters left in the neutralino LSP (gravitino LSP) pMSSM models. The 19 free parameters [55] are the gaugino masses M_1 , M_2 , M_3 , the Higgsino mixing parameter μ , the ratio of the two Higgs vacuum expectation values $\tan\beta$, the mass of the pseudoscalar Higgs boson M_A , the ten squared masses of the sfermions (five for the assumed degenerate first two generations and five for the third generation) and the A-terms for the b , t and τ sectors. In the extended models which include the gravitino as the LSP, the gravitino mass is added as an additional parameter.

In this thesis, three sets of pMSSM models, pMSSM models with fixed stop and LSP masses, 3rd generation squark enriched pMSSM models and general pMSSM models, are used. The analyses using these models are described in Chapter 10. The details of the various pMSSM models are given below.

2.7.1 pMSSM Models with Fixed Stop and LSP Masses

The sensitivity of the stop search depends strongly on the stop and LSP masses. A total of 27 models out of 10,200 described in [56] are therefore selected in three small mass window in the stop and LSP mass plane to study the dependence of the sensitivity on other parameters. The 14 models in mass window 1 have stop masses between 400 and 420 GeV and χ_1^0 masses between 38 and 50 GeV. The ten models in mass window 2 have stop masses between 545 and 555 GeV and χ_1^0 masses between 40 and 50 GeV. The three models in mass window 3 have stop masses between 545 and 555 GeV and χ_1^0 masses between 145 and 155 GeV. Only models with more than one stop decay mode are selected in order to complement the already simulated simplified models. In the event simulation, only the direct stop pair production events are considered, even though the signal regions studied have some sensitivity also to e.g. sbottom production. The available decay channels are shown in Figure 2.4.

Table 2.2 shows some relevant parameters of the 27 selected models. In most of the models, the stop is primarily the partner of the left-handed top quark, the lightest neutralino is the LSP and is mainly bino-like. Even though the LSP is much lighter than the other SUSY particles in these models the \tilde{t}_1 prefers to decay into the more Higgsino- or wino-like heavier neutralinos or charginos except in the models where the stop is mainly the partner of the right-handed top quark. The models have almost degenerate masses for the $\tilde{\chi}_1^\pm$, $\tilde{\chi}_2^0$ and $\tilde{\chi}_3^0$, and have higher masses for $\tilde{\chi}_2^\pm$. Therefore,

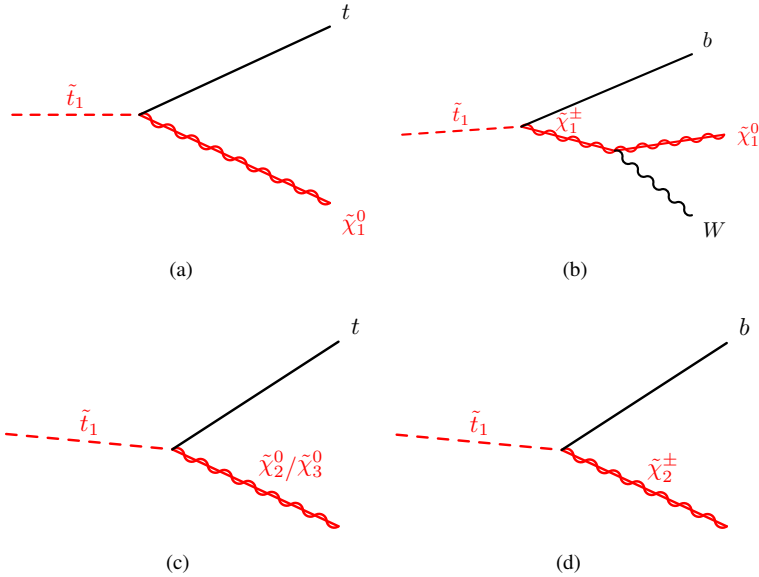


Figure 2.4: Stop decay diagrams illustrating the possible decay scenarios in the pMSSM. All diagrams begin with a squark, and the charge-conjugate symbols are omitted for simplicity.

the $\tilde{\chi}_{2,3}^0$ will almost exclusively decay into a $\tilde{\chi}_1^0$ by emitting an on-shell or off-shell h or Z boson and the $\tilde{\chi}_1^\pm$ will decay into a $\tilde{\chi}_1^0$ by emitting an on-shell or off-shell W boson. The decay of the $\tilde{\chi}_2^\pm$ is more complicated than the others. It can either directly decay into a $\tilde{\chi}_1^0$ by emitting a W boson or can go via a $\tilde{\chi}_{2,3}^0$ or a $\tilde{\chi}_1^\pm$.

2.7.2 3rd Generation-Enriched pMSSM Models

The pMSSM with the $\tilde{\chi}_1^0$ as the LSP has 19 parameters in addition to the SM parameters, making it cover a wide range of phenomena. However, not all of the 19 parameters have an impact on the processes involving third generation squarks. With some additional assumptions, the number of parameters can be reduced to a small set that has a substantial impact on the production and decay of third generation squarks [3]:

- First and second generation squarks are irrelevant to the 3rd generation squark phenomenology; they are suppressed in the production by setting their masses to multiple TeV. This setup is also compatible with the results from the first and second generation squarks searches which have excluded these particles up to

\tilde{t}_1	Mass [GeV]					Branching ratio $\tilde{t}_1 \rightarrow$					$[\Re_{11}]^2$	$[N_{11}]^2$
	$\tilde{\chi}_1^0$	$\tilde{\chi}_2^0$	$\tilde{\chi}_3^0$	$\tilde{\chi}_1^\pm$	$\tilde{\chi}_2^\pm$	$t\tilde{\chi}_1^0$	$t\tilde{\chi}_2^0$	$t\tilde{\chi}_3^0$	$b\tilde{\chi}_1^\pm$	$b\tilde{\chi}_2^\pm$		
404	40	221	230	220	1073	0.09	0.01	0.09	0.81	0.00	0.53	0.96
404	44	324	345	425	471	0.16	0.00	0.00	0.84	0.00	0.98	0.99
407	46	368	372	367	1515	0.74	0.00	0.00	0.26	0.00	0.02	0.98
408	49	187	207	188	376	0.02	0.31	0.23	0.41	0.04	0.97	0.95
409	39	211	212	206	1768	0.05	0.24	0.03	0.68	0.00	0.56	0.95
409	49	180	190	179	796	0.02	0.22	0.17	0.59	0.00	0.99	0.94
410	40	232	253	234	427	0.11	0.25	0.00	0.64	0.00	0.96	0.97
410	43	387	396	386	889	0.88	0.00	0.00	0.12	0.00	0.01	0.99
413	42	197	367	197	385	0.03	0.10	0.00	0.85	0.02	0.95	0.98
413	45	373	406	374	508	0.32	0.00	0.00	0.68	0.00	0.99	0.99
414	45	194	440	195	453	0.03	0.14	0.00	0.83	0.00	0.96	0.99
416	45	394	397	393	1975	0.90	0.00	0.00	0.10	0.00	0.99	0.99
417	46	333	350	335	573	0.65	0.00	0.00	0.35	0.00	0.96	0.98
418	39	206	209	202	1779	0.08	0.05	0.28	0.59	0.00	0.47	0.95
546	46	292	310	292	520	0.02	0.28	0.24	0.44	0.01	0.98	0.98
547	46	346	374	346	500	0.12	0.49	0.00	0.22	0.16	0.93	0.98
550	40	225	235	225	760	0.02	0.28	0.24	0.46	0.00	0.98	0.96
551	43	351	366	351	621	0.07	0.38	0.21	0.35	0.00	0.98	0.99
552	41	249	275	252	420	0.02	0.20	0.21	0.44	0.13	0.98	0.97
552	42	332	337	331	1496	0.05	0.47	0.35	0.13	0.00	0.99	0.98
552	43	346	350	344	1501	0.08	0.27	0.52	0.13	0.00	0.97	0.98
552	43	385	397	385	731	0.36	0.00	0.00	0.64	0.00	0.97	0.99
554	44	439	445	439	1007	0.21	0.00	0.00	0.79	0.00	0.99	0.99
555	47	279	287	280	933	0.04	0.54	0.38	0.04	0.00	0.97	0.97
553	147	169	444	168	455	0.31	0.12	0.00	0.27	0.30	0.07	0.94
554	151	195	207	191	1969	0.09	0.35	0.43	0.12	0.00	0.88	0.68
546	154	210	213	200	434	0.07	0.40	0.34	0.05	0.14	0.86	0.70

Table 2.2: The masses of the stop, neutralinos and charginos in the 27 selected pMSSM models. The branching ratios of the possible stop decays, the left-handed stop content of the \tilde{t}_1 ($[\Re_{11}]^2$ with \Re being the stop mixing matrix), and the bino content of the χ_1^0 ($[N_{11}]^2$ with N being the neutralino mixing matrix).

massed well above 1 TeV. The slepton masses are also set to high values (same as the first and second generation squarks) to decouple them from the third generation phenomena.

- The trilinear coupling A_τ is set to $A_\tau = 0$ to decouple the stau.
- The trilinear coupling A_b is set to $A_b = 0$ since the sbottom sector has a small impact on the relevant phenomena.

- The decoupling limit $M_A = 3$ TeV and $\tan\beta > 15$ are chosen to impose the results of heavy Higgs searches at the LHC.
- The full parameter space is required to satisfy the Higgs mass constraint of 125 GeV which strongly depends on the stop mass parameter $M_s = \sqrt{m_{\tilde{t}_1} m_{\tilde{t}_2}}$ and the mixing parameter $X_t = A_t - \mu/\tan\beta$.
- Gluino masses are set to $M_3 = 1.7$ TeV which is above the gluino exclusion limits from the ATLAS Run 1 result.

The remaining free parameters are μ , M_1 , M_2 and the stop/sbottom masses $m_{\tilde{q}L3}$, $m_{\tilde{t}R}$ and $m_{\tilde{b}R}$. By setting these parameters, three types of pMSSM models dominated by 3rd generation squark production are constructed. These are used in the interpretation of all 3rd generation squark searches with ATLAS Run 1 data.

Naturalness-inspired pMSSM Models

These models are required to satisfy naturalness criteria which constrain the μ parameter to be small, about a few hundred GeV. The μ and left-handed squark mass parameter $m_{\tilde{q}L3}$ are chosen as the free parameters while the other parameters are either fixed or determined from the values of μ and $m_{\tilde{q}L3}$. The parameter μ is scanned in the range of $100 \text{ GeV} < \mu < m_{\tilde{q}L3} - 150 \text{ GeV}$ with a 50 GeV step size. The lower bound of 100 GeV, is determined from LEP exclusion limits [49–53]. The upper bound is chosen to avoid having too small mass gaps between the stop/sbottom and the lightest neutralino. The parameter $m_{\tilde{q}L3}$ is scanned in the range of $350 \text{ GeV} < m_{\tilde{q}L3} < 900 \text{ GeV}$ with a 50 GeV step size. The lower bound of 350 GeV is chosen such that the stop and sbottom both also decay via charginos and heavier neutralinos. The upper bound is set to be above the stop mass limit from simplified models.

The right-handed stop mass $m_{\tilde{t}R}$ and X_t are determined by the maximal mixing scenario, $X_t/M_s = \sqrt{6}$. The value of $X_t/M_s = \sqrt{6}$ is required such that the Higgs boson has a mass around 125 GeV throughout the entire parameter space. The wino mass parameter M_2 is set to $M_2 = 3\mu$; this setting allows a $\tilde{\chi}_2^\pm$ with a higher mass. The gluino mass parameter is fixed at $M_3 = 1.7$ GeV, while the bino mass parameter, M_1 , and other SUSY mass parameters are set to 3 TeV which decouple them from the phenomena probed with these models.

Well-tempered Neutralino pMSSM Models

These models are motivated by the measured thermal-relic density. The desired parameter space of these models loosely satisfies the thermal-relic density between 0.9 and 0.15. Furthermore, it requires a fine-tuning of less than 1% which is measured using the Ellis-Barbieri-Giudice measure [45, 57]. The parameter space, spanned by M_1 and $m_{\tilde{q}L3}$ or $m_{\tilde{t}R}$ is scanned with a 50 GeV step size. The wino mass parameter M_2 is set to

$M_2 = 2$ TeV in order to have a $\tilde{\chi}_2^\pm$ with a mass much greater than the stop or sbottom masses. Other irrelevant SUSY mass parameters are set to 3 TeV. The $\tan\beta$ parameter is set to 20 for both scenarios. The Higgsino mass μ is set to around the bino mass, $\mu \approx -M_1$, to ensure that the lightest neutralino is a mixture of bino and Higgsino. Finally, to impose the Higgs mass constraint, the Higgs mass is required to be in the range 123 GeV - 129 GeV for the entire desired parameter space. These settings lead us to consider two types of scenarios regarding the handedness of the stop, the left-handed and the right-handed stop scenarios:

- **Left-handed stop:** The parameter space is scanned in M_1 in the range $110 \text{ GeV} \leq M_1 \leq 410 \text{ GeV}$ and in $m_{\tilde{q}L3}$ in the range $310 \text{ GeV} \leq m_{\tilde{q}L3} \leq 850 \text{ GeV}$. $m_{\tilde{q}L3} = \mu + 10 \text{ GeV}$ is used to constrain the $\tilde{\chi}_1^\pm$ and $\tilde{\chi}_{2,3}^0$ masses to be below the desired left-handed stop masses. The stop mixing parameters are set to $X_t/M_S = \sqrt{7}$ with M_S in the range $850 \text{ GeV} < M_S < 950 \text{ GeV}$ in order to get the Higgs mass right.
- **Right-handed stop:** The parameter space is scanned in M_1 in the range $110 \text{ GeV} \leq M_1 \leq 410 \text{ GeV}$ and in $m_{\tilde{t}R}$ in the range $260 \text{ GeV} \leq m_{\tilde{t}R} \leq 760 \text{ GeV}$. $m_{\tilde{t}R} = \mu + 10 \text{ GeV}$ is used to constrain the $\tilde{\chi}_1^\pm$ and $\tilde{\chi}_{2,3}^0$ masses to be below the desired right-handed stop masses. The stop mixing parameters are set to $X_t/M_S = \sqrt{6}$ and M_S to around 1 TeV to get the right Higgs mass.

h/Z -enriched pMSSM Models

These models aim at having the Higgs boson or the Z boson in the decay chain of the stop or sbottom. This kind of decay requires the $\tilde{\chi}_{2,3}^0$ to be lighter than the stop and sbottom, and the $\tilde{\chi}_{2,3}^0$ and $\tilde{\chi}_1^0$ to have enough mass splitting for the decay chain to involve Higgs and Z bosons. The parameter space is scanned in μ and $m_{\tilde{b}R}$ or $m_{\tilde{q}L3}$. The bino mass parameter M_1 is set to $M_1 = 100 \text{ GeV}$, which makes the LSP mostly bino-like. The gluino mass parameter M_3 is set to $M_3 = 2.5 \text{ TeV}$, which suppresses the direct gluino production. The stop mixing parameters are chosen with maximal mixing which satisfies the constraint on the Higgs mass being around 125 GeV over the desired parameter space. There are two possible production mechanisms:

- **Sbottom production dominated scenario:** The parameter space is scanned in μ in the range of $100 \text{ GeV} < \mu < m_{\tilde{b}R}$, and in $m_{\tilde{b}R}$ in the range of $250 \text{ GeV} < m_{\tilde{b}R} < 750 \text{ GeV}$. The wino mass parameter M_2 is set to μ . The third generation squark mass parameter $m_{\tilde{q}L3}$ is set to 1.2 TeV, and the right-handed stop mass parameter $m_{\tilde{t}R}$ is set to 1.6 TeV. This setting puts the stop mass well above the TeV scale so that the sbottom is dominantly produced.
- **Stop and sbottom production dominated scenario:** The parameter space is scanned in the range of $100 \text{ GeV} < \mu < m_{\tilde{q}L3}$, and in $m_{\tilde{q}L3}$ in the range of 500 GeV

$< m_{\tilde{q}L3} < 800$ GeV. The wino mass parameter M_2 is set to 1 TeV. The right-handed sbottom mass parameter $m_{\tilde{b}R}$ is set to 3 TeV and the right-handed stop mass parameter $m_{\tilde{t}R}$ is set to 2 TeV. These settings make the left-handed stop and sbottom lighter and with almost degenerate masses so that they both are dominantly produced in the pp collision.

2.7.3 General pMSSM Models

A total of 500 million models are produced by sampling the 19-dimensional parameter space within the ranges shown in Table 2.3. The models are further required to pass the constraints from precision electroweak and flavor measurements, the constraints from the dark matter searches and various collider constraints, leaving a total of 310,327 models [4]. These are used to determine the impact of the entire ATLAS SUSY search program on the allowed pMDDM parameter space.

90 GeV	$<$	$m_{\tilde{L}(e)1,2,3}$	$<$	4 TeV
200 GeV	$<$	$m_{\tilde{Q}(q)1,2}$	$<$	4 TeV
100 GeV	$<$	$m_{\tilde{Q}(q)3}$	$<$	4 TeV
0 GeV	$<$	$ M_1 $	$<$	4 TeV
70 GeV	$<$	$ M_2 $	$<$	4 TeV
80 GeV	$<$	$ \mu $	$<$	4 TeV
200 GeV	$<$	M_3	$<$	4 TeV
0 GeV	$<$	$ A_{t,b,\tau} $	$<$	4 TeV
0 GeV	$<$	$ A_t $	$<$	8 TeV
100 GeV	$<$	M_A	$<$	4 TeV
1	$<$	$\tan\beta$	$<$	60

Table 2.3: The ranges of parameters scanned when generating the general ATLAS pMSSM models.

- Constraints from precision electroweak and flavor measurements: Each model must have the electroweak parameter in the range $-0.0005 < \Delta\rho < 0.0017$ [58]. This parameter describes the radiative corrections to the Z boson coupling strength, the effective weak mixing angle, and the W boson mass. Each model satisfies the branching ratio of $b \rightarrow s\gamma$ within a 2σ interval around the experimental measurement [59]. The branching ratio of $B_s \rightarrow \mu^+\mu^-$ is also required to be within a 2σ interval around the value measured by the LHCb and CMS collaborations [60, 61]. Each model is required to have the branching ratio, $B^+ \rightarrow \tau^+\nu_\tau$, within a 2σ interval around the measured value [62–65]. The last constraint is from the anomalous magnetic moment of the muon, $\Delta(g-2)_\mu$. The selected models must

have $\Delta(g-2)_\mu$ within a 3σ interval around the SM value [66–69] and the measured value [70, 71] which is corrected using an updated value of the magnetic moment ratio of the muon and the proton [72, 73].

- Dark matter constraints: Since the LSP is assumed to be stable, it contributes to the cosmological abundance. There is no assumption that the LSP is the only candidate for dark matter. Therefore, the LSP abundance is constrained to have a smaller thermal relic density than the latest measurement from the Planck collaboration, 0.1188 ± 0.0010 [74]. In addition, the constraints from the spin-independent and the spin-dependent cross section limits for a neutralino interacting with a nucleus are also applied. The upper bounds on the cross sections are set to four times the limits from [75–77] to take into account the nucleon form-factor uncertainties described in [78].
- Collider constraints: The constraints from LEP measurements [79, 80], and the Higgs mass measurement at the LHC are imposed. The predicted masses of the charged sparticles should be heavier than 100 GeV, which is consistent with the LEP limit. The predicted SM-like Higgs boson mass is required to be within the range of 124 GeV - 128 GeV, corresponding to a 2 GeV window around the LHC measurement of the Higgs boson mass [15, 16].

2.8 Sparticle Pair Production Cross Sections in pp Collisions

The cross section for sparticle production at LHC depends on the center of mass energy of the LHC and the mass of the sparticle. Figure 2.5 shows the sparticle production cross sections in pp collisions at center-of-mass energies of $\sqrt{s} = 8$ TeV [81] and $\sqrt{s} = 13$ TeV [82], as a function of average masses of the sparticles. The cross sections are calculated at next-to-leading order with resummation of soft gluon emission to next-to-leading-log order accuracy (NLO+NLL). The cross section for the direct \tilde{g} pair production is about 50 times higher than the direct \tilde{t}_1 pair production at the same sparticle mass, due to the additional spin and color states. Table 2.4 shows the comparison of the cross sections of $\tilde{g}-\tilde{g}$ and $\tilde{t}_1-\tilde{t}_1$ production at the sparticle masses 700 GeV, 1000 GeV and 1200 GeV. The higher production cross section for direct gluino pair production is the main motivation for the analysis described in Chapter 11.

2.9 Search for Supersymmetry at ATLAS

As the masses of the superpartners in the MSSM are predicted to be in the order of the electroweak scale, it is one of the best motivated frameworks to search for at the LHC. To date, no excess over the expected background from SM processes has been observed by the ATLAS experiment. Therefore, the data are used to set limits on various SUSY parameters such as the masses of the superpartners.

Mass	$\sigma_{\tilde{t}_1-\tilde{t}_1}$ [pb]	$\sigma_{\tilde{g}-\tilde{g}}$ [pb]
700 GeV	0.06705	3.52510
1000 GeV	0.00615	0.32539
1200 GeV	0.00160	0.08564

Table 2.4: Cross sections for $\tilde{t}_1-\tilde{t}_1$ and $\tilde{g}-\tilde{g}$ production in pp collisions at $\sqrt{s} = 13$ TeV, for particle masses of 700 GeV, 1000 GeV and 1200 GeV.

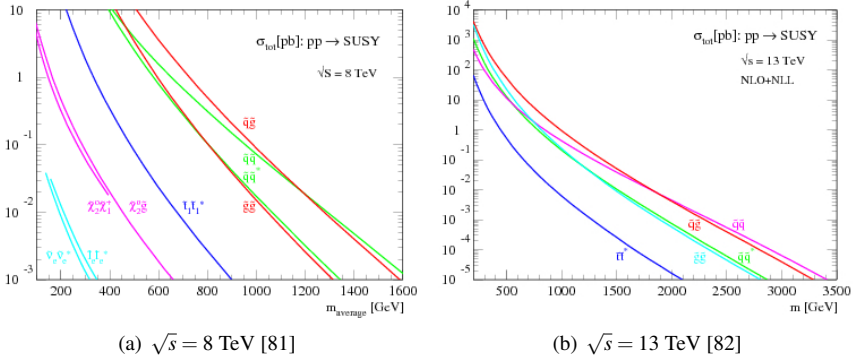


Figure 2.5: Sparticle production cross sections as a function of the average sparticle mass in pp collisions at $\sqrt{s} = 8$ TeV (a) and $\sqrt{s} = 13$ TeV (b). The cross sections are calculated at NLO+NLL.

Figures 2.6 and 2.8 show the excluded parameter space of the gluino (\tilde{g}), the lightest stop (\tilde{t}_1) and the LSP ($\tilde{\chi}_1^0$). For neutralino masses below 700 GeV, the gluino masses about 1.78 GeV and 1.76 GeV are excluded at 95% CL. The excluded masses for the lightest stop from searches for direct stop pair production are still below the TeV mass scale. For small $\tilde{\chi}_1^0$ masses, stop masses up to around 850 GeV are excluded for the $\tilde{t}_1 \rightarrow t\tilde{\chi}_1^0$. For the $\tilde{t}_1 \rightarrow b\tilde{\chi}_1^\pm$ scenario with $m_{\tilde{\chi}_1^\pm} = 2 \times m_{\tilde{\chi}_1^0}$, the stop masses up to about 750 GeV are excluded for the neutralino masses about 150 GeV.

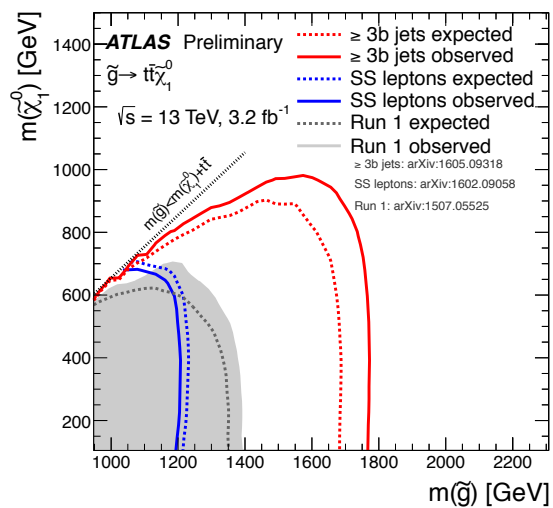


Figure 2.6: Exclusion limits at 95% CL in the $(m(\tilde{g}), m(\tilde{\chi}_1^0))$ plane for the $\tilde{g} \rightarrow tt$ model. The two gluinos decay via off-shell stop and produce four top quarks and two $\tilde{\chi}_1^0$. Uncertainties from signal model cross sections are not included in the limits [83].

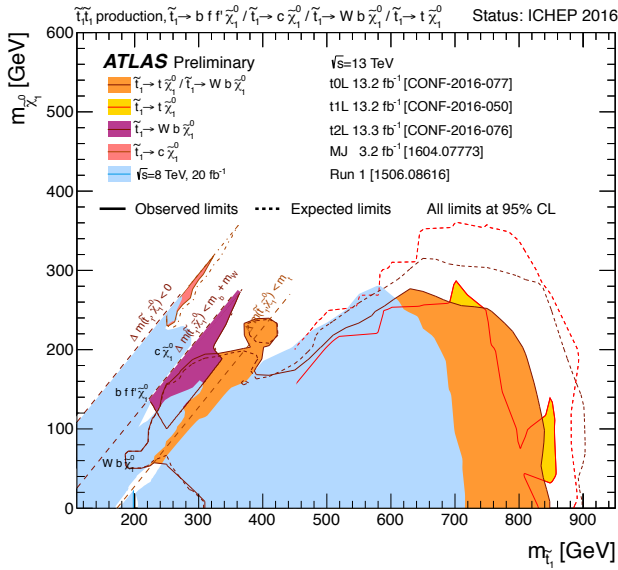


Figure 2.7: Summary of the exclusion limits at 95% CL for the searches for direct stop pair production at $\sqrt{s} = 8$ TeV and $\sqrt{s} = 13$ TeV. The limits are shown for the $\tilde{t}_1 \rightarrow t \tilde{\chi}_1^0$, $\tilde{t}_1 \rightarrow b W \tilde{\chi}_1^0$ and $\tilde{t}_1 \rightarrow b f f' \tilde{\chi}_1^0$ decay scenarios. Uncertainties from signal model cross sections are not included in the limits [83].

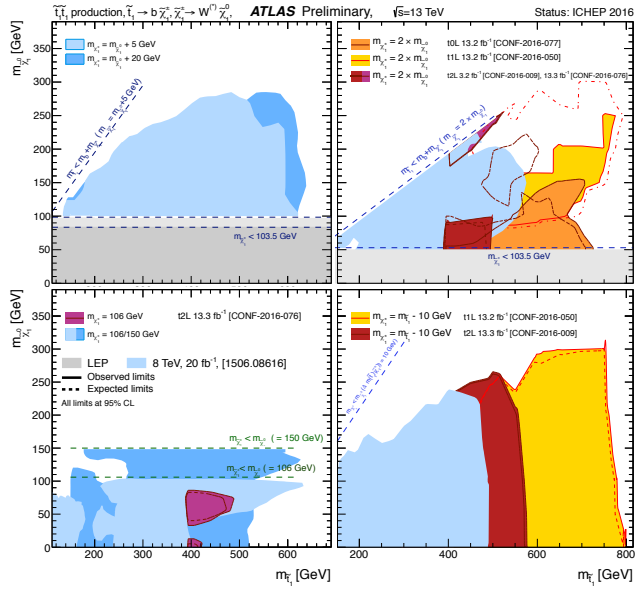


Figure 2.8: Summary of the exclusion limits at 95% CL for the searches for direct stop pair production at $\sqrt{s} = 8$ TeV and $\sqrt{s} = 13$ TeV. The limits are shown for $\tilde{t}_1 \rightarrow b\tilde{\chi}_1^\pm$ decay scenarios with various $\tilde{\chi}_1^\pm$ mass hierarchy. Uncertainties from signal model cross sections are not included in the limits [83].

Part II

Experimental Overview

3 The Large Hadron Collider

The world's largest particle accelerator is the Large Hadron Collider (LHC) [84]. It is a synchrotron accelerator in which the electric and magnetic fields are synchronized with the accelerating particle beams. The LHC was built to accelerate protons up to a center-of-mass energy of $\sqrt{s} = 14$ TeV, and therefore provides a possibility to study the electroweak symmetry breaking and to search for new physics at the TeV scale; searches for the Higgs boson and BSM physics were the main objectives of this machine.

This chapter is organized as follows. The LHC machine and its accelerator chain are described in Section 3.1. The LHC luminosity and its pileup conditions are described in Section 3.2.

3.1 LHC and the Accelerator Chain

The LHC is the world's most complex particle accelerator. It is located at CERN, the European Organization for Nuclear Research, near Geneva. Its storage ring is 27 km in circumference and installed about 100 m underground, in the old Large Electron Positron Collider (LEP) tunnel.

However, the LHC storage ring cannot accelerate particles from rest. Instead, it relies on a chain of pre-accelerators that raise the kinetic energy of the particle beams before they are injected into the LHC. As shown in Figure 3.1, several synchrotron and linear accelerators are supplying the LHC ring. The simplified LHC accelerator chain is shown in Figure 3.2. The chain starts with a linear accelerator (LINAC 2) which is about 30 meters long; there, hydrogen atoms which have their electrons stripped away form the proton beams. The proton beams are accelerated to reach 50 MeV kinetic energy at the end of LINAC 2. The next step in the chain is the Proton Synchrotron Booster (PSB) which is composed of four superimposed synchrotron rings; each of them is about 150 meters long. The PSB accelerates and squeezes the protons into a high-intensity proton beam which has a 1.4 GeV beam energy when it exits the PSB. This beam is passed on to the next accelerator in the chain, the Proton Synchrotron (PS). The PS has a circumference of 628 meters, and it provides 25 GeV proton beams to the

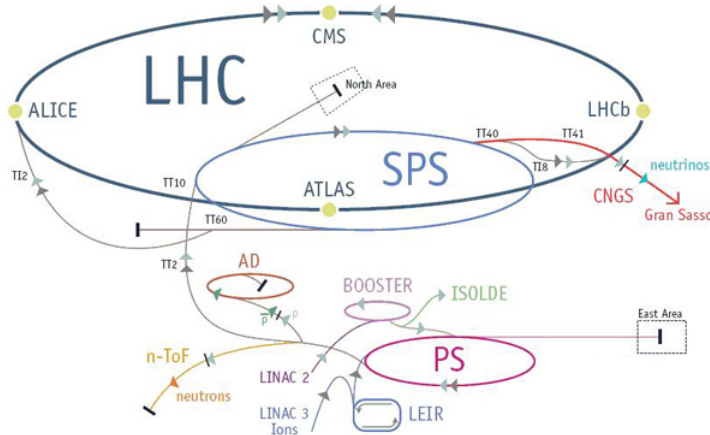


Figure 3.1: CERN's accelerator complex with the LHC and its pre-accelerators [85].

next accelerator, the Super Proton Synchrotron (SPS). The SPS is the second largest accelerator at CERN; it is nearly 7 kilometers in circumference. Finally, the SPS injects 450 GeV proton beams into the LHC ring, the final synchrotron accelerator in the chain.

The LHC ring has two separate vacuum beam pipes, and the proton beams from the SPS are split into two sets that are injected in the two pipes. One proton beam circulates clockwise while the other one circulates anti-clockwise around the ring. The two beam pipes are surrounded by more than 7000 superconducting coils which provide a magnetic field up to 8.3 T in order to trap the beams inside the storage ring. Figure 3.3 shows the cross-section of an LHC dipole magnet; it generates two magnetic fields with opposite directions that are perpendicular to the beam pipes. The two beam pipes cross each other at four colliding points where the proton bunches are brought to collide up to every 25 ns. At these points, the four complex particle detectors, ATLAS, CMS, ALICE, and LHCb are installed. The ATLAS and CMS experiments are general-purpose detectors which are independently designed to investigate a broad range of physics phenomena. The ALICE experiment is designed to study heavy-ion collisions and the LHCb experiment is designed to study the decays of hadrons containing bottom quarks.

3.2 LHC Parameters

3.2.1 Center of Mass Energy and Luminosity

The center of mass energy of the LHC is a critical parameter in new physics searches. The maximum center of mass energy of the LHC is 14 TeV which allows for investi-

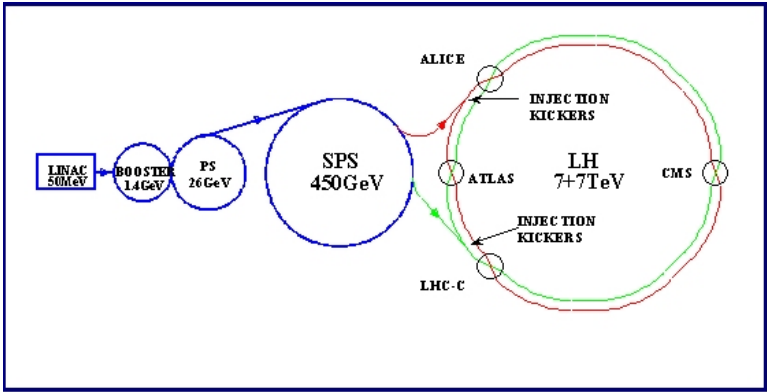


Figure 3.2: The acceleration steps of an LHC and its pre-accelerators.

LHC DIPOLE : STANDARD CROSS-SECTION

CERN AC/CD/MTM - HE107 - 30.04.1999

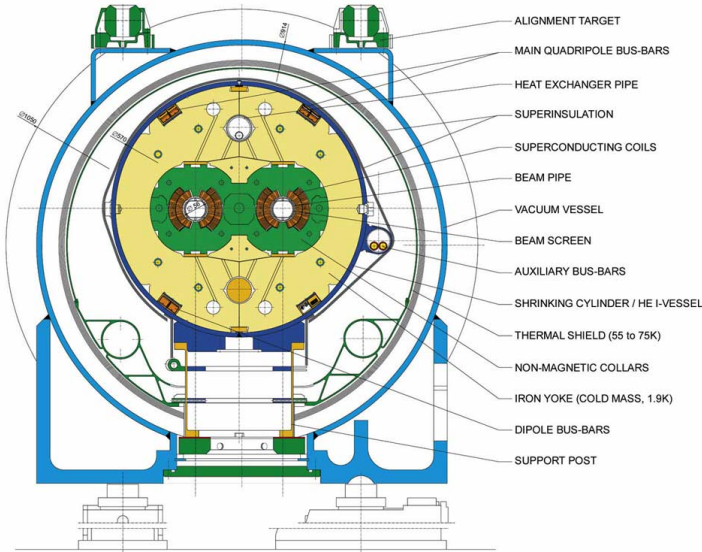


Figure 3.3: Cross-section of the LHC dipole magnet [84].

gation of a vast range of BSM physics scenarios. With such a high collision energy, massive particles at the TeV scale can be created, if they exist at that energy scale. The LHC also accelerates heavy ions up to 1150 TeV (2.76 TeV per nucleon pair) for heavy ion collisions.

Another key parameter is the luminosity of the LHC. The higher the luminosity, the larger the accumulated data set, and a large amount of data is essential to perform high precision measurements and study rare physics processes.

The instantaneous luminosity, \mathcal{L} , is a measure of the number of collisions that can be produced per cm^2 and second. The design value of \mathcal{L} for proton-proton collisions in the LHC is $10^{34} \text{ cm}^{-2}\text{s}^{-1}$, corresponding to the peak luminosity that the LHC can reach when filled with proton bunches. The instantaneous luminosity decreases with the run time; after a certain amount of time the circulating beams will be dumped and the LHC ring will be injected with new proton bunches. The instantaneous luminosity is related to the number of particles in each bunch and is defined as:

$$\mathcal{L} = \frac{N_b^2 n f_r \gamma}{4\pi \epsilon_n \beta^*} \quad (3.1)$$

where N_b is the number of particles in each bunch, n is number of bunches in the LHC ring, f_r is the cycling frequency of the bunches, γ is the relativistic factor, ϵ_n is the normalized transverse emittance and β^* is the β function at the interaction point [84].

The integrated luminosity, $L_{\text{int}} = \int \mathcal{L} dt$, is the integral of the instantaneous luminosity over a certain amount of time; in the LHC this generally corresponds to entire run periods, for example one or two years of data taking. Correspondingly, the total number of produced events N from a physics process with a production cross section σ is related to the integrated luminosity, which is

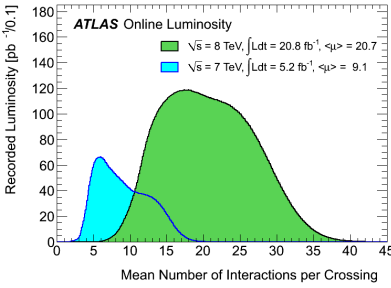
$$N = L_{\text{int}} \times \sigma. \quad (3.2)$$

The unit of the integrated luminosity is normally inverse barn (b^{-1}), where $1 \text{ b} = 10^{-24} \text{ cm}^2$ and cross sections are analogously given in units of barn (b).

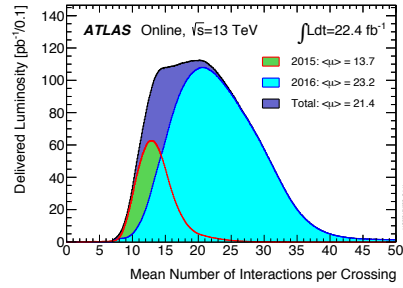
In September 2008, beam was successfully circulated in the LHC ring for the first time. In March 2010 the first proton-proton collisions with a beam energy of 3.5 TeV (7 TeV center of mass energy) took place. In 2011, the center of mass energy was raised to 8 TeV (4 TeV per beam). These data are referred as the Run 1 data. In 2013, the Run 1 data taking was terminated and the LHC entered a shutdown scheduled to last until 2015. The main purpose of the shutdown was to upgrade the machine to allow for proton-proton collisions at 13 and 14 TeV. After two years of work on upgrading, in May 2015, the Run 2 data taking started at a collision energy of 13 TeV.

3.2.2 Pileup Conditions

In each collision, more than one proton-proton interaction takes place. One of them is selected as a primary interaction (see section 6.2) and the others are regarded as pileup interactions. Increasing the number of protons in each bunch increases the instantaneous luminosity, but it also increases the number of pileup interactions in each collision. The high pileup conditions degrade the reconstruction and identification capability of the detector, e.g. the tracking and vertexing performance; consequently, it also affects the flavor tagging of reconstructed jets (see chapter 6 for a description of the object reconstruction). Figure 3.4 shows the measured mean number of interactions per bunch crossing. The 8 TeV data have an average of 20 interactions per bunch crossing while the 7 TeV and 13 TeV data have an average of 9 and 13-23 interactions per bunch crossing respectively.



(a) The 2011 and 2012 data [86]



(b) The 2015 and 2016 data [87]

Figure 3.4: Luminosity-weighted distributions of the mean number of interactions per bunch crossing.

4 The ATLAS Detector

The ATLAS detector is a complex particle detector which helps to understand the micro world of elementary particles. Over the past few years, the ATLAS detector has collected a huge amount of data for the various physics programs carried out in the ATLAS experiment. This chapter describes the ATLAS detector and its sub-detectors. In section 4.1 an overview of the full ATLAS detector is given. The ATLAS coordinate system and its geometrical parameters are described in section 4.2. The various ATLAS sub-detectors are described in sections 4.3-4.5. To reduce the recorded data size, trigger selections and event filters are applied. The trigger and data acquisition systems are described in section 4.6.

4.1 Detector Overview

ATLAS [88] is a general-purpose detector, designed with a forward-backward symmetric cylindrical geometry covering nearly 4π in solid angle. ATLAS is a huge detector; it is 44 meters long and 25 meters high. The overall weight is about 7000 tons. The ATLAS experiment covers broad SM and BSM physics programs, and the collaboration includes over 175 institutes from 38 countries with more than 3000 physicists.

As shown in Figure 4.1, ATLAS is composed of several sub-detector systems which aim at measuring tracks, momenta and energies of particles that interact with the detector material. Figure 4.2 illustrates the purpose of each sub-detector. The inner detector (ID) is designed to measure the trajectories of electrically charged particles. It is composed of several layers. Each layer of the ID measures the positions of particles when they pass through it. Then full trajectories are extracted by fitting track hypotheses to all hits in the ID. The ID also measures the momenta of the charged particles. It is surrounded by a superconducting solenoid magnet which provides a 2 T magnetic field, and the trajectories of moving charged particles are bent by the magnetic field. The bent trajectory provides momentum information of the particles. Outside the ID, electromagnetic calorimeters and hadronic calorimeters are installed. Electrons and photons are captured by the electromagnetic calorimeter, which is installed in front of the hadronic calorimeter. Hadrons instead pass through the electromagnetic calorimeter and are captured by the hadronic calorimeter. A stopped particle loses its energy inside the

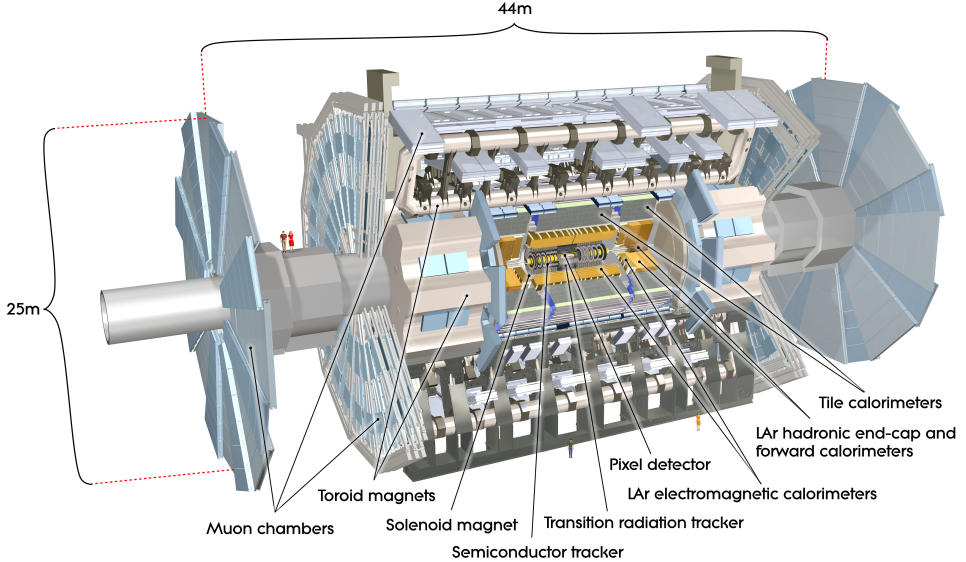


Figure 4.1: Cut-away view of the ATLAS detector and its sub-detectors [89].

calorimeter where the deposited energy is transformed into a measurable signal. The measured signal is proportional to the energy of the particle. Muons escape from the calorimeters since they interact very little with the detector material. The momentum of a muon is measured in a dedicated sub-detector, the muon spectrometer (MS), which surrounds the calorimeter. The muon spectrometer operates inside a 4 T magnetic field (not homogeneous) which is supplied by air-core toroid magnets.

Combining the information from each sub-detector, different types of particles can be identified. Figure 4.2 shows how each sub-detector responds to different types of particles. Charged particles leave tracks in the ID. Photons and electrons are captured by the electromagnetic calorimeter; by matching the tracks from the ID to electromagnetic calorimeter deposits, photons and electrons are identified. Charged hadrons leave tracks in the ID and both neutral and charged hadrons are stopped in the hadronic calorimeter. Muons pass through all sub-detector systems and leave tracks in the ID and the muon spectrometer. Muons also deposit a small amount of energy in the calorimeters. Therefore, muons can be identified either by the muon spectrometer alone or by combining sub-detector information. Neutrinos do not interact with the detector material meaning that they are invisible in all sub-detector systems; they give rise to missing momentum in the transverse detector plane.

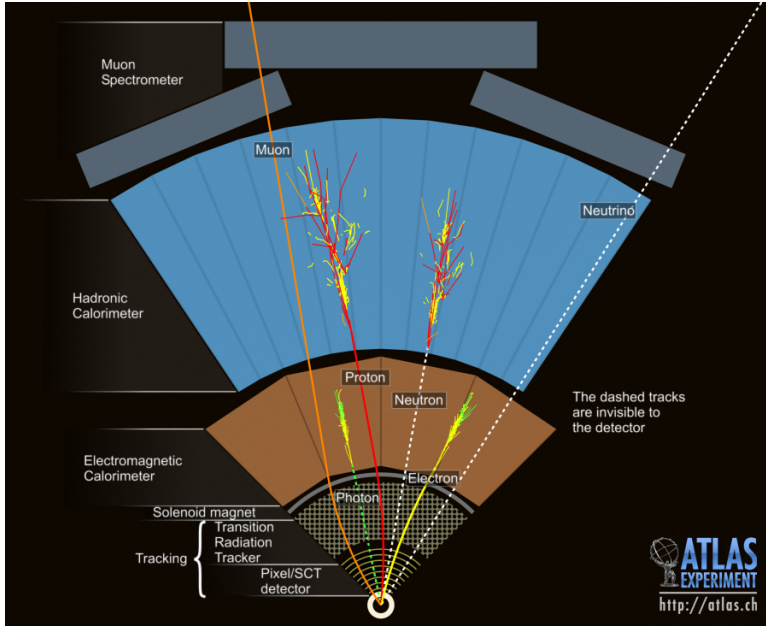


Figure 4.2: Transverse view of the ATLAS sub-detector system [90].

4.2 ATLAS Coordinate System

As mentioned before, the ATLAS detector has a cylindrically symmetric geometry. In the Cartesian coordinate system, the z axis is defined along the beam pipe, and it is pointing in the anti-clockwise beam direction, the x axis is defined to point to the center of the LHC ring, and the y axis is pointing upwards (see Figure 4.3(a)). The reference point is set to a selected proton-proton interaction point or, if such an interaction point is not available, to the center of the detector. In the spherical coordinate system, r is the radial distance to the reference point, the polar angle θ is measured in the y - z plane, and the azimuthal angle ϕ is measured from the x axis in the transverse plane. When describing the detector geometry and the Lorentz vector of particles, pseudorapidity and rapidity are often used instead of θ . The pseudorapidity is defined as

$$\eta = -\ln \left(\tan \frac{\theta}{2} \right) \quad (4.1)$$

As shown in Figure 4.3(b), the pseudorapidity is zero along the y axis, and along the z axis it approaches infinity. The pseudorapidity is used to describe the trajectories of

massless objects. For massive objects, the rapidity, defined as

$$y = \frac{1}{2} \ln \left(\frac{E + p_z}{E - p_z} \right) \quad (4.2)$$

is used since the rapidity difference is an invariant under a boost along the z axis.

Some kinematic variables are defined in the transverse plane such as transverse momentum p_T and transverse energy E_T . Another useful parameter is the angular distance, $\Delta R = \sqrt{\Delta\eta^2 + \Delta\phi^2}$, of two objects in the pseudorapidity-azimuthal angle space.

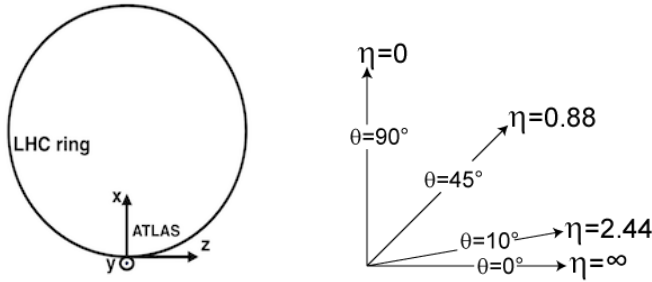


Figure 4.3: The ATLAS coordinate system (left), the values of pseudorapidity, η , for a polar angle θ of 0, 10, 45 and 90 degrees (right) [91].

Other important geometrical parameters are the traverse and longitudinal impact parameters of tracks with respect to a reference point, d_0 and z_0 . The d_0 is defined as the vector in the transverse plane from the reference point to the closest point on the track. The absolute value of d_0 is the distance of closest approach between the reference point and the track. The sign of d_0 is positive if the polar angle of the d_0 is equal to $\phi_0 + \frac{\pi}{2}$, where ϕ_0 is the polar angle of the track momentum vector. Figure 4.4 shows the positive d_0 parameter of a track. If the the polar angle of the d_0 is equal to $\phi_0 - \frac{\pi}{2}$ then its sign is negative. The z_0 is defined as the z coordinate of the point on the track closest to the reference point.

4.3 Inner Detector

The layout of the ID is illustrated in Figure 4.5; it is 6.2 m long and 2.1 m in diameter, and placed in a 2 T magnetic field. The ID itself is composed of three high granularity tracking sub-detectors, the pixel detector, the semiconductor tracker (SCT) and the transition radiation tracker (TRT). They are independent but complementary to each other.

Pixel detector: The pixel detector is the innermost tracking sub-detector. It consists of three barrel layers at average radii of 50.5 (B-layer), 88.5 and 122.5 mm from the

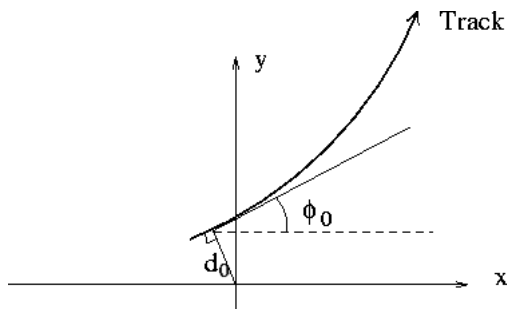


Figure 4.4: The positive d_0 parameter of a track [92].

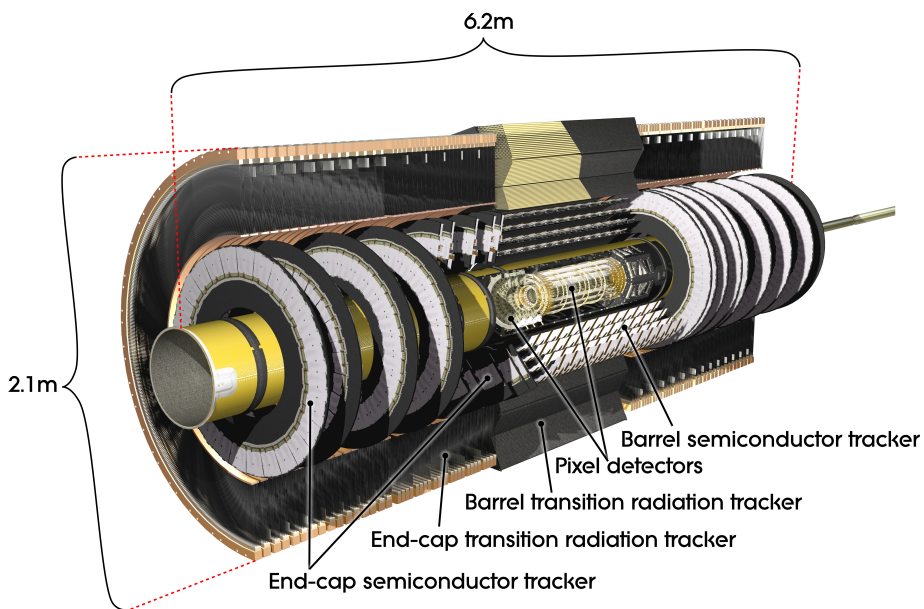


Figure 4.5: Cut-away view of the inner detector of ATLAS [93].

beam axis and three end-cap disks on each side located at 495, 580 and 650 mm from the interaction point along the z axis. The barrel and end-cap disks cover pseudorapidities of $|\eta| < 1.7$ and $1.7 < |\eta| < 2.5$ respectively, with full coverage in ϕ . The pixel detector provides high spacial resolution as it consists of 1744

modules and has approximately 80.4 million readout channels; the precision measured by such a high granularity is crucial for the primary and secondary vertex reconstruction. Since the pixel detector operates in high radiation conditions, it must be replaced after approximately three years of running.

One additional layer, the insertable B-layer (IBL) [94, 95], was installed during the shutdown after Run 1. The IBL, being a fourth layer of the pixel detector and the closest layer to the interaction point, aims at improving tracking and vertexing performance in high-pileup conditions and consequently, also improving b -tagging (see Section 6.3) performance. The IBL is a high granularity pixel layer consisting of 180 modules mounted on 14 staves which cover the full azimuthal angle, ϕ . The IBL staves are mounted directly on the beam pipe, at a radius of about 3.3 cm. Each staff is 64 cm long and covers a pseudo-rapidity of $|\eta| < 2.9$. The IBL has approximately 12 million readout channels.

SCT: The SCT is placed outside of the pixel detector. It uses silicon microstrip modules organized in the four cylindrical layers of the SCT barrel and the nine end-cap disks. Each layer is made of two sub-layers of modules which are rotated with respect to each other to provide 3-dimensional information. The SCT barrel covers $|\eta| < 1.4$ and the end-cap disks cover $1.4 < |\eta| < 2.5$. The SCT system has approximately 6.3 million readout channels.

TRT: The TRT is located outside the SCT and provides tracking over a large volume. It consists of a barrel and two end-caps. The TRT barrel covers $|\eta| < 0.7$ while the end-caps allow tracking up to $|\eta| < 2.0$.

The TRT is a straw-tube detector which is made of transition radiation material. Each straw tube is 4 mm in diameter; it is 144 cm long in the barrel and 37 cm long in the end-caps. A straw tube is filled with a gas mixture of 70% Xe, 27% CO₂ and 3% O₂. Charged particles ionize the gas inside the tube. The wall of the straw tube is made of polyamide which enhances the photon emission of charged particles passing through it. The amount of radiation depends on the particle mass. Therefore, in addition to providing measurements used for tracking, the TRT also provides information to identify electrons and charged pions. The TRT only provides $r - \phi$ information and has approximately 351000 readout channels.

These three sub-detectors (see Figure 4.6) provide high resolution measurements of the particle trajectories up to $|\eta| < 2.5$. This information is critical to determine the momenta of charged particles as well as to reconstruct primary and secondary vertices. The combined ID provides a momentum resolution, $\sigma(p_T)/p_T \simeq 0.05\% p_T/\text{GeV} \oplus 1\%^1$, depending on the p_T of the particles.

¹⁾The symbol \oplus refers to the quadratic sum.

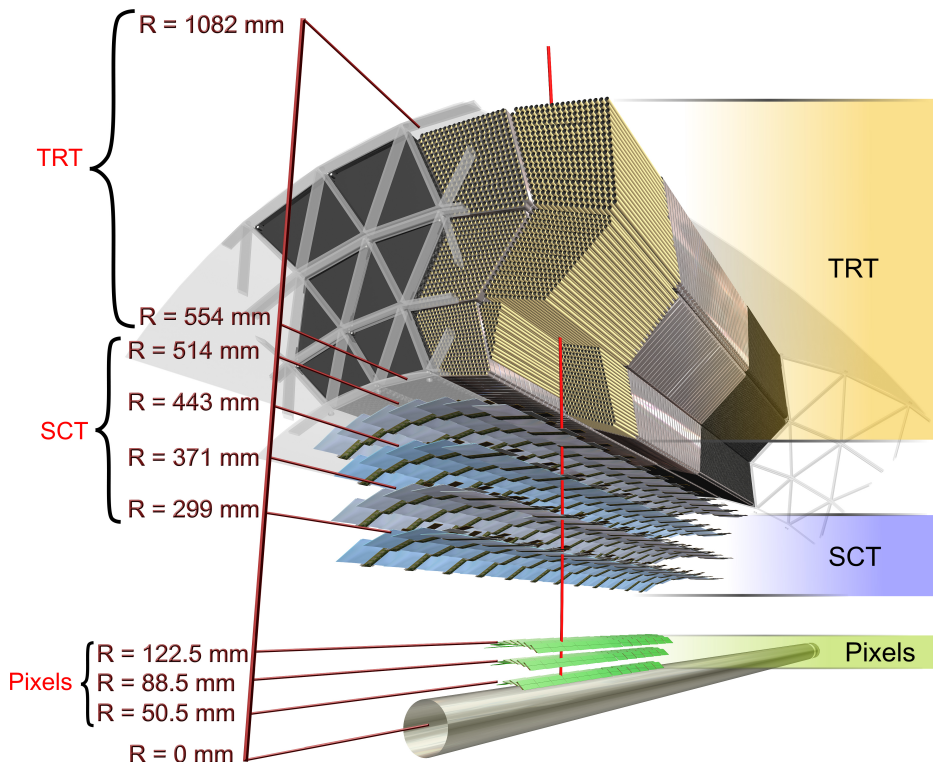


Figure 4.6: A cross section of the barrel region of the ATLAS inner detector [93]. The picture shows the radial positions of the barrel layers in the pixel detector, SCT and TRT. The z axis is oriented along the beam pipe.

4.4 Calorimeters

The calorimeters measure the energy of particles by stopping them in the calorimeter material; this requires the calorimeter to be large. The ATLAS detector uses sampling calorimeters which are composed of passive and active materials placed in a sandwich

structure. The passive materials are dense and have shorter radiation (or interaction) length. The active materials have lower density, and their main function is generating measurable signals which will be read out from the detectors.

The entire ATLAS calorimeter covers $|\eta| < 4.9$ and consists of an electromagnetic and a hadronic calorimeter. The electromagnetic calorimeter uses lead plates as the passive material and liquid argon (LAr) as the active material to measure electromagnetic showers from photons and electrons. The electromagnetic calorimeter is designed with accordion-shaped absorbers and electrodes which allow the calorimeter to have several active layers in depth. The LAr electromagnetic calorimeter is divided into three components: a LAr barrel, which covers $|\eta| < 1.475$ and two end-caps which cover $1.375 < |\eta| < 3.2$. In the part corresponding to the coverage of the ID ($|\eta| < 2.5$), it is segmented into three segments in depth. The granularity of the detector in this region is suited for precision measurements of electrons and photons. In the two forward sections ($2.5 < |\eta| < 3.2$), the granularity is sufficient for the physics requirements of jet reconstruction and missing transverse energy measurements. The relative energy resolution provided by the electromagnetic calorimeter is $\sigma(E)/E \simeq 10\%/\sqrt{E/\text{GeV}} \oplus 0.7\%$.

Hadronic showers are measured in the hadronic calorimeter which is composed of the tile calorimeter in the central region and the hadronic end-cap calorimeter (HEC) and the liquid-argon forward calorimeter (FCal) in the forward region. The tile calorimeter uses an iron-scintillating-tile technique with steel as the passive material and scintillating tiles as the active material. The tile calorimeter is placed outside the electromagnetic calorimeters in the central region and covers the range $|\eta| < 1.7$. The tile calorimeter itself is subdivided into a central barrel and two extended barrels. The HEC consist of two independent wheels per end-cap, located outside the electromagnetic end-cap calorimeters, and covers the range $1.5 < |\eta| < 3.1$. The FCal is based on LAr technology and covers the range $3.1 < |\eta| < 4.9$. In the barrel and end-cap regions of the hadronic calorimeter the relative resolution is $\sigma(E)/E \simeq 50\%/\sqrt{E/\text{GeV}} \oplus 3\%$, while in the forward region the relative resolution is $\sigma(E)/E \simeq 100\%/\sqrt{E/\text{GeV}} \oplus 10\%$.

4.5 Muon Spectrometer

The MS is the outermost sub-detector system of the ATLAS detector. It identify muons and measures their momenta. Just as for the ID, the MS measures momenta by bending the muon trajectories in a magnetic field. In the range $|\eta| < 1.4$, the magnetic field is provided by eight large superconducting air-core toroid magnets; in the range $1.6 < |\eta| < 2.6$, the magnetic field is provided by two smaller end-cap toroids. In the transition region $1.4 < |\eta| < 1.6$, the magnetic field is a combination of the barrel and end-cap magnetic fields. With this configuration, the magnetic field is mostly orthogonal to the muon trajectories.

The MS consists of three cylindrical layers in the barrel region; in this region, the track bending is measured by monitored drift tubes (MDTs). The MDTs cover $|\eta| < 2.7$

($|\eta| < 2.0$ in the innermost layer). In the end-cap, the MS has three vertical wheels perpendicular to the beam; in this region, high granularity cathode strip chambers (CSC) are used which provide tracking in the range $2.0 < |\eta| < 2.7$.

The momentum resolution of the muon spectrometer does not depend on muon p_T for high- p_T muons and is $\sigma(p_T)/p_T \lesssim 10\%$ for muon p_T up to 1 TeV.

4.6 Trigger and Data Acquisition

The trigger and data acquisition (collectively TDAQ) systems, the timing- and trigger-control logic, and the detector control system (DCS) are partitioned into sub-detector systems.

The LHC bunch crossing rate is 40 MHz at nominal design luminosity. This corresponds to approximately 1.5 PB s^{-1} of raw data which means that it is impossible to store all the data from the detector. The ATLAS trigger system is designed to filter the collision events and reduce the rate down to approximately 200 Hz at which events are written to permanent data storage.

ATLAS has three distinct trigger levels, L1, L2 and the event filter, as well as a data acquisition system (Figure 4.7). Each trigger level makes a decision based on the output of the previous level. The L1 searches for leptons, photons, jets, hadronically decaying τ leptons and large missing transverse energy using a limited amount of information from the sub-detectors. With this information, it defines so-called regions-of-interest (RoIs) where the possible trigger objects are found. The L1 information from the sub-detectors is processed by the central trigger processor which implements the trigger selections. The desired L1 trigger rate is 100 kHz.

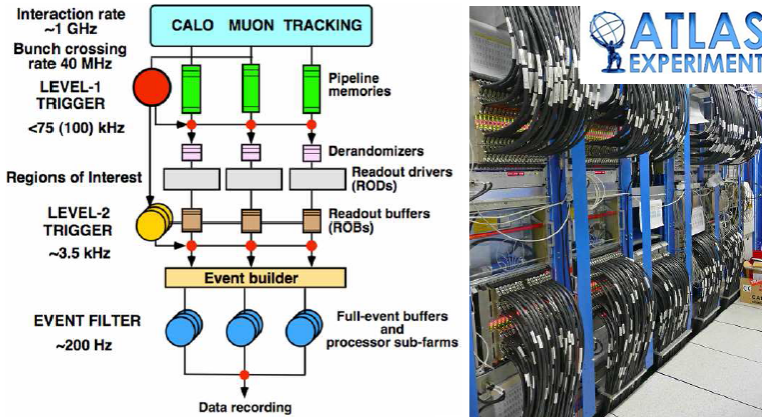


Figure 4.7: Block diagram of the ATLAS trigger and data acquisition system [96].

Events passing the L1 trigger selection are sent to the next stages of the detector-

specific electronics and subsequently to the data acquisition via point-to-point links. In the next step, the L2 trigger is seeded by RoI information from the L1 triggers, such as coordinates, energy and type of signatures. The L2 uses all available detector data in the RoIs to select events and reduces the event rate to less than 3.5 kHz. The events that pass the L2 criteria are sent to the event filter which performs the final event selection. The event filter uses offline analysis procedures on the complete event information and reduces the event rate down to approximately 200 Hz. Finally, the events selected by the event filter are moved to permanent event storage at CERN's computer center.

5 Data Sets and Simulated Samples

This chapter summarizes the data sets and Monte Carlo (MC) simulations which are used in the analyses described in this thesis. In Section 5.1, the data sets recorded by the ATLAS detector are described. In Section 5.2, MC simulated samples which correspond to data sets at various center of mass energies are described.

5.1 Data Sets

Four sets of data have been collected by the ATLAS detector with different conditions in Run 1 and Run 2. Figure 5.1 shows the integrated luminosities in 2011, 2012, 2015 and 2016 corresponding to data taking at 7 TeV, 8 TeV and 13 TeV center of mass energies respectively. In 2011 and 2012, the proton bunches collided with 50 ns bunch spacing while in 2015 and 2016 the bunch spacing was 25 ns.

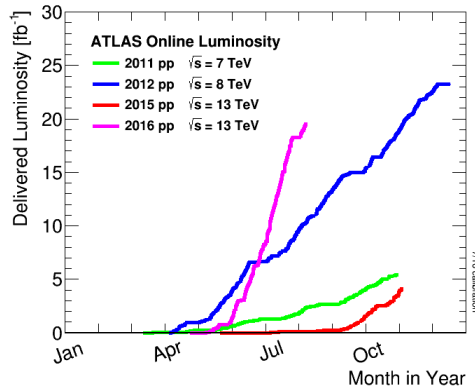


Figure 5.1: Integrated luminosity versus time delivered to ATLAS detector [87].

In 2011, the ATLAS detector recorded 5.1 fb^{-1} of data at the center of mass energy $\sqrt{s} = 7 \text{ TeV}$, and 4.6 fb^{-1} of data are selected as good for physics. The data collected early in the year, period E, has low pileup conditions while data collected later in the year, period M, has high pileup conditions. The period E and period M are were used in the primary vertex reconstruction performance study in chapter 7.

In 2012, the LHC raised the center of mass energy up to $\sqrt{s} = 8 \text{ TeV}$. In this year, the ATLAS detector recorded 21.3 fb^{-1} of data, and 20.3 fb^{-1} of data are selected as good for physics. The total uncertainty on the luminosity is 2.8%. This entire data set was used in the analysis presented in chapters 9 and 10.

In 2015 and 2016, the LHC operated at $\sqrt{s} = 13 \text{ TeV}$. In these years, the ATLAS detector recorded 3.2 fb^{-1} and 10 fb^{-1} (up until July) of data which fulfill the quality requirements and is selected as good for physics. The total uncertainties on the luminosities are in the range of 2-5%. These data sets were used in the analyses described in chapters 11 and 12.

5.2 Monte Carlo Simulation

In the SUSY analyses, MC simulation is used to estimate the number of events from SM background processes and the composition of the background to perform shape studies (kinematic distributions). It is also used in the optimization of selection criteria. MC samples are generated in such a way that they describe data at the various center of mass energies. In the simulations pileup effects are also taken into account. The MC samples are reweighted based on the average number of interactions per bunch crossing, $\langle \mu \rangle$, so that the number of MC pileup interactions are matched the data. MC events are generated using MC event generators; their parameters were tuned to ATLAS data. Then, these events are processed through the GEANT4 [97] detector simulation. Physics objects in the events without the GEANT4 detector simulation are called generator-level objects; after the detector simulation they are referred to as reco-level objects.

5.2.1 Standard Models Samples

The SM processes which are relevant for the analyses in this thesis are t quark pair production ($t\bar{t}$), associated production of a t quark pair and a vector boson ($t\bar{t} + W/Z/\gamma^*$), single t production, W/Z boson production with additional jets and diboson (VV) production.

- In the study with $\sqrt{s} = 7 \text{ TeV}$ data in chapter 7, only $t\bar{t}$ and $Z \rightarrow \mu\mu$ events are used. The $t\bar{t}$ events are generated with the MC@NLO [98] event generator interfaced to JIMMY [99] for parton shower and hadronisation. The $Z \rightarrow \mu\mu$ events are generated with the Pythia [100] event generator. The cross sections of the simulated processes are calculated up to next-to-leading order (NLO) in QCD including next-to-next-to-leading logarithmic (NNLL) soft gluon terms for the

$t\bar{t}$ sample, and next-to-next-to-leading order (NNLO) accuracy for the $Z \rightarrow \mu\mu$ sample.

- At $\sqrt{s} = 8$ TeV, $t\bar{t}$ events are generated with POWHEG v2129 [101] using a t mass value, m_t , of 172.5 GeV. The cross section is calculated up to NNLO+NNLL using top++2.0 [102–107]. The simulated $t\bar{t}$ events are reweighted according to the p_T of the $t\bar{t}$ system which was measured by ATLAS at 7 TeV [108]. The s -channel and the Wt channel single t quark events are generated with POWHEG v2129 while the t -channel is generated with AcerMC-3.8 [109]. The total cross section is calculated at NLO+NNLL precision. The $t\bar{t} + V$ and single t associated with a Z boson are generated with MadGraph-5.1.4.8 [110] with up to two additional partons. The $t\bar{t} + V$ cross section is calculated at NLO and the cross section for single t production associated with a Z boson is calculated at LO precision. The $W/Z/\gamma^* + \text{jets}$ and diboson processes are generated with the SHERPA-1.4.1 [111] generator; the $W/Z/\gamma^* + \text{jets}$ are generated with up to four additional partons. The cross section for the $W/Z/\gamma^* + \text{jets}$ production is calculated at NNLO precision with DYNLO [112] while the cross section of the diboson process has NLO precision and is calculated with MCFM [113, 114]. All MC samples generated by the POWHEG and SHERPA generators use the CT10 [115] parton distribution function (PDF) set at NLO. The other samples use the CTEQ6L1 [116] PDF set in the event generation.
- At $\sqrt{s} = 13$ TeV, the $t\bar{t}$ and single t MC samples are generated with POWHEG-Box v2 [117–121] event generator interfaced to Pythia 6 [122] for parton shower and hadronization. The cross sections are calculated at NNLO+NNLL accuracy. The $W/Z + \text{jets}$ samples are produced with the SHERPA-2.1.1 [111] generator for the analysis described in Chapter 11 and they are produced with SHERPA-2.2 [111] for the analysis described in Chapter 12. The diboson samples are produced with the SHERPA-2.1.1 generator. The $W/Z + \text{jets}$ cross sections are calculated at NNLO while the diboson cross section is calculated at NLO accuracy. The $t\bar{t} + W/Z/\gamma$ MC samples are produced with MG5_aMC-2 [123] and interfaced to Pythia 8 [124]; the cross sections are calculated at NLO order. In the event generation, the CT10 PDF set is used with the POWHEG and SHERPA generators while the NNPDF-2.3 set [125] is used for MG5_aMC-2 except for the $t\bar{t} + \gamma$ sample where the CTEQ6L1 PDF set is used.

5.2.2 Signal Samples

Models where the supersymmetric top quarks are directly produced as well as pMSSM models and vector-like top quark models are used to interpret the results of the analyses described in Chapters 9, 10, 11 and 12.

- In the $\sqrt{s} = 8$ TeV analysis, the signal samples of direct stop pair production use different generators for different decay modes; each decay mode has 100%

branching ratio. For $\tilde{t}_1 \rightarrow t\tilde{\chi}_1^0$ and three-body ($\tilde{t}_1 \rightarrow bW\tilde{\chi}_1^\pm$) decays, signal samples are generated with the HERWIG++ [126] event generator. For $\tilde{t}_1 \rightarrow b\tilde{\chi}_1^\pm$ and four-body ($\tilde{t}_1 \rightarrow bff'\tilde{\chi}_1^\pm$) decays, MadGraph is used for the generation in which the W boson is on-shell while for the \tilde{t}_1 decays with an off-shell W boson Pythia 6 is used. The signals are sampled in a grid in the \tilde{t}_1 and $\tilde{\chi}_1^0$ mass plane with a 50 GeV step size; however, in the diagonal regions (small mass difference between \tilde{t}_1 and $\tilde{\chi}_1^0$), the signals are sampled with higher granularity. The pMSSM models enriched in 3^{rd} generation squarks and the pMSSM models with fixed stop and LSP masses are generated with the HERWIG++ generator. The general pMSSM models used for the interpretation of all ATLAS Run 1 SUSY searches are generated with MadGraph interfaced to Pythia 6 with the CTEQ6L1 PDF set. Cross sections of all models are calculated at NLO+NLL accuracy.

- At $\sqrt{s} = 13$ TeV, the $\tilde{t}_1 \rightarrow t\tilde{\chi}_1^0$ and the gluino-mediated \tilde{t}_1 samples are generated with MG5_aMC-2. The vector-like top quark model is generated with Protos v2.2 [127]. The generators are interfaced to Pythia 8, and the NNPDF-2.3 set is used; the cross sections are calculated at NLO+NLL for the $\tilde{t}_1 \rightarrow t\tilde{\chi}_1^0$ and the gluino-mediated \tilde{t}_1 models, and at NNLO+NNLL for the vector-like top quark model.

6 Event Reconstruction

Events are reconstructed using information collected from each sub-detector. In this thesis, the $\sqrt{s} = 8$ TeV and $\sqrt{s} = 13$ TeV analyses select a final state with exactly one charged lepton. Therefore, events are reconstructed by requiring at least one reconstructed vertex, exactly one electron (e) or muon (μ), several jets and large missing transverse energy (E_T^{miss}). Object reconstruction and identification is described in sections 6.1 - 6.8. Overlap removal (OR) can resolve ambiguities of the reconstruction, as is described in section 6.9.

6.1 Tracks

Tracks are reconstructed in the ID [128]. The tracking starts by seeding the inside-out pattern recognition algorithm with three hits in the silicon detectors (pixel detector + SCT), then adds more hits while moving away from the primary interaction point. After resolving ambiguities in the track candidates, tracks are extended to the TRT. In the next steps, a back-tracking starts from the TRT segments not used by the inside-out tracking, and extends them inwards by adding hits in the silicon detectors. The back-tracking is designed to find tracks originating from secondary vertices. A TRT track that does not match any track in the silicon detectors is defined as a TRT-standalone track.

Reconstructed tracks are further selected by requiring $p_T > 400$ MeV in the central region $|\eta| < 2.5$, and a minimum number of hits in the pixel detector and SCT [129]. In the loose selection criteria, at least seven silicon hits are required with maximum two holes in the silicon detectors and maximum one hole in the pixel detector. A hole is a “missing hit” on the track where a track trajectory intersects with a sensitive detector element without any resulting hits. In the tighter selection, in addition to the loose selection criteria, at least nine silicon hits in the range $|\eta| < 1.65$ and 11 silicon hits in the range $|\eta| > 1.65$ are required. At least one hit in the pixel detector B-layer or IBL (this is added in Run 2) and no holes in the other layers of the pixel detector is also required.

6.2 Primary Vertex

A primary vertex is an estimated proton-proton collision point inside the ATLAS detector. The number of primary vertices in each bunch crossing is not a constant value, but follows a Poisson distribution with an average that depends on the instantaneous luminosity of the LHC.

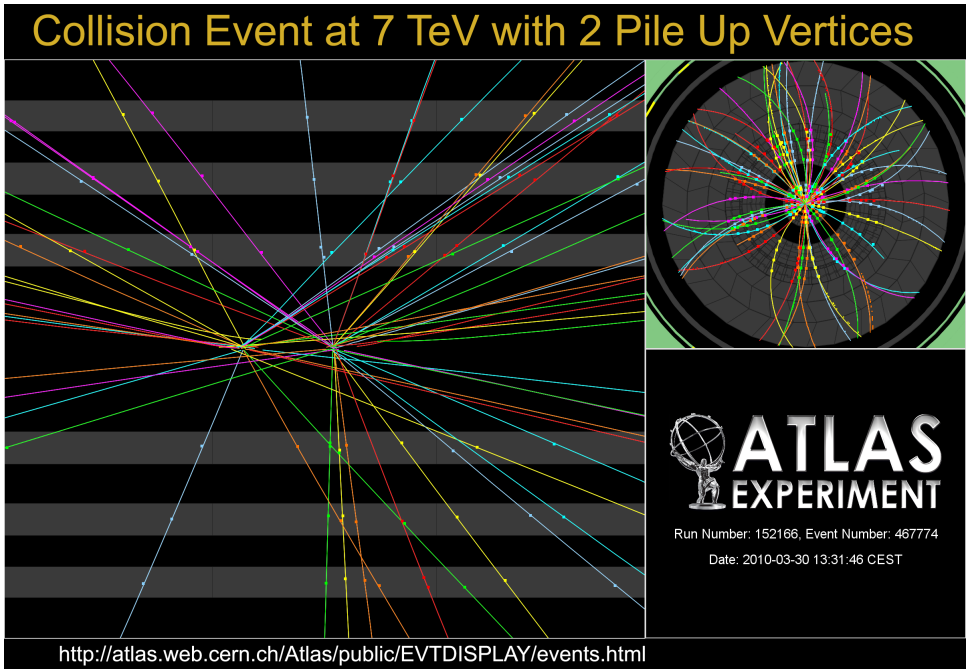


Figure 6.1: Display of a 7 TeV event with two inelastic proton-proton collisions.

The primary vertex is reconstructed using the tracks of charged particles in the ID. The reconstruction [130, 131] consists of two steps: vertex finding and vertex fitting. In the first step, tracks are selected according to their longitudinal impact parameter z_0 with respect to the origin (here the center of the detector) and form clusters in z_0 as shown in Figure 6.1. These clusters are considered as independent primary vertex candidates and provide the initial inputs to the algorithm which finds and fits the primary vertex candidates. The tracks used in the final primary vertex fit are said to be associated with that vertex. In the second step, the actual position of the primary vertex is reconstructed, and the quality of the fit is estimated. Based on the contribution to the χ^2 of the vertex fit, outlier tracks are removed from the set of tracks used in the fit; then the primary vertex is refitted. The procedure is repeated until no outliers are left.

Among all the reconstructed primary vertices, the one believed to be the hard-scatter vertex which corresponds to the proton-proton collision giving rise to the process of interest, is chosen as the one with the largest $\sum_{\text{tracks}} p_T^2$, where tracks refer to those associated to this vertex. The primary vertices other than the hard-scatter vertex are referred to as pileup vertices.

6.3 Jets

Jets are made of hadrons and other particles which are produced by the hadronization of a gluon or quark and tend to travel in approximately the same direction.

Jets are constructed from three-dimensional, noise-suppressed, topological clusters in the calorimeters. The clustering starts with a cell that has a ratio of the energy deposit and its noise above a certain threshold. Then, neighboring calorimeter cells that have significant energy deposits compared to the expected noise are grouped into the clusters. Using these clusters, jets are reconstructed by the anti- k_t jet clustering algorithm [132] with a distance parameter of 0.4. The reconstructed jet candidates are calibrated [133] to account for the effects from e.g. the calorimeter non-compensation and inhomogeneities using calibration factors which depend on the energy and η of the jets. There are several reasons for calorimeter non-compensation. The calorimeters have a different response for electromagnetic and hadronic constituents of the jets. The energy losses in inactive regions and the energy deposits which are below the noise threshold are not used in the jet reconstruction. The longitudinal energy leakage of the shower also causes the energy loss in the calorimeters. In addition, particles from pileup interactions also affect jet energies; these additional particles increase the jet energy response and make it luminosity-dependent.

Calibration factors (Equation 6.1) are derived from simulation. In the simulation, truth jets are formed using stable (lifetime > 10 ps) truth particles produced in the fragmentation model in the MC generator. Then the reconstructed jet energy is calibrated, on average, to the corresponding truth jet energy. The calibration factors are defined by

$$R(E, \eta) = \left\langle \frac{E_{\text{reco}}}{E_{\text{truth}}} \right\rangle \quad (6.1)$$

where E_{reco} is the reconstructed jet energy and E_{truth} is the truth jet energy. The jet energy calibration also corrects for pileup effects. The calibration is validated with test-beam and collision data.

In the $\sqrt{s} = 8$ TeV and $\sqrt{s} = 13$ TeV analyses, jets with $p_T > 20$ GeV and $|\eta| < 2.5$ are considered as jet candidates.

A hadronically decaying t quark with a large p_T can have all its decay products being efficiently captured by a single large-radius jet (large- R jet). This is exploited in analyses targeting final states with boosted t quarks. Therefore, large- R jets [134] are

reconstructed using the anti- k_t jet clustering algorithm with a distance parameter of 1.0 or 1.2.

Jets containing b -hadrons are identified as b jets. The b -jet identification is based on both impact parameter and secondary vertex information. In Run 1, ATLAS used the MV1 b -tagging algorithm which is based on an artificial neural network to combine the inputs from the impact parameter-based algorithm (IP3D), the JetFitter+IP3D algorithm, and the secondary vertex-based algorithm (SV1) [135], to identify jets as b jets. In Run 2, the multivariate tagging algorithm MV2c20 [136] is used. This algorithm is similar to MV1 but is based on a boosted decision tree (BDT) which is trained to discriminate also against c jets. In both cases, by cutting on the output weight of the algorithms, one can discriminate b jets from light jets and c jets. Different cut values provide different b -tag efficiencies and light- and c -jet rejection rates. These cut values are referred to as “operating points”.

In the $\sqrt{s} = 8$ TeV analysis, the operating points corresponding to efficiencies of 70, 75 and 80% are primarily used; in the $\sqrt{s} = 13$ TeV analysis a b -tag operating point at 77% b -tag efficiency is used¹⁾.

6.4 Electrons

Electrons are reconstructed from energy deposits in the electromagnetic calorimeter; the energetic cells form clusters that are matched to tracks in the inner detector in the central region, $|\eta| < 2.47$. The reconstructed electrons must pass the identification criteria which aim to discriminate true electrons from jets with a large electromagnetic component.

In the $\sqrt{s} = 8$ TeV analysis, the electron candidates are required to have $p_T > 10$ GeV and are further classified as “loose”, “medium” or “tight” electrons [137]. The “loose” selection has less jet rejection power while the “tight” selection has higher jet rejection power. The electron candidates are considered as signal electrons if they have $p_T > 25$ GeV and are isolated from other activity in the detector by requiring the scalar sum of the p_T of all tracks (not including the electron itself) within a distance $\Delta R = 0.2$ from the electron to be less than 10% of the electron p_T .

In the $\sqrt{s} = 13$ TeV analysis, electron candidates have $p_T > 7$ GeV and have to satisfy the “VeryLoose” likelihood identification criteria [138]. Signal electrons are selected among the electron candidates by requiring them to satisfy impact parameter requirements with respect to the primary vertex $|z_0 \sin \theta| < 0.5$ mm and $|d_0/\sigma_{d_0}| < 5$ (σ_{d_0} is the uncertainty on the d_0), $p_T > 25$ GeV, the “Loose” likelihood identification criteria in [138] and a track-based isolation criterion [138].

¹⁾The given efficiencies correspond to the inclusive efficiencies in a simulated $t\bar{t}$ sample.

6.5 Muons

Muons are reconstructed using information from the ID, MS and calorimeter sub-detectors. Four types of muons are defined: combined (CB) muons, segment-tagged (ST) muons, stand-alone (SA) muons, and calorimeter-tagged (CT) muons. The CB muons are reconstructed by combining tracks in the MS to matched tracks in the ID. The ST muons are reconstructed from tracks in the ID matched to at least one local track segment in the MS. The SA muons are reconstructed only in the MS. The CT muons are reconstructed from tracks in the ID matched to an energy deposit in the calorimeter compatible with a minimum ionizing particle.

In the $\sqrt{s} = 8$ TeV analysis, muon candidates are required to have $|\eta| < 2.4$ and $p_T > 10$ GeV. The muons candidate are considered as signal muons if $p_T > 25$ GeV. The signal muons must also be isolated by requiring the scalar sum of the p_T of all tracks (not including the muon itself) within a distance $\Delta R = 0.3$ from the muon to be less than 1.8 GeV.

In the $\sqrt{s} = 13$ TeV analysis, muon candidates are required to have $p_T > 6$ GeV, $|\eta| < 2.7$, and to satisfy the “Loose” identification criteria [139]. Signal muons are further required to have impact parameters $|z_0 \sin \theta| < 0.5$ mm and $|d_0/\sigma_{d_0}| < 3$, $p_T > 25$ GeV and satisfy a track-based isolation criterion.

6.6 Hadronically Decaying τ Leptons

Hadronically decaying τ leptons are reconstructed as jets but use a separate energy calibration. The τ candidates are required to have $p_T > 15$ GeV, to be in the central region $|\eta| < 2.47$ and to have one or three tracks associated with the corresponding jet. The τ identification uses a BDT, which takes the transverse and longitudinal shapes of the energy deposits in the calorimeters as inputs [140]. In the $\sqrt{s} = 13$ TeV analysis, the τ candidates are in addition required to pass “Loose” identification criteria [141] which have a 60% (50%) efficiency for identifying a τ lepton decaying into one (three) charged pions.

6.7 Photons

Photon candidates are not used in the main event selections of the analyses presented in this thesis, but are used in background estimations. Photons are reconstructed in the same way as electrons but without the requirement on the ID track match. In the $\sqrt{s} = 8$ TeV analysis, photon candidates must have $p_T > 20$ GeV, be reconstructed in the central region $|\eta| < 2.47$ and satisfy “tight” identification criteria [142]. In the $\sqrt{s} = 13$ TeV analysis, photon candidates are required to have $p_T > 125$ GeV in the analysis in Chapter 11 and 145 GeV in the analysis in Chapter 12, be reconstructed within $|\eta| < 2.37$ and to pass “Tight” identification criteria [143].

6.8 Missing Transverse Energy

The missing transverse energy, E_T^{miss} , is defined as the magnitude of the missing transverse momentum vector, \vec{p}_T^{miss} . The missing transverse momentum vector is measured from the momentum imbalance in the transverse plane of the detector as the negative sum of the transverse momenta of electrons, muons and jets candidates. In addition, calibrated calorimeter clusters not assigned to these physics objects are added to the E_T^{miss} calculation in the $\sqrt{s} = 8$ TeV analysis while tracks that are not associated to reconstructed objects are included in the E_T^{miss} calculation in the $\sqrt{s} = 13$ TeV analysis.

6.9 Overlap Removal

There are some ambiguities in the object reconstruction procedure. For example, an electron will also be reconstructed as a jet in the calorimeters. Unless this ambiguity is resolved, this will lead to a double counting of the energies of the calorimeter cells that are shared by the electron and jet candidates. The purpose of the overlap removal is thus to resolve these ambiguities.

In the $\sqrt{s} = 8$ TeV analysis the overlap removal is designed as follows, and applied in the order specified:

- If a jet candidate overlaps with an electron candidate within $\Delta R < 0.2$, the jet is removed and the electron is kept, unless the jet is b -tagged in which case the jet is kept and the electron is removed.
- A lepton candidate which overlaps with any jet within $\Delta R < 0.4$ ($0.2 < \Delta R < 0.4$ for electrons) is removed.
- A τ lepton candidate which overlaps with any other lepton (electron or muon) candidate within $\Delta R < 0.2$ is removed.

In the $\sqrt{s} = 13$ TeV analysis the following overlap removal is used:

- If a muon overlaps with any electron within $\Delta R < 0.01$, the electron is removed and the muon is kept, unless the muon is calo-tagged, in which case the electron is kept and the muon is removed.
- If a jet candidate overlaps with an electron candidate within $\Delta R < 0.2$, the jet is removed and the electron is kept, unless the jet is b -tagged in which case the jet is kept and the electron is removed.
- A jet that overlaps with a muon within $\Delta R < 0.2$ is removed and the muon is kept, unless the jet is b -tagged and has either more than three associated tracks or $p_T^\mu / p_T^{\text{jet}} > 0.7$, in which case the jet is kept and the muon is removed.

- An electron or muon (ℓ) is removed if it overlaps with any jet within $\Delta R(\ell, \text{jet}) < \min\{0.4, 0.4 + \frac{10 \text{ GeV}}{p_T^\ell}\}$.
- A jet which overlaps with a photon (γ) within $\Delta R(\gamma, \text{jet}) < 0.2$ is removed. This step is only applied in event selections including a photon.
- A photon which overlaps with and an electron within $\Delta R(\gamma, e) < 0.1$ is removed. This step is only applied in event selection including a photon.
- A τ lepton which overlaps with a jet within $\Delta R(\gamma, \tau) < 0.1$ is removed. This step is only applied in event selection including a photon.

Part III

Primary Vertex Studies

7 Primary Vertex Reconstruction Performance in Dimuon Events

This chapter presents a study of the primary vertex performance using $t\bar{t}$ and Z events with two muons. The main purpose is to compare the performance in data to that in simulated events to ensure that the simulation properly models the primary vertex performance in both low and high pileup conditions.

In this study data recorded by the ATLAS detector in 2011 is compared to simulated $t\bar{t}$ and Z events. The method with which this is done is described in more detail in Section 7.1. The event selection criteria used are described in Section 7.2 while the results are presented in Sections 7.3 and 7.4.

7.1 Vertex Classification Methods

As illustrated in Figure 7.1, the proton-proton interaction point is reconstructed using the tracks in the ID. In the ideal case, tracks from one truth interaction are used to reconstruct one vertex (see Figure 7.1 (a)). But sometimes the tracks from one truth interaction are used to reconstruct more than one vertex (see Figure 7.1 (b)). The latter case is referred to as a split vertex.

7.1.1 The Dimuon Method

Split vertices can be studied using physics processes giving rise to two prompt muons. Examples of such processes are $Z \rightarrow \mu^+ \mu^-$ and $t\bar{t} \rightarrow W^+ b W^- \bar{b} \rightarrow \mu^+ \nu b \mu^- \bar{\nu} \bar{b}$. These events are said to contain a split vertex if the two selected muons are associated with different reconstructed vertices as illustrated in Figure 7.1 (b).

It should be noted that the dimuon method is only sensitive to a subset of all split vertices as an event in which the two muons are associated to the same reconstructed vertex can have a second vertex reconstructed from tracks originating from the same truth interaction as the muons. But the strength of this method is that it can be applied

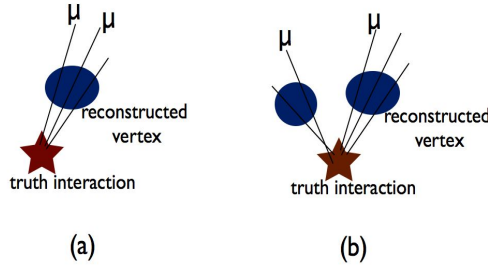


Figure 7.1: Tracks from one truth interaction are associated with a single reconstructed vertex (a). Tracks from one truth interaction are associated with different reconstructed vertices (b).

to both data and simulation, allowing for a direct comparison of the split vertex rates in the two cases.

7.1.2 The Truth-Matching Method

The truth-matching method [144] operates on simulated events only and matches particles at generator level (so called truth particles) to reconstructed tracks and classifies the reconstructed primary vertices as matched, merged, split or fake depending on the level of contribution from the tracks originating from the various generated proton-proton interactions (so called truth interactions) in the event. The classification is done as follows:

MATCHED vertex: at least 70% of the tracks associated with a reconstructed primary vertex originate from the same truth interaction.

MERGED vertex: one reconstructed primary vertex has contributions from two or more truth interactions and the sum of the contributions from these truth interactions is at least 70%.

SPLIT vertex: more than one primary vertex is reconstructed from the tracks originating from the same truth interaction and the contribution from this truth interaction is at least 70% in each reconstructed vertex. The vertex with the highest $\sum p_T^2$ of the tracks is referred to as the mother vertex and the others are called split vertices.

FAKE vertex: at least 70% of the tracks which contribute to the reconstructed primary vertex are fake tracks.

7.2 Object and Event Selection

From Equation 3.2 it follows that the expected number of events N_p^{sc} from a given physics process p after a set of selection criteria sc is given by

$$N_p^{sc} = L_{\text{int}} \times \sigma_p \times \varepsilon_p^{sc} \quad (7.1)$$

where L_{int} is the integrated luminosity of the data set, σ_p is the cross section for process p and ε_p^{sc} is the selection efficiency of the criteria sc for events from the process p . The selection criteria used are defined below.

7.2.1 Jet Selection

The jets are required to have $p_T > 25$ GeV and $|\eta| < 2.5$. Furthermore, the jet vertex fraction (JVF), defined as the summed transverse momenta of the tracks associated to a jet consistent with originating from the selected primary vertex divided by the summed transverse momenta of all tracks associated to a jet, is required to be larger than 0.75.

7.2.2 Muon Selection

Muons are reconstructed by combining a track measured in the ID with information in the muon system. The muon selection criteria are identical for the $t\bar{t}$ and Z event selections. The transverse momentum, p_T , of the muons is required to be greater than 20 GeV and the absolute value of the pseudorapidity, $|\eta|$, is required to be less than 2.5. The ID track matched to the muon is required to fulfill the following criteria:

- Number of B-layer hits > 0 in the pixel detector.
- Number of pixel hits plus number of crossed dead pixel sensors > 1 .
- Number of SCT hits plus number of crossed dead SCT sensors ≥ 6 .
- Number of pixel holes plus number of SCT holes < 3 , where a hole is an expected hit which has not been assigned to the track.
- Total number of TRT hits, $N_{\text{TRT}} = N_{\text{TRT}}^{\text{hits}} + N_{\text{TRT}}^{\text{outlier}}$, > 5 ($|\eta| < 1.9$ only) and the fraction of TRT outliers, $N_{\text{TRT}}^{\text{outliers}}/N_{\text{TRT}}$, < 0.9 , where an outlier is a hit which gives a large χ^2 contribution to the fitted track. For tracks with $|\eta| \geq 1.9$ and $N_{\text{TRT}} < 5$ no requirement on the fraction of outliers is made.

The muons are further required to be isolated from other activity in the ID and the calorimeters. Specifically the scalar sum of the transverse momenta of the tracks in a cone of radius $\Delta R = 0.3$ around the muon track must be less than 2.5 GeV and the calorimeter energy measured in a cone of radius $\Delta R = 0.2$ around the muon must be less than 4 GeV. The muons are also required to be well separated from any reconstructed jet fulfilling the criteria listed in Section 7.2.1 by requiring $\Delta R(\text{muon}, \text{jet}) > 0.4$. Finally, muon pairs with opposite sign in d_0 (impact parameter in the transverse plane with respect to the primary vertex), $|d_0| > 0.5$ mm and $\Delta\phi > 3.10$ are identified as cosmic muons and rejected.

7.2.3 $t\bar{t}$ Event Selection

The events are required to have two selected muons with opposite charge fulfilling the criteria listed in Section 7.2.2, at least two jets fulfilling the criteria listed in section 7.2.1 and missing transverse energy greater than 40 GeV. The events with invariant mass of the two muons within 10 GeV of the Z boson mass are identified as Z events and rejected in order to reduce the Z background. Table 7.1 shows the $t\bar{t}$ selection efficiency, the number of expected events estimated for simulated $t\bar{t}$ and Z events and the observed number of events in data. Figure 7.2 shows the jet p_T distribution in data (period E) and simulated events after all selections.

		Simulation		Data
		$t\bar{t}$	Z	
Selection efficiency	E	0.0062 ± 0.0001	0.00010 ± 0.00002	–
	M	0.0061 ± 0.0001	0.00021 ± 0.00003	
Number of selected events	E	23.9 ± 0.5	4.1 ± 0.8	36
	M	494 ± 11	180 ± 26	952

Table 7.1: The selection efficiency as well as the number of observed (data) and expected (simulation) events passing the $t\bar{t}$ event selection criteria. The capital letters E and M refer to the data periods.

7.2.4 Z Event Selection

Z events are selected by requiring two muons with opposite charge which pass the selection criteria listed in section 7.2.2. The events are further required to have an invariant mass of the two muons within 10 GeV of the Z boson mass. No requirement on jets and missing transverse energy are made. Table 7.2 shows the Z selection efficiency, the expected number of events estimated with simulated $t\bar{t}$ and Z events and the observed

number of events in data. Figure 7.3 shows the invariant mass distribution of the muon pair in data (period M) and simulated events after all selections.

		Simulation		Data
		$t\bar{t}$	Z	
Selection efficiency	E	0.00180 ± 0.00008	0.3790 ± 0.0009	—
	M	0.00178 ± 0.00008	0.3768 ± 0.0009	
Number of selected events	E	6.1 ± 0.3	15431 ± 36	17417
	M	144 ± 7	322932 ± 754	355970

Table 7.2: The selection efficiency as well as the number of observed (data) and expected (simulation) events passing the Z event selection criteria. The capital letters E and M refer to the data periods.

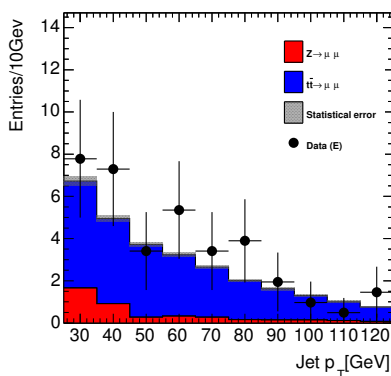


Figure 7.2: The jet p_T distribution for events passing the $t\bar{t}$ selection criteria in data period E. Backgrounds other than Z production have not been estimated.

7.3 Comparison of the Dimuon and Truth-Matching Methods

The ATLAS vertex reconstruction group historically studied split vertices using the truth-matching method described in section 7.1.2. Therefore, the result of the dimuon

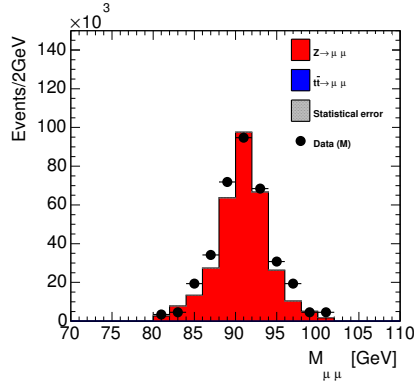


Figure 7.3: The invariant mass of the two selected muons for events passing the Z selection criteria in data period M, together with the expectation from simulated events. Backgrounds from other sources than $t\bar{t}$ production have not been estimated.

method is compared to the truth-matching method in simulated events. For this comparison a split vertex fraction is defined:

$$\text{Split vertex fraction} = \frac{N_{\text{events}}^{\text{split vertex}}}{N_{\text{events}}^{\text{selected}}} \quad (7.2)$$

where $N_{\text{events}}^{\text{selected}}$ is the total number of selected events and $N_{\text{events}}^{\text{split vertex}}$ is the number of selected events containing a split primary vertex.

Figures 7.4(a) and 7.5(a) show the split vertex fractions from the two methods in the selected events from the $t\bar{t}$ and Z simulated samples. The split vertex fraction from the dimuon method is much lower than that obtained with the truth-matching method. This is because the dimuon method is only sensitive to the subset of vertex splits in which the two muons get associated to two different vertices. The split vertex cases in which the two muons are associated to the same vertex cannot be identified by the dimuon method but can be by the truth-matching method.

Figures 7.4(b) and 7.5(b) show the split vertex fraction from the dimuon method together with the fraction of events which are labeled as split vertex events by both the dimuon method and the truth-matching method. In the events which are labeled split by the dimuon method but not the truth-matching method, the contribution from the truth interaction point to one of the two vertices with an associated muon is not large enough for the truth-matching method to label it a split.

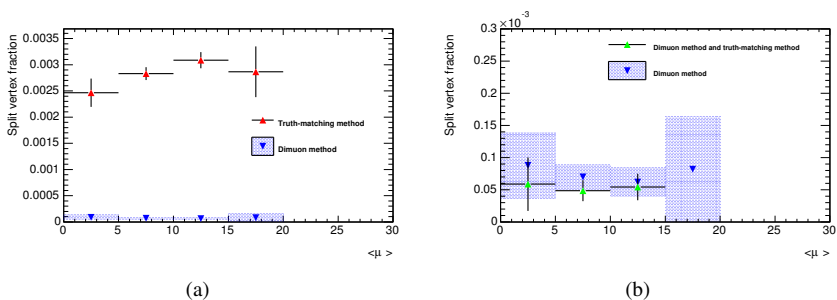


Figure 7.4: The split vertex fraction from the dimuon method and the truth-matching method (a), and the dimuon method and both methods (b) for selected $t\bar{t}$ events. The $\langle \mu \rangle$ is the average number of proton-proton interactions per bunch crossing. Uncertainties are statistical only.

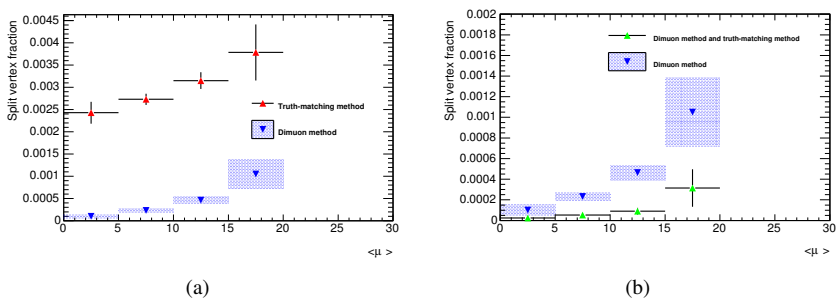


Figure 7.5: The split vertex fraction from the dimuon method and the truth-matching method (a), and the dimuon method and both methods (b) for selected Z events. The $\langle \mu \rangle$ is the average number of proton-proton interactions per bunch crossing. Uncertainties are statistical only.

7.4 Results

In this section the split vertex fraction of the dimuon method observed in data is compared to the fraction expected from simulated events.

7.4.1 $t\bar{t}$ Events

Table 7.3 shows the the results of the dimuon method applied to selected $t\bar{t}$ events. The split vertex fraction in simulated $t\bar{t}$ events is very low, resulting in an expected number of split vertex events much less than the one obtained for both data periods. The contribution from the Z background cannot be estimated since no simulated Z events with split vertices are selected. No events with split vertices are observed in data which is consistent with the expectation from simulated events.

Category		Simulation $t\bar{t}$	Z	Data
Split vertex fraction	E	0.0004 ± 0.0002	–	–
	M	0.00033 ± 0.00009	–	–
$N_{\text{events}}^{\text{split vertex}}$	E	0.008 ± 0.002	–	–
	M	0.17 ± 0.04	–	–

Table 7.3: The result of the dimuon method applied to events passing the $t\bar{t}$ selection criteria.

7.4.2 Z Events

Table 7.4 shows the result of the dimuon method applied to selected Z events. Even though the split vertex fraction in the selected Z events is small (even smaller than the split vertex fraction in $t\bar{t}$ events) several events are observed in data due to the large number of selected Z events.

A clear pileup dependence of the split vertex fraction is observed in both data and simulation as shown in Figure 7.6. The slope of the pileup dependence is consistent between data and simulation.

7.5 Conclusions

The primary vertex performance in data and simulation has been compared using a method based on the vertex association of the two muons from $t\bar{t}$ or Z decays. This so called dimuon method classifies a vertex as split if the two muons are associated to different reconstructed primary vertices. The split vertex fraction in data and simulated events is shown in Figure 7.6. For Z events, the split vertex fraction in data and simulation is compatible for both periods E and M. The data from period M show a slightly higher split vertex fraction than the data from period E, but the difference is not statis-

		Simulation		Data
		$t\bar{t}$	Z	
Split vertex fraction	E	0.0003 ± 0.0002	0.00031 ± 0.00009	0.0004 ± 0.0002
	M	0.0006 ± 0.0002	0.00039 ± 0.00004	0.00088 ± 0.00005
$N_{\text{events}}^{\text{split vertex}}$	E	0.003 ± 0.001	5.6 ± 0.6	7
	M	0.08 ± 0.03	125 ± 13	312

Table 7.4: The result of the dimuon method applied to events passing the Z selection criteria.

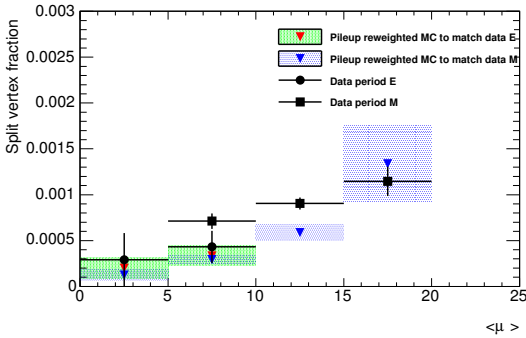


Figure 7.6: The split vertex fraction from the dimuon method in both data and simulated events for events passing the Z selection criteria. Only statistical uncertainties are shown. The $\langle \mu \rangle$ is the average number of proton-proton interactions per bunch crossing.

tically significant. The dependence of the split vertex fraction on the average number of proton-proton interactions per bunch crossing, $\langle\mu\rangle$, is consistent between data and simulation.

In $t\bar{t}$ events, no events with two muons associated to different reconstructed primary vertices are observed in data. This is compatible with the 0.2 expected number of events with split vertices estimated from simulated $t\bar{t}$ events.

Part IV

Search for the Supersymmetric Partner of the Top Quark in Final States with One Isolated Lepton

8 Analysis Strategies and Methods

This chapter describes analysis strategies and methods used in the searches for the supersymmetric partner of the top quark at $\sqrt{s} = 8$ TeV and $\sqrt{s} = 13$ TeV described in this thesis. The search signature of the analyses and dominant the SM backgrounds are described in Section 8.1. The discrimination between the signal events and the SM background events is achieved with various kinematic variables which are described in Section 8.2. By using these variables, signal, control and validation regions can be constructed to select signal events and normalize the SM backgrounds. The applications of the various regions are explained in Section 8.3. The background estimation technique is described in Section 8.4. The statistical methods used to obtain the final results of the analyses are described in Section 8.5.

8.1 Analysis Strategies

The analyses described in this thesis consider all signal scenarios described in Section 2.6. The searches are performed in the single-lepton final state, where the final state particles of a signal event will be one electron or muon, one or two neutrinos originating from the decay of an on- or off-shell W boson, two b quarks (reconstructed as b jets), two light-flavor quarks and two LSPs. The LSPs are not interacting with the detector material and cause large E_T^{miss} together with the neutrino(s). Therefore, the event selection in the analysis requires exactly one isolated electron or muon (defined in Sections 6.4 and 6.5), large E_T^{miss} and at least one b jet.

The dominant backgrounds originate from $t\bar{t}$ and single top Wt production where both W bosons decay leptonically and one of the charged leptons is not identified or is a hadronically decaying τ lepton, as well as $t\bar{t} + Z$ production with $Z \rightarrow \nu\bar{\nu}$, and W +jets production. These dominant backgrounds are normalized in corresponding control regions and extrapolated to the signal regions to estimate the expected number of background events in each signal region. The extrapolation relies on transfer factors (TFs) which are obtained from the simulation. The sub-dominant backgrounds, diboson and Z +jets, are estimated using simulated events.

The results in each signal region are obtained from maximum likelihood ratio fits [145] to the number of observed events in the signal regions as well as the control regions.

8.2 Discriminating Variables

The following kinematic variables are constructed from the reconstructed signal lepton, jets and missing transverse momentum (see Chapter 6). These variables are used to discriminate signal events from the SM background events in the various signal, control, and validation regions.

- $\Delta\phi(\vec{O}_1, \vec{O}_2)$ is the azimuthal opening angle between the directions of the two objects \vec{O}_1 and \vec{O}_2 , where \vec{O}_i is the direction of a jet, lepton or \vec{p}_T^{miss} .
- Transverse mass, m_T , is calculated using the signal lepton (ℓ) and \vec{p}_T^{miss} as [146]

$$m_T = \sqrt{2 \cdot p_T^\ell \cdot E_T^{\text{miss}} (1 - \cos\Delta\phi(\vec{\ell}, \vec{p}_T^{\text{miss}}))}.$$

For most SM processes, this variable has an end-point at the W boson mass, since the E_T^{miss} primarily arises from a single neutrino which originates from a W boson. However, in the BSM physics processes the E_T^{miss} originates from multiple invisible particles, and therefore the m_T value can extend beyond the W mass.

- H_T is the scalar sum of the p_T of the four leading jets. Including only the four leading jets makes this variable robust against extra jets in the events.
- Effective mass, m_{eff} , is the scalar sum of the p_T of all jets with $p_T > 30$ GeV, the p_T of the signal lepton and the E_T^{miss} .
- $E_T^{\text{miss}}/\sqrt{H_T}$ is an approximate measure of the significance of E_T^{miss} ¹⁾. It helps to separate real E_T^{miss} from the mis-measured E_T^{miss} that often arises because of the existence of highly energetic jets.
- $H_{T,\text{sig}}^{\text{miss}}$ is defined as

$$H_{T,\text{sig}}^{\text{miss}} = \frac{|\vec{H}_T^{\text{miss}}| - M}{\sigma_{|\vec{H}_T^{\text{miss}}|}},$$

where \vec{H}_T^{miss} is the negative sum of the p_T vectors of the signal jets and the signal lepton. The $|\vec{H}_T^{\text{miss}}|$ is the mean value of the distribution obtained by replacing the measured jet energies with Gaussian distributions. The central value of each

¹⁾The uncertainty of the energy can be approximated with \sqrt{E} .

Gaussian is set to the measured energy of that jet and the width is set to the ATLAS jet energy resolution. The $\sigma_{|\vec{H}_T^{\text{miss}}|}$ is the root mean square of the \vec{H}_T^{miss} distribution. The M , a characteristic scale of the background, is a tunable parameter and set to 100 GeV [147].

- $m_{\text{had-top}}$ is the hadronic top quark mass reconstructed as the invariant mass m_{j_1, j_2, b_i} with a chi-square minimization method. For a given choice of b -jets, b_i , the χ^2 is defined as:

$$\chi^2 = \frac{(m_{j_1, j_2, b_i} - m_t)^2}{\sigma_{m_{j_1, j_2, b_i}}^2} + \frac{(m_{j_1, j_2} - m_W)^2}{\sigma_{m_{j_1, j_2}}^2},$$

where i takes the value 1 or 2. Here b_1 and b_2 are the b -tagged jets with the highest b -tagging weights while j_1 and j_2 are the two selected jets with highest p_T other than b_1 and b_2 . The $\sigma_{m_{j_1, j_2, b_i}}^2$ and $\sigma_{m_{j_1, j_2}}^2$ are mass resolution terms, which are defined as $\sigma_{m_{j_1, j_2}}^2 = m_{j_1, j_2}^2 (r_{j_1}^2 + r_{j_2}^2)$ and $\sigma_{m_{j_1, j_2, b_i}}^2 = m_{j_1, j_2, b_i}^2 (r_{j_1}^2 + r_{j_2}^2 + r_{b_i}^2)$ respectively, where r_i is the fractionna jet energy uncertainty of jet i . The masses of the top quark and the W boson, m_t and m_W , are set to 170 GeV and 80 GeV, respectively.

- $N^{\text{iso-trk}}$ is the number of isolated tracks which are not associated with any reconstructed leptons or jets. Vetoing events where such tracks exists can help rejecting $t\bar{t}$ events with a τ lepton decaying hadronically to the final state containing a charged pion.
- am_{T2} and m_{T2}^τ are two variants of the m_{T2} variable [148]. The m_{T2} variable is a generalization of the transverse mass in the case where there are two undetected particles. Both am_{T2} and m_{T2}^τ target $t\bar{t}$ events where both W bosons decay to leptons, $t\bar{t} \rightarrow WbWb \rightarrow \ell\nu b\ell'\nu'b$. The am_{T2} variable is designed to reject $t\bar{t}$ events where one lepton is not reconstructed in which case am_{T2} has an end-point at the t mass while in BSM events it can exceed this point. The m_{T2}^τ variable is designed to discriminate against events where one lepton is a hadronically decaying τ lepton giving rise to an additional (undetected) neutrino.
- $topness$ is calculated based on minimizing a χ^2 -type function [149]. The $topness$ variable is also constructed to suppress dileptonic $t\bar{t}$ events in which one lepton is not identified.
- τ veto is constructed based on reconstructed τ candidates passing additional selection criteria. A τ candidate is selected if one or three tracks are associated to it. The selected τ candidate is required to have an opposite charge compared to the signal lepton. Finally, based on the BDT requirement, three working points for the veto, loose, tight, and extra-tight, are defined.

Figure 8.1 shows the comparison between data and MC simulations for the E_T^{miss} , m_T , am_{T2} and $topness$ variables after applying the preselection criteria described in Section 9.2. The comparison shows that the discriminating variables are well modeled in the simulation. The benchmark signal models are also overlaid to indicate the discriminating power of the variable.

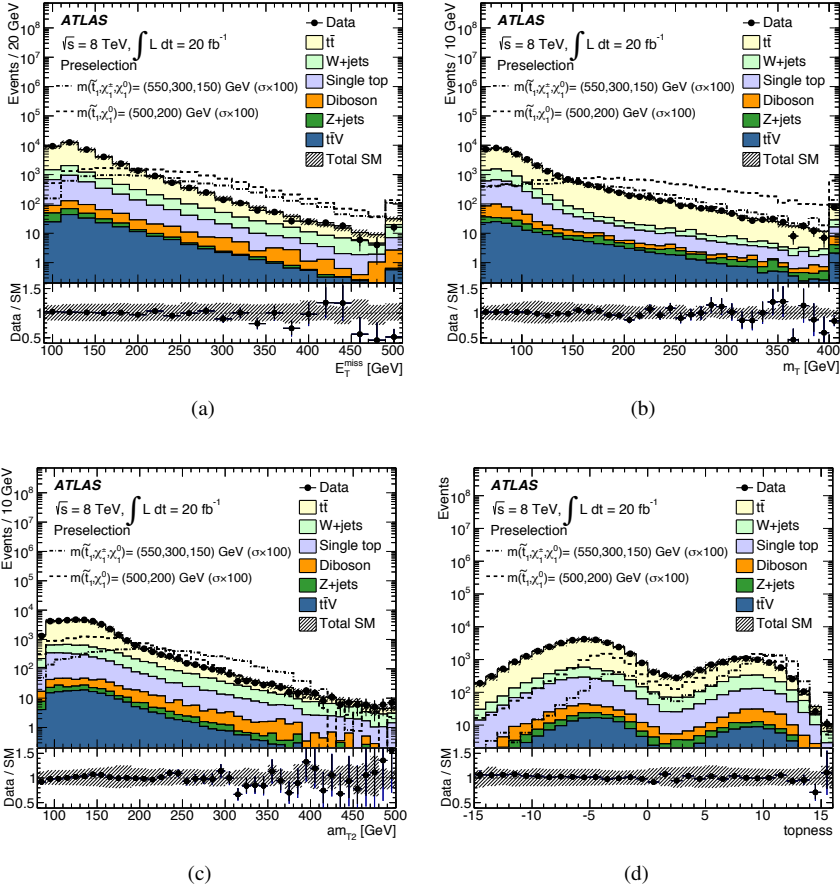


Figure 8.1: Comparison of data with the estimated backgrounds in the variables E_T^{miss} (a), m_T (b), am_{T2} (c) and $topness$ (d) after the preselection is applied [1]. The uncertainty band includes statistical and all experimental systematic uncertainties. The last bin includes overflows. The cross sections of the benchmark signal models overlaid are enhanced by a factor of 100.

8.3 Signal, Control and Validation Regions

Figure 8.2 illustrates the analysis strategy using signal regions (SRs), control regions (CRs) and validation regions (VRs). A signal region is a region of phase space defined by selection criteria on the kinematic variables which are optimized for a particular signal model. The signal region optimization is based on simulation and uses the expected number of signal and background events in the SR to construct a figure of merit to be maximized. The signal region is either constructed as a single-binned or multi-binned region. A single-binned signal region (SR1 and SR3 in Figure 8.2) corresponds to a simple cut-and-count analysis in which the number of events in the signal region is counted. A multi-binned signal region (SR2 in Figure 8.2) corresponds to a shape fit analysis where the signal region is split into several bins, and the number of events is counted in each bin separately. All bins are fitted simultaneously in the likelihood fit, as described in Section 8.5. The CRs and VRs can also be either single-binned or multi-binned regions.

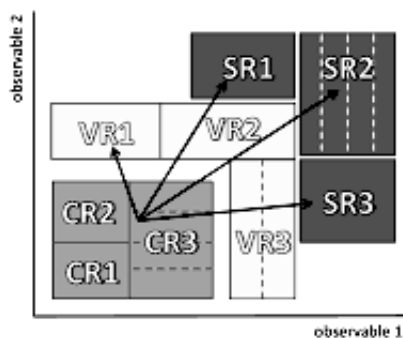


Figure 8.2: Illustration of an analysis strategy using single- and multi-binned signal regions (SR1-3), control regions (CR1-3) and validation regions (VR1-3) [150].

A CR is defined by a set of selection criteria similar to those defining the signal region but with some criteria altered to retain a sufficiently large number of background events and reject most events from the signal and other background processes. A VR is defined between a signal region and its corresponding control region. The VR is used to validate the prediction obtained from the CR. A SR and the corresponding CRs and VRs are defined to be orthogonal to each other. But the various SRs can be overlapping.

8.4 Background Estimation Techniques

The expected number of events from each dominant SM background process is normalized to data in a corresponding CR. The normalization is obtained using a normalization factor F^{norm} , which in the case of a CR that is 100% pure in a given SM background process, is defined as

$$N_{\text{data}}^{\text{CR}} = N_{\text{MC}}^{\text{CR}} \times F^{\text{norm}} \quad (8.1)$$

where $N_{\text{data}}^{\text{CR}}$ is the observed number of data events in the CR and $N_{\text{MC}}^{\text{CR}}$ is the expected number of SM background events in simulation. In practice, all CRs contain a mix of SM backgrounds, where multiple normalization factors are needed:

$$N_{\text{data}}^{\text{CR}} = \sum_i N_{\text{MC},i}^{\text{CR}} \times F_i^{\text{norm}} \quad (8.2)$$

Since one CR is defined for each major background, all normalization factors TF_i^{norm} , can be determined in a common fit to all CRs (see Section 8.5). The estimated numbers of background events in the SR, VRs and other CRs are obtained from an extrapolation between the CR and SR, VRs or other CRs. As an example, the extrapolation between a CR and the SR is defined as:

$$N_{\text{est},i}^{\text{SR}} = N_{\text{MC},i}^{\text{CR}} \times F_i^{\text{norm}} \times TF_i \quad (8.3)$$

where $N_{\text{est},i}^{\text{SR}}$ is the estimated number of events from background i in the signal region and TF_i is the transfer factor. The transfer factor is obtained using simulated background events, and is defined as:

$$TF_i = \frac{N_{\text{MC},i}^{\text{SR}}}{N_{\text{MC},i}^{\text{CR}}} \quad (8.4)$$

where $N_{\text{MC},i}^{\text{SR}}$ is the expected number of MC simulated events from background i in the signal region.

The estimations of the sub-dominant backgrounds rely on the simulation, and they are normalized to their theoretical cross sections. The multijet background is estimated from data using the matrix method [151], and its contribution is found to be negligible.

8.5 Statistical Methods

In particle physics experiments a large number of data samples need to be carefully analyzed. In general, the analyses rely on the predicted number of signal and background events in the data. As discussed in the previous section, the expected numbers of background events may be constructed entirely from simulated events or data-driven methods, for example using dedicated control regions. In the case of a search for physics beyond the SM, the expected number of signal events are always obtained from simulations. The simulation of the signal process may depend on several parameters like the masses of the BSM particles. In the case that no excess over the expected SM background is observed in the data, exclusion limits can be set on these parameters. In addition, model-independent upper limits on the number of non-SM events can also be provided.

The search results are obtained by maximizing a likelihood function. The inputs to the likelihood fit are the number of expected and observed events in the various SRs and CRs. The fit is performed using the HistFitter software framework [150]. It is a flexible and programmable framework and contains tools to perform the fits, as well as interpret and present results. In the HistFitter package, a Probability Density Function (PDF) is constructed from the parameters of interest, such as the rate of a signal process, the normalization factors for background processes and so-called nuisance parameters that parameterize the impact of systematic uncertainties. The figure of merit for excluding a part of the parameter space in a BMS search is based on the so-called CL_s method [152] which is also implemented in by HistFitter.

There are three common fit strategies, "background-only fit", "model-dependent fit" and "model-independent fit" which are different in terms of which combination of SRs and CRs they are using.

Parametrized Likelihood

The general parametrized likelihood L implemented in HistFitter is the product of the Poisson distributions of event counts in the SR and the CRs multiplied by constraint terms from systematic uncertainties C_{syst} . It can be written as:

$$\begin{aligned}
 L(\mathbf{n}, \theta^0 | \mu_{\text{sig}}, \mathbf{b}, \theta) &= P_{\text{SR}} \times P_{\text{CR}} \times C_{\text{syst}} \\
 &= P(n_S | \lambda_S(\mu_{\text{sig}}, \mathbf{b}, \theta)) \times \\
 &\quad \prod_{i \in \text{CR}} P(n_i | \lambda_i(\mu_{\text{sig}}, \mathbf{b}, \theta)) \times C_{\text{syst}}(\theta^0, \theta)
 \end{aligned} \tag{8.5}$$

The Poisson measurements n_S and n_i are the numbers of observed events in the signal region and each control region i . The Poisson expectations λ_S and λ_i in the signal region and each control region respectively, are functions of the signal strength parameter μ_{sig} and the background predictions \mathbf{b} . The signal strength parameter is defined such that

$\mu_{\text{sig}} = 0$ turns off the signal component completely while $\mu_{\text{sig}} = 1$ sets the signal expectation equal to the nominal value. Systematic uncertainties are included using C_{syst} , where θ are the nuisance parameters, and θ^0 are the central values of θ . Typically C_{syst} is parameterized as the product of a Gaussian distribution G with unit width:

$$C_{\text{syst}}(\theta^0, \theta) = \prod_{j \in S} G(\theta_j^0 - \theta_j) \quad (8.6)$$

where S is the full set of systematic uncertainties that are under consideration. Each nuisance parameter θ_j describes a systematic uncertainty and is defined such that $\theta_j = 0$ corresponds to the nominal case and $\theta_j = \pm 1$ to a $\pm 1\sigma$ variation of the size of the systematic uncertainty.

Background-Only Fit

This fit configuration is used to estimate the total number of background events in the SR and VRs, that can be used by external groups to perform hypothesis tests. It uses background estimates only and does not make any assumptions on the signal model, which means that $\mu_{\text{sig}} = 0$. The fit is performed only with inputs from the CRs.

Model-Dependent Fit

The model-dependent fit takes a specific signal model into account and fits the CRs and the SR simultaneously. In the case of no significant excess, the fit result can be used to set upper limits on the parameters of this signal model. The possible signal contaminations in the CRs are taken into account by including the predicted signal in each CR. In this fit configuration, μ_{sig} is a free parameter.

This configuration can run on several SRs and CRs as long as they are statistically independent. The combination of several SRs can increase the sensitivity of the analysis on signal models.

Model-Independent Fit

This fit configuration is used to set an upper limit on the expected number of BSM events predicted in an SR. Just as for the model-dependent fit it uses both the SR and the CRs, but here the assumption is made that there is no signal contamination in the CRs; it sets the signal predictions in all SRs to zero. Since the fit is model independent, the results from it can be used to test any signal model by comparing the predicted number of events from this model to the upper limit from the model-independent fit.

One restriction is that the fit can only be applied to a single bin SR since the distribution of signal events over several bins requires assumptions on the signal model. For multi-bin SRs used in the shape fit analyses, the fit is generally performed with only the SR bin with the largest expected signal contribution.

CL_s Calculation

The decision of excluding a model is based on the CL_s value, which is the probability of the observation being compatible with the signal+background hypothesis.

It is defined as a normalization of the confidence level observed for the signal + background hypothesis, CL_{s+b}, to the confidence level observed for the background-only hypothesis, CL_b:

$$\text{CL}_s = \frac{\text{CL}_{s+b}}{\text{CL}_b} = \frac{P(N_{s+b} \leq N_{\text{obs}})}{P(N_b \leq N_{\text{obs}})} \quad (8.7)$$

where $P(N_{s+b} \leq N_{\text{obs}})$ is the probability of the parameter N_{s+b} being less than the observation N_{obs} under the signal+background hypothesis, and $P(N_b \leq N_{\text{obs}})$ is the probability of the parameter N_b being less than the observation N_{obs} . The CL_s method is conservative as it mitigates the problem of excluding models in cases where a downward fluctuation of the number of background events has occurred, something that is a concern in analyses which have low sensitivity.

In the LHC experiments, the expected and observed CL_s values are calculated from the expected and observed number of events in the SR, respectively. A model is excluded with 95% confidence level if the observed CL_s value is less than 0.05 (5%). The exclusion results are presented in terms of so-called exclusion contours in the signal model parameter space (for a stop search it is usually presented in the $\tilde{t}_1 - \tilde{\chi}_1^0$ mass plane). In general, there is more than one SR sensitive to a given signal model. In this case, the result from the signal region with the best expected CL_s value is used, since the SRs are generally not orthogonal.

9 Search for Direct Stop Pair Production with Run 1 Data

A light \tilde{t}_1 is motivated by the naturalness principle since a \tilde{t}_1 mass below 1 TeV can provide an attractive solution to the hierarchy problem by canceling the radiative corrections to the Higgs mass from the top quark (see Chapter 2). In this chapter, a search for direct \tilde{t}_1 pair production in the single lepton final state using 20.3 fb^{-1} of data at the center of mass energy $\sqrt{s} = 8 \text{ TeV}$ is presented [1]¹⁾. The signal models and analysis strategies for this analysis are described in Section 9.1. The analysis uses optimized signal regions to discriminate signal events from SM processes. The signal region constructions are described in section 9.2. Each signal region has corresponding control and validation regions which are described in Section 9.3. The sources of systematic uncertainties are described in Section 9.4. Finally, the results and conclusion of this analysis are presented in Sections 9.5 and 9.6.

9.1 Signal Models and Analysis Strategies

This analysis targets direct stop pair production in the $\tilde{t}_1 \rightarrow t\tilde{\chi}_1^0$, $\tilde{t}_1 \rightarrow bW\tilde{\chi}_1^0$, $\tilde{t}_1 \rightarrow b\tilde{\chi}_1^\pm$ and mixed decay scenarios described in Section 2.6. Both cut-and-count and shape fit analyses are included to increase sensitivity of the analysis in various signal scenarios. For each signal scenario, one or more signal regions are constructed to cover a wide range of \tilde{t}_1 - $\tilde{\chi}_1^0$ masses.

The SM background estimation is based on the techniques described in section 8.4. The dominant SM background in this analysis comes from $t\bar{t}$ events, followed by the production of a W boson in association with jets (W +jets). Therefore, corresponding top and W +jets control regions are constructed to estimate these backgrounds. Smaller backgrounds, single top, diboson, $t\bar{t} + V$ and Z +jets, are estimated using simulated

¹⁾The analysis in this reference also includes a search in the soft-lepton final state, but it is not included in this thesis.

events.

The results in each signal region are obtained using the CL_s prescription described in Section 8.5. Furthermore, the systematic uncertainties described in Section 9.4 are included in the fit as nuisance parameters. The final results are presented in terms of model-dependent exclusion limits and model-independent upper limits.

9.2 Event Selection

9.2.1 Preselection Criteria

A set of preselection criteria, shown in Table 9.1, are applied to the events before selecting signal-like events. Event candidates in the data are collected using a combination of single-lepton and a E_T^{miss} triggers.

- **Single-electron trigger:** Electrons are identified based on the energy deposits in the electromagnetic calorimeter. The transverse energy (E_T) threshold of the trigger is 24 GeV. Furthermore, it requires the shower shape in the electromagnetic calorimeter to be consistent with an electron, low hadronic leakage and the presence of an ID track matched to the calorimeter cluster.
- **Single-muon trigger:** Muons are identified using tracks reconstructed in the ID and MS. The p_T threshold of the trigger is 24 GeV.
- **Additionally, the single lepton triggers include an isolation requirement.** The isolation requires the sum of the transverse momenta (p_T) of the track within a cone of $\Delta R = 0.2$ to be less than 10% of the electron E_T for the electron trigger and less than 12% of the muon p_T for the muon trigger.
- **E_T^{miss} trigger:** The E_T^{miss} trigger requires $E_T^{\text{miss}} > 80$ GeV, which is calculated as the vector sum of the transverse energy deposits in the projective calorimeter trigger towers. This trigger is fully efficient for events with one signal lepton and offline-calibrated $E_T^{\text{miss}} > 150$ GeV.

In order to recover some efficiency loss for high p_T leptons, the data are also collected with complementary single-lepton triggers which do not require isolation but have a higher threshold, $E_T > 60$ GeV for the electron trigger and $p_T > 36$ GeV for the muon trigger.

The event candidates should have at least one primary vertex. Furthermore, an event is rejected if it contains a muon candidate which is identified as a cosmic muon. In addition, the event is rejected if some jets are badly reconstructed, the E_T^{miss} is mismeasured, or if there are detector-related problems. The events are finally required to contain exactly one electron or muon with $p_T > 25$ GeV and $|\eta| < 2.5$ (2.47 for electrons), at least three or more jets with $p_T > 25$ GeV and $E_T^{\text{miss}} > 100$ GeV.

The events which fulfill the preselection criteria are further considered for the various signal regions. The signal regions are constructed using the kinematic variables described in section 8.2.

Preselection	Description
Trigger	Single-lepton triggers or E_T^{miss} triggers
Data quality	Jet and E_T^{miss} cleaning, cosmic muon veto, at least one primary vertex
Lepton	Exactly one electron or muon with $p_T > 25$ GeV
2nd lepton veto	Veto events containing additional baseline leptons with $p_T > 10$ GeV
Jets	At least 3 or 4 jets (different for different signal regions)
E_T^{miss}	Offline missing transverse energy $E_T^{\text{miss}} > 100$ GeV

Table 9.1: Preselection criteria common to all signal selections.

9.2.2 Signal Regions

The kinematic properties of the \tilde{t}_1 change quite substantially from one decay mode to another and are also different for different masses of the \tilde{t}_1 , $\tilde{\chi}_1^\pm$ and $\tilde{\chi}_1^0$. Therefore, several signal regions are defined to cover various decay modes and a wide range of masses.

$\tilde{t}_1 \rightarrow t\tilde{\chi}_1^0$ signal regions

The signal regions targeting the $\tilde{t}_1 \rightarrow t\tilde{\chi}_1^0$ decay mode are summarized in Tables 9.2 and 9.3. Different signal regions are designed to cover different regions of stop and LSP masses. For low stop masses where the \tilde{t}_1 and $\tilde{\chi}_1^0$ have a mass splitting below the t quark mass, the \tilde{t}_1 undergoes a three body decay via an off-shell t quark. The decay products have lower momenta, but are still above the reconstruction threshold, and the events have low am_{T2} values since $m_{\tilde{t}_1} - m_{\tilde{\chi}_1^0} < m_t$. This scenario is covered by a binned shape fit signal region, 3body, in m_T and am_{T2} . This signal region is optimized for \tilde{t}_1 masses below 300 GeV. In the diagonal region, $m_{\tilde{t}_1} \gtrsim m_{\tilde{\chi}_1^0} + m_t$, the stop and LSP are nearly mass degenerate which results in lower E_T^{miss} . A two-dimensional shape fit signal region, tN_diag in m_T and E_T^{miss} is optimized specifically for this scenario, resulting in improved sensitivity. The binning, together with the number of observed events and the expected number of SM events, for the 3body and tN_diag signal regions are shown in Figure 9.1. In all shape fit signal regions, the upper bins are sensitive to a potential signal but are also used to normalize the $t\bar{t}$ background, while the lower bins are used to

normalize the W +jets background.

At the intermediate stop masses, $250 \text{ GeV} \lesssim m_{\tilde{t}_1} \lesssim 550 \text{ GeV}$, the stop decay products have reasonably large p_T which also yields larger E_T^{miss} . There, a cut-and-count signal region, tN_med is optimized. Analogously the higher stop mass regions ($m_{\tilde{t}_1} \gtrsim 550 \text{ GeV}$) are covered by tN_high . This signal region is also a cut-and-count signal region but with tighter selection criteria, since the decay products of the stop have even larger p_T . In addition to tN_high , a signal region targeting the scenario where the t quark is very boosted is also considered in the high stop mass and very low LSP mass region. Since the t quark from the \tilde{t}_1 has large p_T , its decay products will be very collimated and thus efficiently captured by a large- R jet. Therefore, this tN_boost signal region is optimized based on these large- R jets.

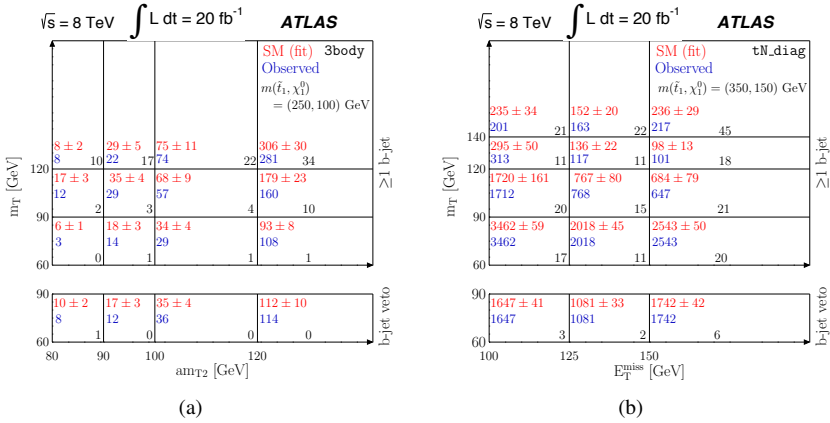


Figure 9.1: The binning of the 3body (a) and tN_diag (b) shape fit signal regions together with the number of observed events and the expected number of SM and signal events. The upper bins provide stop signal sensitivity and are also used to normalize the $t\bar{t}$ background. The bottom bins veto events with b -jets, and are used to normalize the W +jets background [1].

$\tilde{t}_1 \rightarrow b\tilde{\chi}_1^\pm$ Signal Regions

Tables 9.4 and 9.5 show the five signal regions that are constructed to cover the $\tilde{t}_1 \rightarrow b\tilde{\chi}_1^\pm$ scenarios. The kinematics of the $\tilde{t}_1 \rightarrow b\tilde{\chi}_1^\pm$ signal models are mostly defined by the mass of the $\tilde{\chi}_1^\pm$ relative to $m_{\tilde{t}_1}$ and $m_{\tilde{\chi}_1^0}$ as illustrated in Figure 9.2. In scenarios where the mass splitting between the $\tilde{\chi}_1^\pm$ and the $\tilde{\chi}_1^0$ is large but the $\tilde{\chi}_1^\pm$ and \tilde{t}_1 are mass

	tN_diag	tN_med	tN_high	tN_boost
Preselection	Default preselection criteria, c.f. Table 9.1			
Jets [GeV]	≥ 4 with $p_T > (60, 60, 40, 25)$	≥ 4 with $p_T > (80, 60, 40, 25)$	≥ 4 with $p_T > (100, 80, 40, 25)$	≥ 4 with $p_T > (75, 65, 40, 25)$
b -tagging	≥ 1 b -tag (70% eff.) amongst four selected jets			
large- R jet	–			≥ 1 , $p_T > 270$ GeV and $m > 75$ GeV
$\Delta\phi(\text{jet}_2^{\text{large-}R}, \vec{p}_T^{\text{miss}})$	–			0.85
E_T^{miss} [GeV]	$> 100^{(*)}$	> 200	> 320	> 315
m_T [GeV]	$> 60^{(*)}$	> 140	> 200	> 175
am_{T2} [GeV]	–	> 170	> 170	> 145
m_{T2}^τ [GeV]	–	–	> 120	–
$topness$	–	–	–	> 7
$m_{\text{had-top}}$ [GeV]	$\in [130, 205]$	$\in [130, 195]$	$\in [130, 250]$	
τ -veto	tight τ id	–	–	extra-tight τ id, $\Delta R(\tau_{\text{had}}, \text{large-}R\text{-jet}) > 2.6$
$\Delta R(b\text{-jet}, \ell)$	< 2.5	–	< 3	< 2.6
$E_T^{\text{miss}}/\sqrt{H_T}$ [GeV $^{1/2}$]	> 5	–		
$H_{T,\text{sig}}^{\text{miss}}$	–	> 12.5		> 10
$\Delta\phi(\text{jet}_i, \vec{p}_T^{\text{miss}})$	> 0.8 ($i = 1, 2$)	> 0.8 ($i = 2$)	–	$> 0.5, 0.3$ ($i = 1, 2$)

(\ast): The tN_diag is a two-dimensional, multi-bin shape fit based on E_T^{miss} and m_T .

Table 9.2: Selection criteria for signal regions which target $\tilde{t}_1 \rightarrow t\tilde{\chi}_1^0$ decays [1].

degenerate, $m_{\tilde{t}_1} - m_{\tilde{\chi}_1^\pm} \lesssim m_b$, the b quark from the \tilde{t}_1 decay has very low p_T and can not be reconstructed. In this diagonal region, a bCc_diag signal region is optimized in which the events containing reconstructed b jets are rejected.

The low and intermediate stop mass regions ($m_{\tilde{t}_1} \lesssim 500$ GeV) are targeted by two

	tNbC_mix	3body
Preselection	Default preselection criteria, c.f. Table 9.1	
Jets [GeV]	≥ 4 jets with $p_T > (80, 70, 50, 25)$	≥ 4 jets with $p_T > (80, 25, 25, 25)$
b -tagging [GeV]	≥ 1 b -tag (70% eff.) with $p_T > 60$	≥ 1 b -tag (70% eff.) with $p_T > 25$
E_T^{miss} [GeV]	> 270	> 150
m_T [GeV]	> 130	$> 60^{(*)}$
am_{T2} [GeV]	> 190	$> 80^{(*)}$
topness	> 2	—
m_{jjj} [GeV]	< 360	—
$E_T^{\text{miss}}/\sqrt{H_T}$ [GeV $^{1/2}$]	> 9	> 5
τ -veto	tight τ id	
$\Delta\phi(\text{jet}_i, \vec{p}_T^{\text{miss}})$	> 0.6 ($i = 1, 2$)	> 0.2 ($i = 1, 2$)
$\Delta\phi(\ell, \vec{p}_T^{\text{miss}})$	> 0.6	> 1.2
$\Delta R(\ell, \text{jet}_i)$	< 2.75 ($i = 1$)	> 1.2 ($i = 1$), > 2.0 ($i = 2$)
$\Delta R(\ell, b\text{-jet})$	< 3.0	—

(\ast): The 3body is a two-dimensional, multi-bin shape fit based on m_T and am_{T2} .

Table 9.3: Selection criteria for the two SRs which target the mixed $\tilde{t}_1 \rightarrow t\tilde{\chi}_1^0$ and $\tilde{t}_1 \rightarrow b\tilde{\chi}_1^\pm$ decay scenario (left), and the three-body decay, 3body (right) [1].

two-dimensional shape fit signal regions bCd_bulk and bCb_med2 illustrated in Figure 9.3. The bCd_bulk signal region is optimized for a larger mass splitting between the $\tilde{\chi}_1^\pm$ and the $\tilde{\chi}_1^0$ while the bCb_med2 signal region targets the models with a small mass splitting between the $\tilde{\chi}_1^\pm$ and the $\tilde{\chi}_1^0$ ($m_{\tilde{\chi}_1^\pm} - m_{\tilde{\chi}_1^0} \lesssim m_W$) resulting in a decay chain involving a virtual W boson.

In the high stop mass region, $m_{\tilde{t}_1} \gtrsim 500$ GeV, two cut-and-count signal regions bCd_high1 and bCd_high2 are optimized to target $\tilde{t}_1 \rightarrow b\tilde{\chi}_1^\pm$ scenarios with large mass splitting between the \tilde{t}_1 , $\tilde{\chi}_1^\pm$ and $\tilde{\chi}_1^0$.

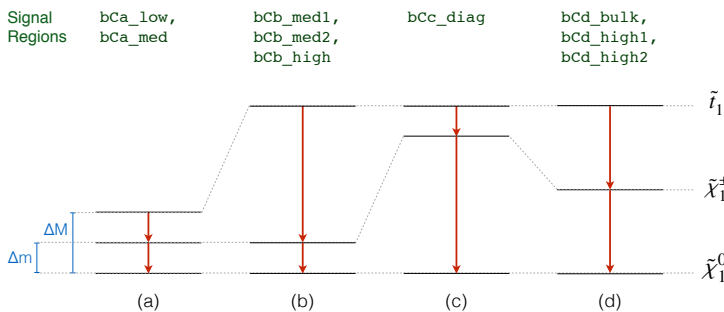


Figure 9.2: Illustration of the mass hierarchies for $\tilde{t}_1 \rightarrow b\tilde{\chi}_1^\pm$ decays with $\tilde{\chi}_1^\pm \rightarrow W^{(*)}\tilde{\chi}_1^0$, and corresponding signal regions [1]. Only the mass hierarchies (b), (c) and (d) and their corresponding signal regions are considered in this thesis.

	bCb_med2	bCd_bulk
Preselection	Default preselection criteria, c.f. Table 9.1	
Jets [GeV]	≥ 4 with $p_T > (80, 60, 40, 25)$	
b -tagging [GeV]	≥ 2 (80% eff.) with $p_T > (140, 75)$	≥ 1 (70% eff.) with $p_T > (25, 25)$
E_T^{miss} [GeV]	> 170	> 150
m_T [GeV]	$> 60^{(*)}$	
$E_T^{\text{miss}}/\sqrt{H_T}$ [GeV $^{1/2}$]	> 6	> 7
am_{T2} [GeV]	$> 80^{(*)}$	
Track, τ -veto	track & τ -veto (tight τ id)	
$\Delta\phi(\text{jet}_i, \vec{p}_T^{\text{miss}})$	> 0.8 ($i = 1, 2$)	

($^{(*)}$): Two-dimensional multi-bin shape fit signal region based on m_T and am_{T2} .

Table 9.4: Selection criteria for signal regions which target $\tilde{t}_1 \rightarrow b\tilde{\chi}_1^\pm$ decays [1].

tNbC_mix signal region

The tNbC_mix signal region in Table 9.3 is a cut-and-count signal region which is optimized to be sensitive to the mixed scenario. The signal region is optimized on a signal

	bCd_high1	bCd_high2	bCc_diag
Preselection	Default preselection criteria, c.f. Table 9.1		
Lepton	= 1 lepton with $p_T > 25$ GeV		= 1 lepton with $p_T > 25$ GeV and $ \eta < 1.2$
Jets [GeV]	≥ 4 with $p_T > (80, 60, 40, 25)$	≥ 4 with $p_T > (80, 80, 40, 25)$	≥ 3 with $p_T > (80, 40, 30)$
b -tagging / veto [GeV]	≥ 2 (80% eff.) with $p_T > (75, 75)$	≥ 2 (80% eff.) with $p_T > (170, 80)$	= 0 (70% eff.) with $p_T > 25$
E_T^{miss} [GeV]	> 150	> 160	> 140
m_T [GeV]	> 120		
$E_T^{\text{miss}}/\sqrt{H_T}$ [GeV $^{1/2}$]	> 9	> 8	> 5
am_{T2} [GeV]	> 200	> 250	–
Track, τ -veto	track & τ -veto (tight τ id)		–
$\Delta R(j_1, \ell)$	–		$\in [0.8, 2.4]$
$\Delta\phi(\text{jet}_i, \vec{p}_T^{\text{miss}})$	> 0.8 ($i = 1, 2$)		> 2.0 ($i = 1$), > 0.8 ($i = 2$)

Table 9.5: Selection criteria for signal regions which target $\tilde{t}_1 \rightarrow b\tilde{\chi}_1^\pm$ decays [1].

sample with a 50% branching ratio of the $\tilde{t}_1 \rightarrow t\tilde{\chi}_1^0$ decay.

9.3 Control and Validation Regions

In this analysis two sets of control/validation regions are constructed for each cut-and-count signal region, one for the $t\bar{t}$ background and one for the W +jets background (see Table 9.6).

- The top control regions (TCRs) are designed to be as close as possible to the SRs but deploy a $60 \text{ GeV} < m_T < 90 \text{ GeV}$ requirement in order to select semi-leptonic $t\bar{t}$ events. The top validation regions (TVRs) are defined in the $90 \text{ GeV} < m_T < 120 \text{ GeV}$ window.
- The W +jets control regions (WCRs) also require $60 \text{ GeV} < m_T < 90 \text{ GeV}$, but additionally require zero b jets, which reduces the $t\bar{t}$ contribution and makes the WCRs orthogonal to the TCRs. The W +jets validation regions (WVRs) are defined with a $90 \text{ GeV} < m_T < 120 \text{ GeV}$ and a zero b jets requirement.

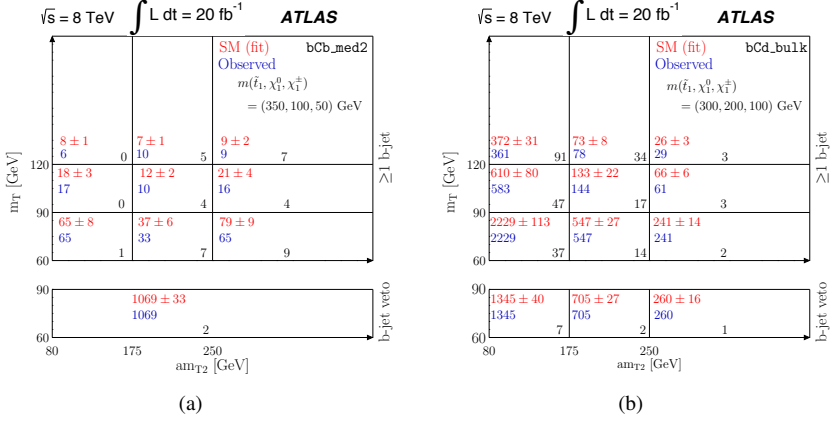


Figure 9.3: The binning of the bCb_med2 (a) and bCd_bulk (b) shape fit signal regions together with the number of observed events and the expected number of SM and signal events. The upper bins provide stop signal sensitivity and are also used to normalize the $t\bar{t}$ background. The bottom bins veto events with b jets, and are used to normalize the W +jets background [1].

The two-dimensional shape fit signal regions have multiple bins that are dominated by $t\bar{t}$ events. These bins can serve as TCRs and be used in the $t\bar{t}$ background normalization. In addition, a three-bin WCR with a b -tag veto and $60 \text{ GeV} < m_T < 90 \text{ GeV}$ is constructed for each shape fit signal region to normalize the W +jets background (see Figures 9.1 and 9.3).

9.4 Systematic Uncertainties

Two types of uncertainties, experimental and theoretical, are evaluated for all background and signal samples, using MC simulations.

The dominant experimental uncertainties arise from the calibration of the jet energy scale (JES), the measurement of the jet energy resolution (JER), and from the modeling of the b -tagging efficiency. The impact of the JES [153, 154] on the background samples is estimated to range from 1% to 13%, and the impact of the JER [155] ranges from 1% to 21%. The total uncertainty from the JER, and the jet mass scale and resolution on the large- R jets is 3% which is obtained from both data and MC simulations [134, 156]. The uncertainty from the b -tagging efficiency is estimated by varying the efficiency correction factors for b and c jets and the mis-tag rate correction factors which are measured in $t\bar{t}$ and dijet events [157–160]. Its impact on the backgrounds ranges from

Signal regions	Variables	Control regions		Validation regions	
		TCR	WCR	TVR	WVR
All tN_*	m_T [GeV]	[60,90]		[90,120]	
	N_b	≥ 1	$= 0$	≥ 1	$= 0$
tN_boost	am_{T2} [GeV]	> 130			
	E_T^{miss} [GeV]	> 260			
	topness	-			
All bCc_*, bCd_*	m_T [GeV]	[60,90]		[90,120]	
bCc_diag	N_b	≥ 1	$= 0$	≥ 1	$= 0$
All bCd_*	N_b	≥ 2	$= 0$	≥ 2	$= 0$
bCd_high1	am_{T2} [GeV]	> 120	> 200	> 120	> 200
bCd_high2	am_{T2} [GeV]	> 120	> 250	> 120	> 250
tNbC_mix	m_T [GeV]	[60,90]		[90,120]	
	N_b	≥ 1	$= 0$	≥ 1	$= 0$
	am_{T2} [GeV]	> 120			
	E_T^{miss} [GeV]	> 170			
	$E_T^{\text{miss}}/\sqrt{H_T}$ [GeV $^{1/2}$]	> 5			

Table 9.6: Event selections for control and validation regions. The asterisk symbol ‘*’ indicates the variables common to several regions.

1% to 8%. The other experimental uncertainties originate from the modeling of the average number of interactions per bunch crossing, the modeling of the contribution to the E_T^{miss} from energy deposits which are not associated to reconstructed objects or arise from pileup effects, the modeling of the trigger, identification efficiency, energy and momentum scale and resolution, isolation and τ -veto, and the uncertainty on the integrated luminosity. The total impact of these sources of uncertainties in the SRs varies from 1% to 5%.

Since the dominant backgrounds, $t\bar{t}$ and W +jets, are normalized in the corresponding CRs, the MC modeling uncertainties only affect the extrapolation from the CRs to the SRs. For both of these background processes, the uncertainties from a variation of the renormalization and factorization scales by factors of 0.5 and 2.0 and from PDF variations [125, 161] are considered. For the $t\bar{t}$ process the uncertainties from the mod-

eling of hadronization, initial state radiation (ISR) and final state radiation (FSR) are derived. For the W +jets process the effect of varying the number of extra partons and the jet flavor composition of the W +jets events [162] in the SRs are taken into account. The overall MC modeling uncertainty varies from 2% to 6% for $t\bar{t}$ events and 1% to 7% for W +jets events. The backgrounds other than $t\bar{t}$ and W +jets are normalized to the theory cross section. The uncertainty on the theory cross section is 7% [163–165] for the single t process, 22% [166, 167] for the $t\bar{t} + V$ process, and 7% and 5% for the WZ and ZZ processes respectively [113, 168]. The other sources of uncertainties considered for these backgrounds are the choice of renormalization and factorization scale, PDF variations, modeling of hadronization, choice of MC generator, ISR and FSR modeling, variation of matching scales, the number of partons and the modeling of the interference between $t\bar{t}$ and single t at NLO. The total uncertainty from these sources is estimated to be 1% to 11% on the transfer factors.

The theory uncertainties on the expected number of signal events mainly originate from the uncertainty on the theory cross section [169] which varies as a function of the \tilde{t}_1 mass. The uncertainty is 15% for a stop mass of 200 GeV and increases up to 18% for a stop mass of 700 GeV. The ISR and FSR uncertainty on the signal acceptance only affects the bCc_diag signal region since it relies on ISR jets, and it is 10% to 20%. For the other signal regions, it is found to be negligible.

9.5 Results

Figures 9.4 and 9.5 show the observed data and the expectation from SM processes from the background-only fit in four different signal regions. In each plot, all signal region selection criteria except the one shown in the plot are applied.

The results show that there is no significant excess in data over the SM model predictions in any of the signal regions. Consequently, model-independent upper limits on non-SM processes are derived for each cut-and-count signal region and for each bin in the shape fit signal regions. Table 9.7 shows the observed number of events, the SM expectations and the upper limits on non-SM processes ($N_{\text{non-SM}}$) for each signal region.

In addition to the model-independent results, the search results are also interpreted in terms of the signal models described in Section 9.1. Figure 9.6(a) shows the excluded mass parameter space in the $\tilde{t}_1 \rightarrow t\tilde{\chi}_1^0$ and $\tilde{t}_1 \rightarrow bW\tilde{\chi}_1^0$ decay scenarios. The four-body decay mode $\tilde{t}_1 \rightarrow bff'\tilde{\chi}_1^0$ in the region $m_{\tilde{t}_1} \lesssim m_b + m_W + m_{\tilde{\chi}_1^0}$ is targeted by a soft-lepton ($p_T < 25$ GeV) analysis and is not described in this thesis. The Figures 9.6(b) and 9.7 show the exclusion contours in the $\tilde{t}_1 \rightarrow b\tilde{\chi}_1^\pm$ decay scenario. The expected and observed exclusion contours are overlaid, and the yellow $\pm 1\sigma_{\text{exp}}$ band indicates the impact of all uncertainties included in the fit while the $\pm 1\sigma_{\text{theory}}^{\text{SUSY}}$ line show the variation of the observed limit as the nominal signal cross section is scaled up and down by the 1σ uncertainty on the theoretical cross section.

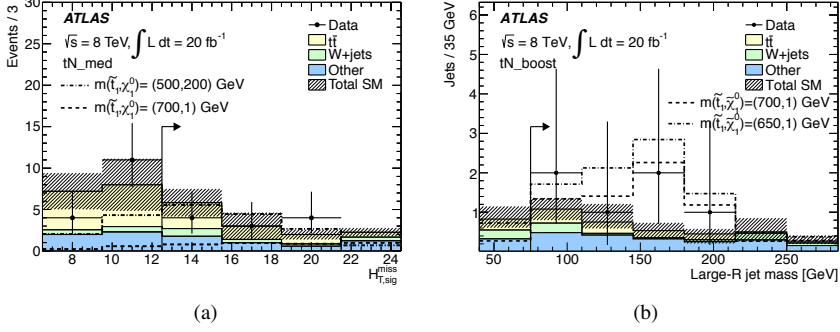


Figure 9.4: Characteristic distributions for the tN_{med} (a) and tN_{boost} (b) signal regions. The full event selection is applied, except for the requirement (indicated by an arrow) on the shown quantity. Both the statistical and all experimental systematic uncertainties are included in the uncertainty band. The last bin includes overflows. Benchmark signal models are overlaid for comparison [1].

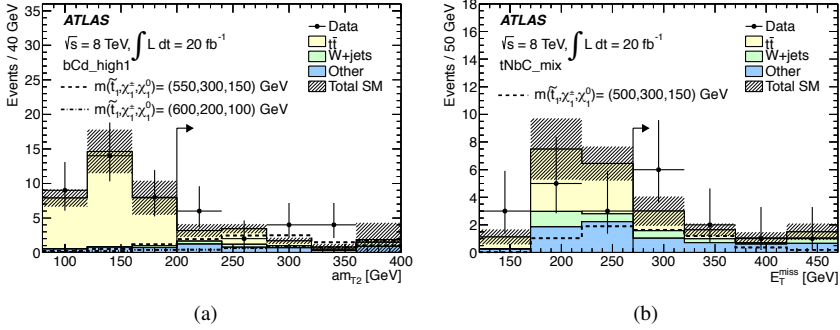


Figure 9.5: Characteristic distributions for the bCd_{high1} (a) and $tNbC_{\text{mix}}$ (b) signal regions. The full event selection is applied, except for the requirement (indicated by an arrow) on the shown quantity. Both the statistical and all experimental systematic uncertainties are included in the uncertainty band. The last bin includes overflows. Benchmark signal models are overlaid for comparison [1].

In the $\tilde{t}_1 \rightarrow t\tilde{\chi}_1^0$ scenario, a \tilde{t}_1 with a mass between 210 GeV and 670 GeV is excluded for a massless LSP. For an LSP mass around 230 GeV a \tilde{t}_1 with a mass below 600 GeV is excluded. In the $\tilde{t}_1 \rightarrow bW\tilde{\chi}_1^0$ scenario, a \tilde{t}_1 between 100 GeV and about 175 GeV

Region	Obs.	Exp. bkg.	$N_{\text{non-SM}}$	
			Obs.	Exp.
tN_med	12	13.0 ± 2.2	8.5	9.2
tN_high	5	4.97 ± 0.96	6.0	6.0
tN_boost	5	3.3 ± 0.7	7.0	5.3
bCc_diag	493	470 ± 50	110.6	95.1
bCd_high1	16	11.0 ± 1.5	13.2	8.5
bCd_high2	5	4.4 ± 0.8	6.3	5.7
tNbC_mix	10	7.2 ± 1.0	9.7	7.0
tN_diag				
$125 < E_T^{\text{miss}} < 150 \text{ GeV}, 120 < m_T < 140 \text{ GeV}$	117	136 ± 22	41.2	55.7
$125 < E_T^{\text{miss}} < 150 \text{ GeV}, m_T > 140 \text{ GeV}$	163	152 ± 20	55.4	47.8
$E_T^{\text{miss}} > 150 \text{ GeV}, 120 < m_T < 140 \text{ GeV}$	101	98 ± 13	36.1	33.9
$E_T^{\text{miss}} > 150 \text{ GeV}, m_T > 140 \text{ GeV}$	217	236 ± 29	58.7	71.4
bCb_med2				
$175 < am_{T2} < 250 \text{ GeV}, 90 < m_T < 120 \text{ GeV}$	10	12 ± 2	7.3	8.8
$175 < am_{T2} < 250 \text{ GeV}, m_T > 120 \text{ GeV}$	10	7.4 ± 1.4	9.7	7.3
$am_{T2} > 250 \text{ GeV}, 90 < m_T < 120 \text{ GeV}$	16	21 ± 4	9.3	12.3
$am_{T2} > 250 \text{ GeV}, m_T > 120 \text{ GeV}$	9	9.1 ± 1.6	7.7	7.8
bCd_bulk				
$175 < am_{T2} < 250 \text{ GeV}, 90 < m_T < 120 \text{ GeV}$	144	133 ± 22	36.1	33.9
$175 < am_{T2} < 250 \text{ GeV}, m_T > 120 \text{ GeV}$	78	73 ± 8	58.7	71.4
$am_{T2} > 250 \text{ GeV}, 90 < m_T < 120 \text{ GeV}$	61	66 ± 6	17.5	20.9
$am_{T2} > 250 \text{ GeV}, m_T > 120 \text{ GeV}$	29	26.5 ± 2.6	7.7	7.8
3body				
$80 < am_{T2} < 90 \text{ GeV}, 90 < m_T < 120 \text{ GeV}$	12	16.9 ± 2.8	7.3	9.9
$80 < am_{T2} < 90 \text{ GeV}, m_T > 120 \text{ GeV}$	8	8.4 ± 2.2	7.9	7.8
$90 < am_{T2} < 100 \text{ GeV}, 90 < m_T < 120 \text{ GeV}$	29	35 ± 4	11.7	14.7
$90 < am_{T2} < 100 \text{ GeV}, m_T > 120 \text{ GeV}$	22	29 ± 5	55.4	47.8

Table 9.7: The number of observed and expected events in each signal region [1]. The upper limits are presented in terms of the number of beyond-SM events ($N_{\text{non-SM}}$) at 95% CL. For shape fit signal regions this upper limit is calculated for each bin separately.

is excluded for massless LSP models. The exclusion is extended up to a \tilde{t}_1 mass of 300 GeV for a higher LSP mass.

In the $\tilde{t}_1 \rightarrow b\tilde{\chi}_1^\pm$ scenario, a \tilde{t}_1 with a mass between 200 GeV and 500 GeV is ex-

cluded for an LSP mass of 50 GeV and a $\tilde{\chi}_1^\pm$ mass of 100 GeV. For the signal scenario in which the chargino mass is closer to the stop mass ($m_{\tilde{t}_1} - m_{\tilde{\chi}_1^\pm} = 10$ GeV), a stop mass below the 390 GeV is excluded.

The mixed decay scenario is considered with various branching ratios of $\tilde{t}_1 \rightarrow t\tilde{\chi}_1^0$, and the exclusion contours are shown for five different values of the branching ratio in Figure 9.8. If the branching ratio is 0, then the signal models are identical to those probed in the $\tilde{t}_1 \rightarrow b\tilde{\chi}_1^\pm$ scenario where the exclusion power is weaker. As the branching ratio increases, the excluded area also extends, reaching the strongest limits at 100% branching ratio, where the models are identical to those used in the $\tilde{t}_1 \rightarrow t\tilde{\chi}_1^0$ scenario.

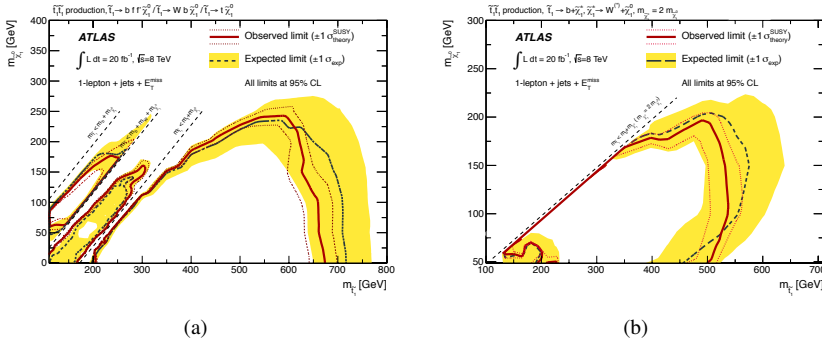


Figure 9.6: Expected (black dashed) and observed (red solid) excluded regions at 95% CL in the plane of $m_{\tilde{t}_1}$ and $m_{\tilde{\chi}_1^0}$ for $\tilde{t}_1 \rightarrow t\tilde{\chi}_1^0$ (right) and $\tilde{t}_1 \rightarrow b\tilde{\chi}_1^\pm$ (left) scenarios [1]. Each decay mode is assumed to have 100% branching ratio. The plots also include results from the soft-lepton search.

9.6 Conclusion

The analysis aims to search for direct stop pair production in the final state with exactly one isolated electron or muon, many jets, and large missing transverse energy with the ATLAS detector. The full set of 2012 data corresponding to 20.3 fb^{-1} at $\sqrt{s} = 8 \text{ TeV}$ is analyzed. The results do not show any significant excess in the data over the SM predictions in neither of the signal regions. Consequently, exclusion limits at 95% CL are placed in the \tilde{t}_1 and the LSP mass plane for pure $\tilde{t}_1 \rightarrow t\tilde{\chi}_1^0$, pure $\tilde{t}_1 \rightarrow b\tilde{\chi}_1^\pm$ and mixed decay scenarios.

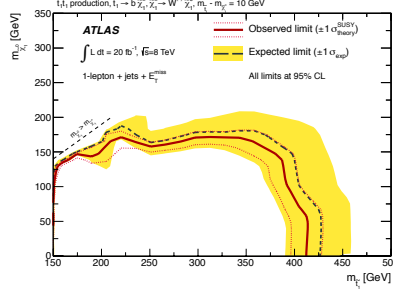


Figure 9.7: Expected (black dashed) and observed (red solid) 95% CL excluded regions in the plane of $m_{\tilde{t}_1}$ and $m_{\tilde{\chi}_1^0}$ for the $\tilde{t}_1 \rightarrow b\tilde{\chi}_1^\pm$ scenario where the chargino mass is only 10 GeV below the stop mass ($m_{\tilde{t}_1} - m_{\tilde{\chi}_1^\pm} = 10$ GeV) [1].

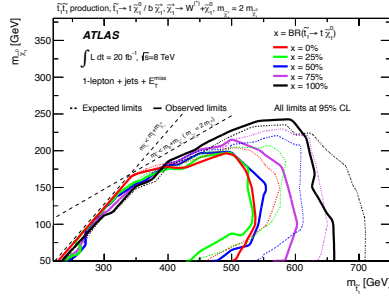


Figure 9.8: Expected (dashed) and observed (solid) limits at 95% CL in the plane of $m_{\tilde{t}_1}$ and $m_{\tilde{\chi}_1^0}$, assuming $x = \text{BR}(\tilde{t}_1 \rightarrow t\tilde{\chi}_1^0) = 1 - \text{BR}(\tilde{t}_1 \rightarrow b\tilde{\chi}_1^\pm)$, with x varying from 0% to 100% [1].

10 Interpretation of the Stop Search Results in the pMSSM

None of the SUSY searches in ATLAS performed with the 20.3 fb^{-1} of Run 1 data show evidence for physics beyond the SM. In particular, the results of the analyses described in Chapter 9 show no evidence of direct stop pair production, and consequently exclude stop masses up to around 670 GeV for lighter neutralinos. However, these exclusion limits are obtained using simplified models. In more realistic SUSY models, such as the pMSSM models (see Section 2.7), multiple stop decay modes coexist, including more complex decay chains which involve heavier charginos and neutralinos.

This chapter presents reinterpretations of the analysis presented in Chapter 9 in three different classes of pMSSM models. The three studies are aimed at probing the sensitivity of the ATLAS SUSY searches to more complex and realistic SUSY scenarios. Two different analysis methods, reco-level and truth-level analysis, are used to derive results for the various pMSSM models, and they are described in Section 10.1. The truth-level analysis is validated in Section 10.3 while the reco-level analysis is a standard method in ATLAS. The results of the analysis are presented in Section 10.4, and the conclusion is given in Section 10.5.

In the first study, the branching ratio dependence of the analysis described in Chapter 9 is investigated using the pMSSM models with fixed stop and LSP masses described in Section 2.7.1. These pMSSM models have almost identical stop and neutralino masses, but each model contains multiple stop decay modes. The impact of the additional decay modes on the exclusion limits can be presented as a function of the sum of the branching ratios of the $\tilde{t}_1 \rightarrow t\tilde{\chi}_1^0$ and $\tilde{t}_1 \rightarrow b\tilde{\chi}_1^\pm$ decays. The results are included in [1].

In the second study, the sensitivity of the 3rd generation squark studies in ATLAS to various pMSSM scenarios is probed using the 3rd generation-enriched pMSSM models described in Section 2.7.2. These pMSSM models provide a framework to combine the 3rd generation squark searches and test their sensitivity on the more complex SUSY scenarios. These results are published in [3].

In the third study, all SUSY searches in ATLAS are interpreted in the general pMSSM models described in Section 2.7.3 where all 19 parameters are scanned. Since the propagation of the particles through the ATLAS detector is the most time-consuming part of the ATLAS simulation, and since the number of pMSSM models is large, it is practically impossible to simulate the detector response for all of these models in a reasonable amount of time. In order to save computing time, analyses at Monte Carlo particle-level are performed on these models which are referred to as truth-level analyses. The corresponding results are included in [4].

10.1 Signal Models and Analysis Strategies

Two types of analysis methods are used in this chapter. One is the CL_s method, described in Section 8.5, which is used to obtain results from fully reconstructed MC and observed data. The fully reconstructed samples are referred to as reco-level samples, and the corresponding analysis as reco-level analysis. The MC samples containing generator-level information are referred to as truth-level samples, and the so-called truth-level analysis method is applied.

10.2 Analysis Methods

10.2.1 Reco-Level Analysis

This method is used to derive the exclusion limits at 95% CL on the models that passed the full ATLAS detector simulation. The full event reconstruction and the event selections constructed in the stop searches (in Chapter 9) are applied to each reco-level signal sample. The model-dependent fit configuration, including the SR and all CRs, is employed. For each model, the result from the signal region that has the best (i.e. smallest) expected CL_s value is used.

10.2.2 Truth-Level Analysis

In this analysis, the truth electrons, muons, jets and taus are used to determine the expected number of events in each of the signal regions listed in Table 10.1. These truth objects are generator-level MC objects which have passed the same kinematic requirements as the reconstructed objects described in Chapter 6. Thus, the event selections were performed on these truth objects to obtain the expected number of events.

In the truth-level analysis, the number of expected signal events is compared to the model-independent upper limit in each signal region. The expected number of events in the truth-level analysis is calculated as:

$$N_{\text{exp,truth}}^{\text{SR}} = L \times \sigma \times A_{\text{truth}}^{\text{SR}} \quad (10.1)$$

where $A_{\text{truth}}^{\text{SR}}$ is the signal acceptance for a given signal region SR, defined as the ratio of

the selected number of MC events, $N_{\text{truth}}^{\text{SR}}$, and the total number of generated MC events, $N_{\text{truth}}^{\text{total}}$. L is the integrated luminosity used for the analysis, and σ is the signal production cross section.

The expected number of events, $N_{\text{exp,truth}}^{\text{SR}}$, corrected for the average reconstruction efficiency $\epsilon^{\text{SR}} = N_{\text{exp,reco}}^{\text{SR}} / N_{\text{exp,truth}}^{\text{SR}}$, is further compared to the model-independent upper limit on the number of non-SM events in the SR, $N_{\text{UL}}^{\text{SR}}$, to give the ratio r^{SR} :

$$r^{\text{SR}} = \frac{\epsilon^{\text{SR}} \times N_{\text{exp,truth}}^{\text{SR}}}{N_{\text{UL}}^{\text{SR}}} \quad (10.2)$$

The numerator $\epsilon^{\text{SR}} \times N_{\text{exp,truth}}^{\text{SR}}$ is an approximation for the expected number of events at reco-level, where ϵ^{SR} is measured from fully reconstructed samples for each signal region. The r^{SR} shows if the number of events predicted by a model is larger than or less than the model-independent upper limit in the signal region. The r^{SR} is measured for all selected models in each signal region.

Based on the r^{SR} values, the models are split into three categories:

$$r^{\text{SR}} < r_1^{\text{SR}} : \text{Cat. 1} \quad (10.3)$$

$$r_1^{\text{SR}} < r^{\text{SR}} < r_3^{\text{SR}} : \text{Cat. 2} \quad (10.4)$$

$$r_3^{\text{SR}} < r^{\text{SR}} : \text{Cat. 3} \quad (10.5)$$

where r_1^{SR} and r_3^{SR} are the boundaries between Cat.1 and Cat.2, and between Cat.2 and Cat.3 respectively. One model may be assigned to different categories by the different signal regions. In this case, the highest category is considered. For each category, a different analysis strategy is used:

- The models in Cat.1 predict a low number of events compared to the upper limit, in all signal regions considered. Therefore, these models are most likely not excluded by any signal region in the analysis.
- The models in Cat.2 predict a number of events which is comparable to the upper limit in the most sensitive signal region. There is thus a possibility that these models could be excluded if the analysis was performed with fully reconstructed MC samples. For these models, it is hard to take a decision only based on the truth-level analysis. Therefore, these models are passed to the full ATLAS detector simulation and reconstruction, and the reco-level analysis is performed afterwards. The exclusion results are obtained from the model-dependent fit.
- The models in Cat.3 predict a number of events which is much higher than the upper limit in the most sensitive signal region, meaning that these models are certainly excluded by at least one of the signal regions.

Table 10.1 shows the list of signal regions and the values of ε , r_1 , and r_3 which are determined both from the truth-level and the reco-level analyses on the simplified models ($\tilde{t}_1 \rightarrow t\tilde{\chi}_1^0$ and $\tilde{t}_1 \rightarrow b\tilde{\chi}_1^\pm$). The boosted selection is not included in this study. The second column in the table shows the expected model-independent upper limits at 95% CL for each signal region of the analysis. The expected model-independent upper limits for shape fit signal regions are given for the four most sensitive shape fit bins separately. In the truth-level analysis, each shape fit bin is considered as an independent signal region.

Signal regions	Applied ε	N_{UL}	r_1	r_3
bCc_diag	0.88	95.1	0.7	1.5
bCd_bulk-shape-amttwo2-mt2	0.44	33.9	0.5	1.5
bCd_bulk-shape-amttwo2-mt3	0.44	71.4	0.5	1.5
bCd_bulk-shape-amttwo3-mt2	0.46	20.9	0.5	1.5
bCd_bulk-shape-amttwo3-mt3	0.46	12.6	0.3	1.5
bCd_high1	0.35	8.5	0.6	1.8
bCd_high2	0.53	5.7	0.5	2.3
bCb_med2-shape-amttwo2-mt2	0.40	8.8	0.5	1.5
bCb_med2-shape-amttwo2-mt3	0.43	7.3	0.5	1.5
bCb_med2-shape-amttwo3-mt2	0.40	12.3	0.5	1.5
bCb_med2-shape-amttwo3-mt3	0.42	7.8	0.5	1.7
3body-shape-amttwo1-mt2	0.15	9.9	0.5	1.5
3body-shape-amttwo1-mt3	0.44	7.8	0.5	1.5
3body-shape-amttwo2-mt2	0.41	14.7	0.5	1.5
3body-shape-amttwo2-mt3	0.52	47.8	0.5	1.5
tN_diag-shape-met2-mt3	0.58	55.7	0.5	1.5
tN_diag-shape-met2-mt4	0.54	47.8	0.5	1.5
tN_diag-shape-met3-mt3	0.54	33.9	0.5	1.5
tN_diag-shape-met3-mt4	0.52	71.4	0.3	1.5
tN_med	0.32	9.2	0.5	1.5
tN_high	0.55	6.0	0.5	1.5
tNbC_mix	0.50	7.0	0.7	1.5

Table 10.1: Selected signal regions from the analysis presented in Chapter 9 for the truth-level analysis in the general pMSSM interpretation. The reconstruction efficiencies ε , the expected model-independent upper limits (N_{UL}), r_1 and r_3 values, and the most sensitive bins of the two-dimensional shape fit signal regions are listed.

10.3 Validation of the Truth-Level Analysis Method

To validate that the procedure of sorting the models into the three categories does not lead to incorrect results (claiming that a model is excluded when in reality it is not or

vice versa), a small fraction of the models from the three categories is passed to the full ATLAS detector simulation and reconstruction. The three categories are then validated by comparing the results from these reco-level samples to the results from the truth-level analysis.

Figures 10.1-10.6 show validation plots for the three categories. The left plots show the comparison of the expected number of events from the truth analysis ($N_{\text{truth}}^{\text{exp}}$) and from the reco-level analysis ($N_{\text{reco}}^{\text{exp}}$). The models are split into the three categories based on the truth-level analysis. The models with green color are excluded at the 95% CL while the black color indicates the models which are not excluded based on the results of the reco-level analysis. The right plots show the r value and the reconstruction efficiency ε for each model and each signal region. The mean ε is the average reconstruction efficiency of these models, and the applied ε is the value that was chosen for the truth-level analysis (see Table 10.1). The plots show that for each signal region, the applied ε is within $\pm 1\sigma$ of the mean ε except for bCd_high1. Therefore, bCd_high1 is only sensitive to a few models.

From the Figures 10.1 - 10.3 one can see that the values of the boundaries r_1 and r_3 are well chosen for each cut-and-count signal region. In Cat.1, no model points are excluded. In contrast in Cat.3, all model points are excluded. In Cat.2, some models are excluded, and some are not excluded. This is in good agreement with the truth-level analysis results.

Compared to the cut-and-count signal regions, the two-dimensional multi-bin shape fit signal regions show weaker exclusion power at truth-level. This is because the fits in the truth-level analysis are performed on each bin separately while the reco-level analysis fits are performed on all bins simultaneously. Figures 10.4 - 10.6 show the models in the three categories for the multi-bin shape fit signal regions. The boundaries r_1 and r_3 for multi-bin shape fit signal regions are chosen such that the categories work well for at least one bin.

The validation plots for other shape fit bins and signal regions are omitted here since they do not show any sensitivity to these general pMSSM models.

10.4 Results

10.4.1 Branching Ratio Dependence of the Stop Search

The signal regions described in Chapter 9 are applied to all of the pMSSM models with fixed stop and LSP masses described in Section 2.7.1. Figure 10.7 shows the expected and observed CL_s significance values as a function of the sum of the branching ratios for the $\tilde{t}_1 \rightarrow t\tilde{\chi}_1^0$ and $\tilde{t}_1 \rightarrow b\tilde{\chi}_1^\pm$ decays. The CL_s significance is small when \tilde{t}_1 decay channels other than $\tilde{t}_1 \rightarrow t\tilde{\chi}_1^0$ and $\tilde{t}_1 \rightarrow b\tilde{\chi}_1^\pm$ are kinematically allowed.

In addition, the analysis sensitivity also depends on other parameters, e.g. the stop mixing matrix (determining if \tilde{t}_1 is mainly the partner of the right- or left-handed t quark), masses of the other sparticles and their field contents. These additional depen-

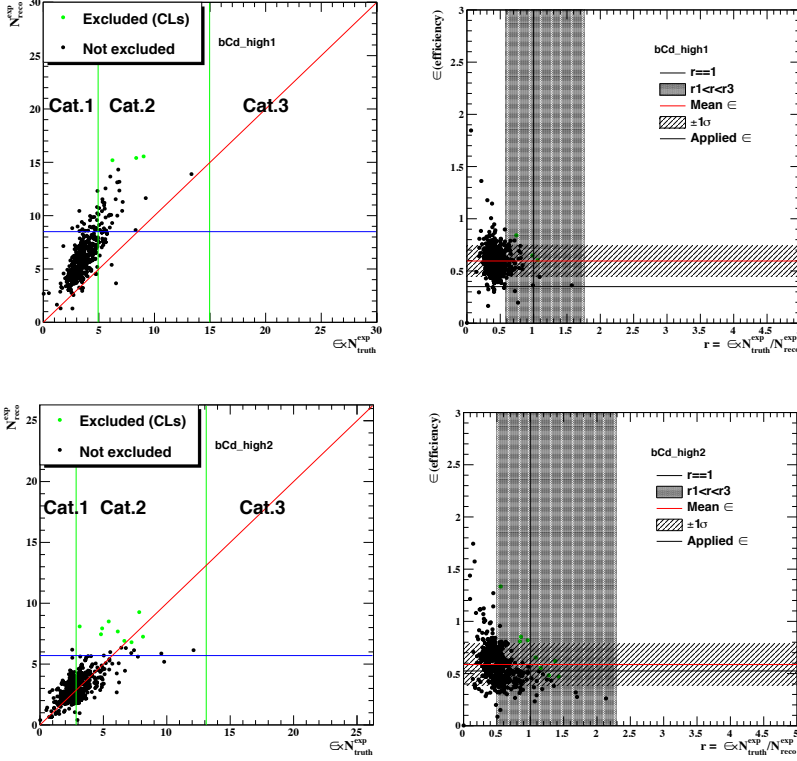


Figure 10.1: Validation of the categories for the $b\text{Cd_high1}$ and $b\text{Cd_high2}$ signal regions targeting the $\tilde{t}_1 \rightarrow b\tilde{\chi}_1^\pm$ scenarios (left) and the r value and the reconstruction efficiency ε for each model (right). $N_{\text{truth}}^{\text{exp}}$ is the expected number of events from the truth-level analysis, $N_{\text{reco}}^{\text{exp}}$ is the expected number of events from the reco-level analysis, and $\varepsilon \times N_{\text{truth}}^{\text{exp}}$ is an approximation of $N_{\text{reco}}^{\text{exp}}$ used in the truth-level analysis. The blue line in the left plot indicates the model-independent upper limit on the number of expected BSM events

dencies can explain the large spread in CL_s significance values for models that have the same branching ratios of \tilde{t}_1 decays.

10.4.2 Interpretation in the 3rd Generation-Enriched pMSSM Models

All signal region selections described in Chapter 9 are applied to the 3rd generation-enriched pMSSM models described in Section 2.7.2. Combined exclusion limits on

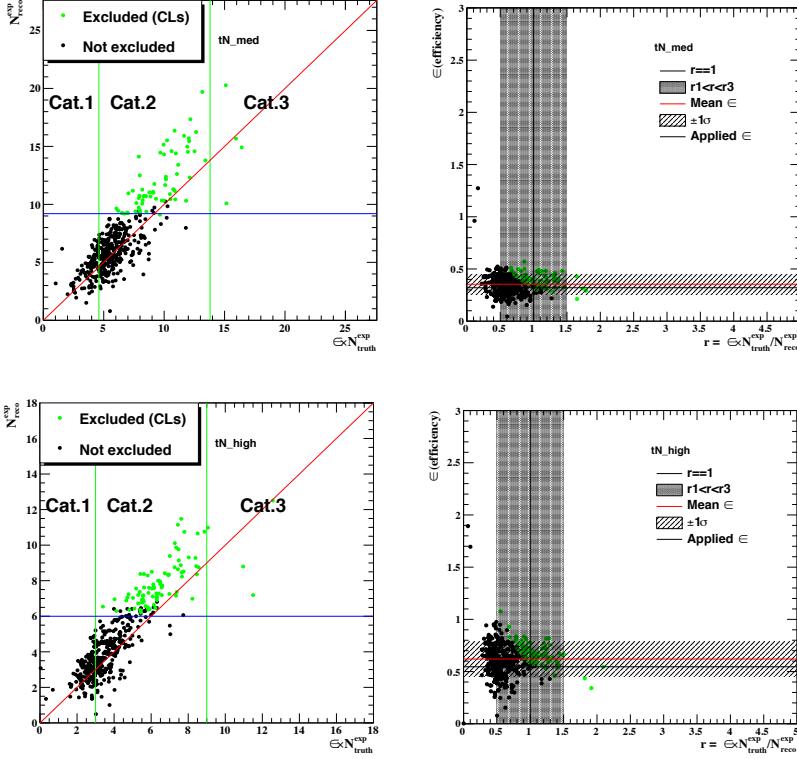


Figure 10.2: Validation of the categories for the tN_{med} and tN_{high} signal regions targeting the $\tilde{t}_1 \rightarrow t\tilde{\chi}_1^0$ scenarios (left) and the r value and the reconstruction efficiency ϵ for each model (right). $N_{\text{truth}}^{\text{exp}}$ is the expected number of events from the truth-level analysis, $N_{\text{reco}}^{\text{exp}}$ is the expected number of events from the reco-level analysis, and $\epsilon \times N_{\text{truth}}^{\text{exp}}$ is an approximation of $N_{\text{reco}}^{\text{exp}}$ used in the truth-level analysis. The blue line in the left plot indicates the model-independent upper limit on the number of expected BSM events.

relevant parameters are determined at 95% CL using the reco-level analysis method. For each model, the signal region with the best expected CL_s value is used.

Figure 10.8 shows the excluded area for naturalness-inspired pMSSM models in the μ and m_{qL3} parameter space. In these models, \tilde{t}_1 is left-handed, and \tilde{t}_1 is lighter than \tilde{b}_1 . The m_{qL3} is excluded up to 700 GeV for low μ values.

Figure 10.9 shows the exclusion limits in the M_1 - m_{qL3} plane for the left-handed \tilde{t}_1 scenario in well-tempered pMSSM models. The m_{qL3} is excluded up to 500 GeV which

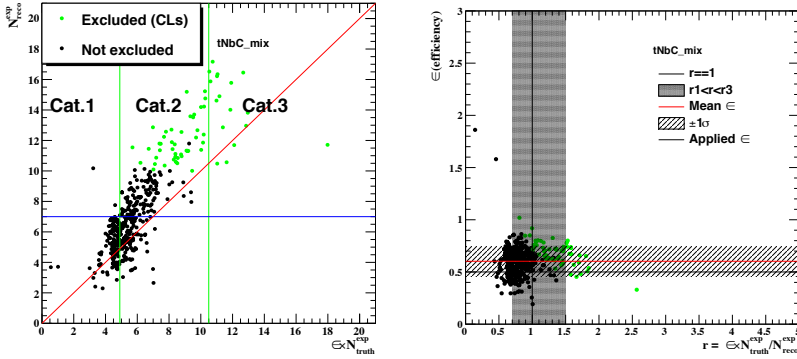


Figure 10.3: Validation of the categories for the $t\text{NbC_mix}$ signal region of mixed decay scenarios (left) and the r value and the reconstruction efficiency ϵ for each model (right). $N_{\text{truth}}^{\text{exp}}$ is the expected number of events from the truth-level analysis, $N_{\text{reco}}^{\text{exp}}$ is the expected number of events from the reco-level analysis, and $\epsilon \times N_{\text{truth}}^{\text{exp}}$ is an approximation of $N_{\text{reco}}^{\text{exp}}$ used in the truth-level analysis. The blue line in the left plot indicates the model-independent upper limit on the number of expected BSM events.

corresponds to \tilde{t}_1 masses near 500 GeV for low M_1 . The signal models with higher m_{qL3} are dominated by the stop decays other than $\tilde{t}_1 \rightarrow t\tilde{\chi}_1^0$ and $\tilde{t}_1 \rightarrow b\tilde{\chi}_1^\pm$ resulting in weaker sensitivity in these regions. The results show that the analysis does not have any sensitivity to the right-handed \tilde{t}_1 scenario in well-tempered pMSSM models.

As shown in Figure 10.10, the exclusion limits in h/Z boson-enriched pMSSM models are stronger for the left-handed \tilde{b}_1 scenario than the right-handed \tilde{b}_1 scenario. In the left-handed \tilde{b}_1 scenario, the m_{qL3} is excluded up to 650 GeV for all μ values while in the right-handed sbottom scenario the m_{qL3} is excluded between 280-420 GeV for very low values of μ . In general, the higher sensitivity in the left-handed \tilde{t}_1 and \tilde{b}_1 scenarios is a consequence of the mass spectrum of \tilde{t}_1 and \tilde{b}_1 . In the left-handed \tilde{t}_1 and \tilde{b}_1 scenarios, \tilde{t}_1 and \tilde{b}_1 have degenerate masses which results in an increase in the effective production cross section of the sparticles while in the right-handed \tilde{t}_1 scenario only the \tilde{t}_1 is produced. The larger production cross section in the left-handed \tilde{t}_1 scenario strengthens the exclusion limit.

The results presented above are only based on the search described in Chapter 9. In the same way, all 3rd generation squark searches in ATLAS have examined the same set of models. The combined results from all groups are shown in Figures 10.11-10.13. Stronger limits are obtained when including more SUSY searches as they are complementary to each other.

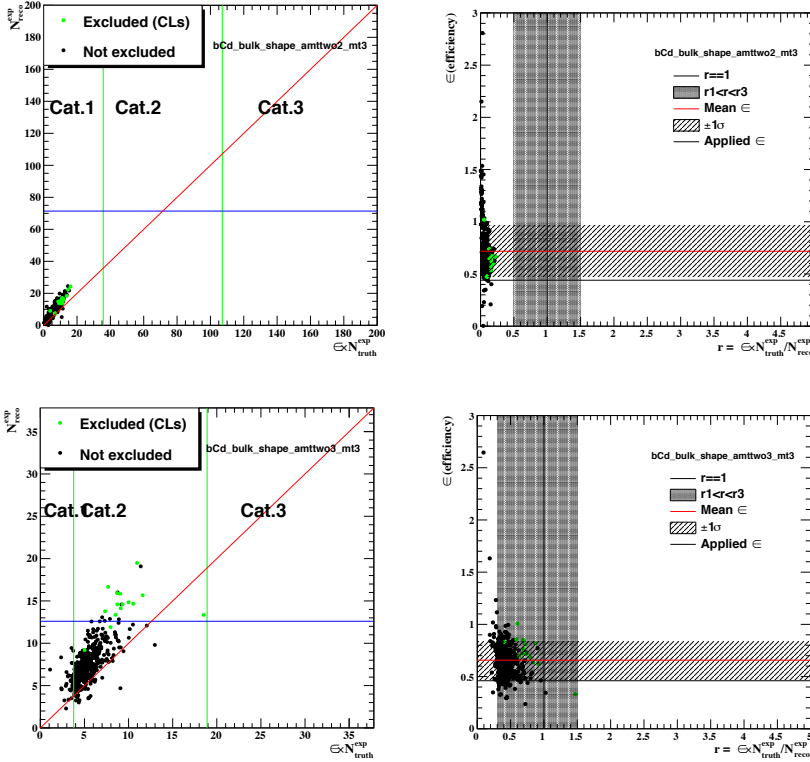


Figure 10.4: Validation of the categories for the bCd_bulk shape fit signal region targeting the $\tilde{t}_1 \rightarrow b\tilde{\chi}_1^\pm$ scenarios (left) and the r value and the ϵ for each model (right). $N_{\text{truth}}^{\text{exp}}$ is the expected number of events from the truth-level analysis, $N_{\text{reco}}^{\text{exp}}$ is the expected number of events from the reco-level analysis, and $\epsilon \times N_{\text{truth}}^{\text{exp}}$ is an approximation of $N_{\text{reco}}^{\text{exp}}$ used in the truth-level analysis. The blue line in the left plot indicates the model-independent upper limit on the number of expected BSM events.

10.4.3 Interpretation in the General pMSSM Models

For the 44,559 models falling in Cat.2 exclusion results are derived at 95% CL based on the reco-level analysis. For the models which belong to Cat.1 and Cat.3, results from the truth-level analyses are used.

All ATLAS SUSY searches are performed on these pMSSM models, and the results are combined by choosing, for each model, the most sensitive signal region out of all

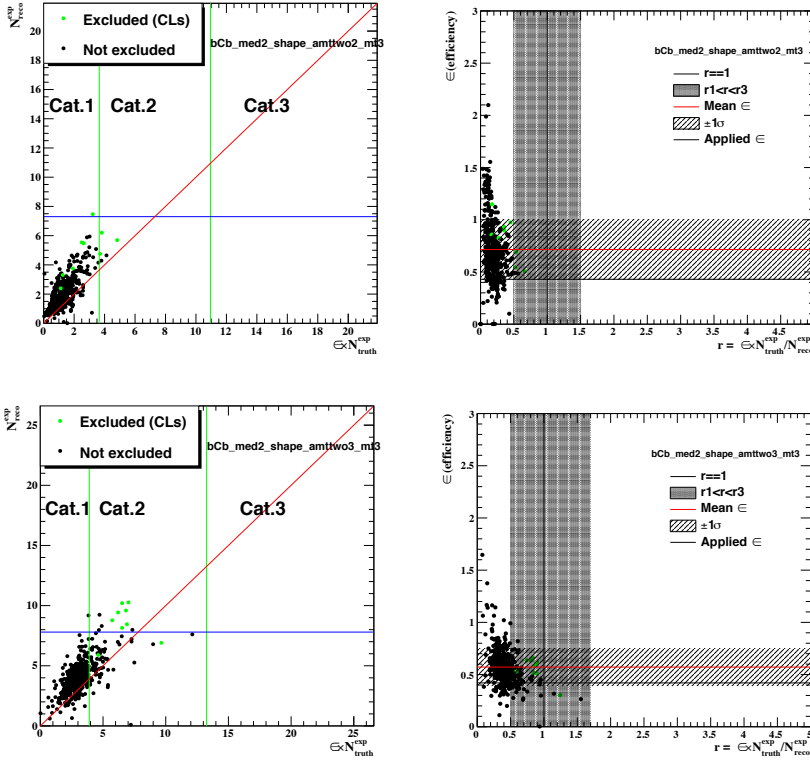


Figure 10.5: Validation of the categories for the bCb_med2 shape fit signal region targeting the $\tilde{t}_1 \rightarrow b\tilde{\chi}_1^\pm$ scenarios (left) and the r value and the ϵ for each model (right). $N_{\text{truth}}^{\text{exp}}$ is the expected number of events from the truth-level analysis, $N_{\text{reco}}^{\text{exp}}$ is the expected number of events from the reco-level analysis, and $\epsilon \times N_{\text{truth}}^{\text{exp}}$ is an approximation of $N_{\text{reco}}^{\text{exp}}$ used in the truth-level analysis. The blue line in the left plot indicates the model-independent upper limit on the number of expected BSM events.

SUSY searches. The combined results are presented as exclusion limits in the space of sparticle masses. Here, only limits in the stop-LSP mass plane are shown as they are the only parameters relevant to the stop searches described in this thesis.

Figure 10.14 shows the fraction of excluded models both when considering all ATLAS SUSY searches and when considering only the third generation squark searches. The results are projected onto the stop-LSP mass plane. The white contours in the figures show the exclusion limits at 95% CL from the analysis described in Chapter 9. The

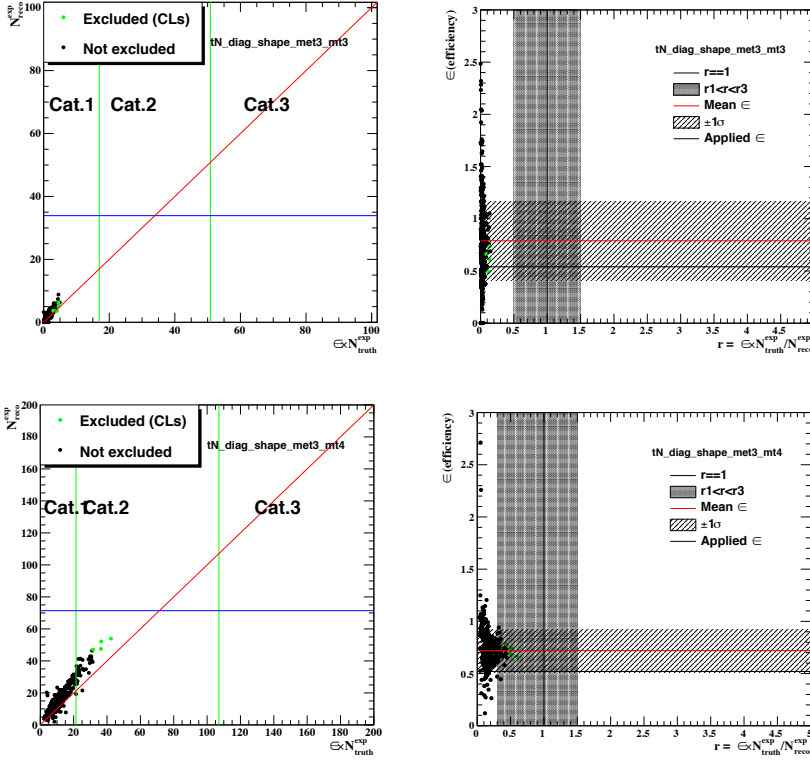


Figure 10.6: Validation of the categories for the tN_diag shape fit signal region targeting the $\tilde{t}_1 \rightarrow t\tilde{\chi}_1^0$ scenarios (left) and the r value and the ε for each model (right). N_{truth}^{exp} is the expected number of events from the truth-level analysis, N_{reco}^{exp} is the expected number of events from the reco-level analysis, and $\varepsilon \times N_{truth}^{exp}$ is an approximation of N_{reco}^{exp} used in the truth-level analysis. The blue line in the left plot indicates the model-independent upper limit on the number of expected BSM events.

results show a good agreement between the limits derived from pMSSM models and simplified models.

The third generation squark searches show good sensitivity to the models in which stop and sbottom production dominates. In most of the low mass range in the stop-LSP mass plane, 100% of the pMSSM models considered are excluded. In the stop mass range between 600 and 700 GeV, less than 100% of the models are excluded while this range is excluded in the analysis based on simplified models. This is not surprising given

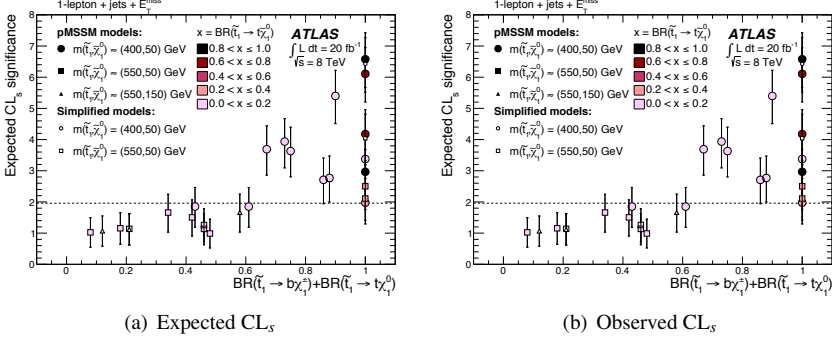


Figure 10.7: The best expected CL_s (a) and observed CL_s (b) significance values for the all 27 pMSSM models as a function of the sum of the branching ratios for the $\tilde{t}_1 \rightarrow t\tilde{\chi}_1^0$ and $\tilde{t}_1 \rightarrow b\tilde{\chi}_1^\pm$ decays. The black dashed line indicates the CL_s significance corresponding to 95% CL that above this line, models are excluded. The shape of the markers represents the different mass windows. The color of the markers indicates the branching ratio of the $\tilde{t}_1 \rightarrow t\tilde{\chi}_1^0$ decay. As a reference, the simplified models are also shown using open markers. The uncertainty bars on the expected CL_s significance include all statistical and systematic uncertainties except the uncertainties on the cross sections of the signal models. The uncertainty bars on the observed CL_s significance include the uncertainties on the cross sections of the signal models [1].

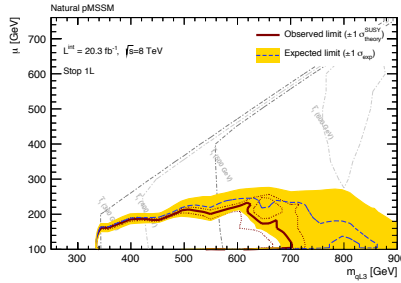


Figure 10.8: Expected and observed exclusion limits at 95% CL in the naturalness-inspired pMSSM models. The grey lines indicate contours of fixed \tilde{t}_1 mass. The shape of the \tilde{t}_1 (600 GeV) contour is due to the choice of $M_S = 800$ GeV. Even if m_{QL3} is larger, m_{tR} becomes smaller to keep M_S constant. As a result, $m_{\tilde{t}_1}$ does not exceed around 600 GeV.

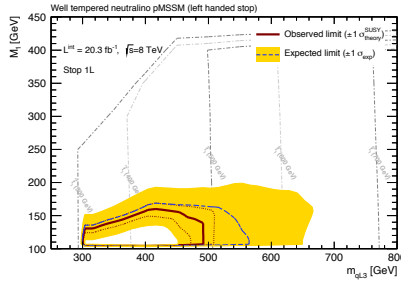


Figure 10.9: Expected and observed exclusion limits at 95% CL for the well-tempered pMSSM models in the left-handed stop scenario. The grey lines indicate contours of fixed \tilde{t}_1 mass.

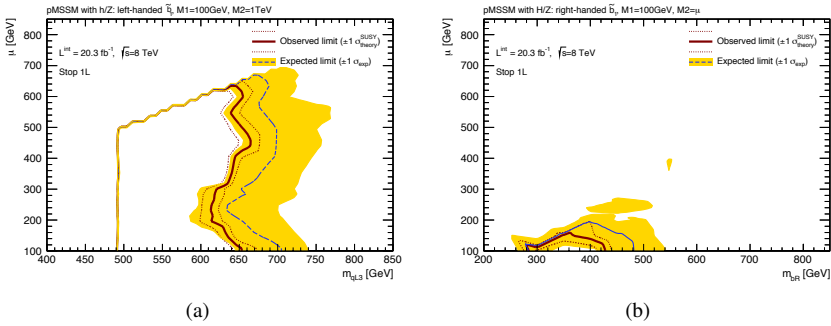


Figure 10.10: Expected and observed exclusion limits at 95% CL for the h/Z pMSSM models in the left-handed sbottom scenario (a) and the right-handed sbottom scenario (b).

the results in Section 10.4.2 showing that the sensitivity of the stop searches depends on the branching ratios of the $\tilde{t}_1 \rightarrow t\tilde{\chi}_1^0$ and $\tilde{t}_1 \rightarrow b\tilde{\chi}_1^\pm$ decays. In addition, many models also have compressed mass spectra which suppresses the sensitivity of most analyses. As shown in the figure, there is a relatively low fraction of models in the low stop mass region, which is mainly because a large radiative correction requires higher \tilde{t}_1 mass to arrive at the observed Higgs mass.

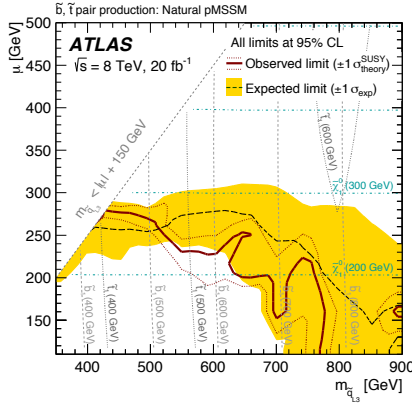


Figure 10.11: Combined result from all 3rd generation squark searches in ATLAS, showing expected and observed exclusion limits at 95% CL for the natural pMSSM models. The grey line show contours of fixed \tilde{t}_1 mass [1].

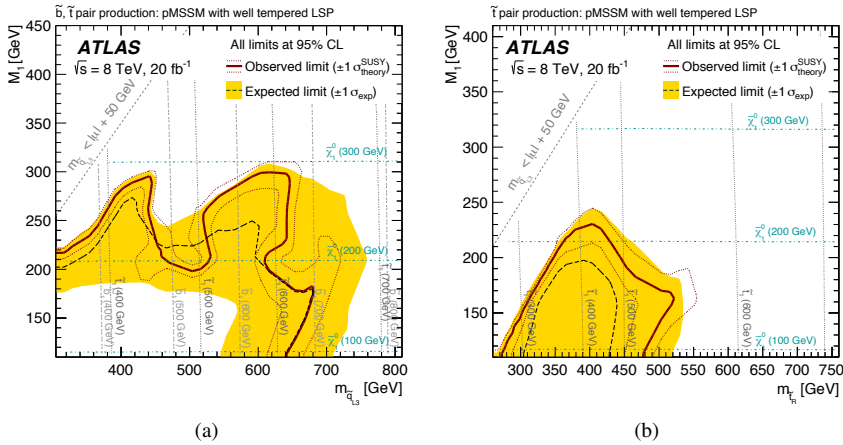


Figure 10.12: Combined result from all 3rd generation squark searches in ATLAS, showing the expected and observed exclusion limits at 95% CL for the well-tempered pMSSM models in the left-handed stop scenario (a) and the right-handed sbottom scenario (b). The grey line show contours of fixed \tilde{t}_1 mass, and the dark turquoise lines show contours of fixed $\tilde{\chi}_1^0$ masses [1].

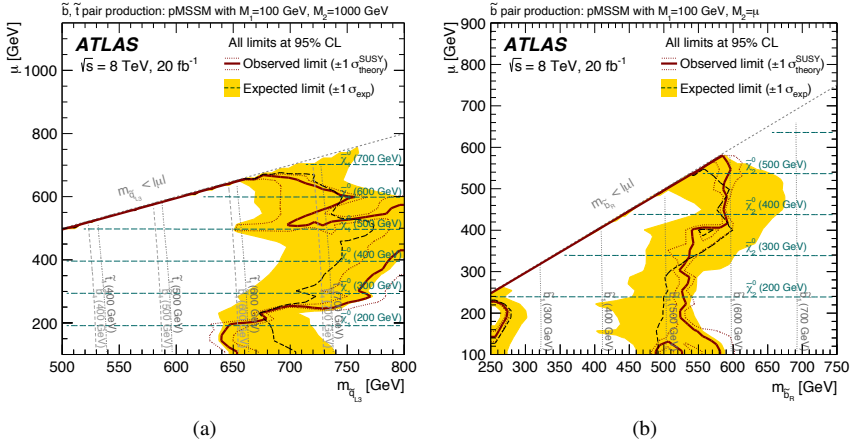


Figure 10.13: Combined result from all 3rd generation squark searches in ATLAS showing the expected and observed exclusion limits at 95% CL for the h/Z enriched pMSSM models in the left-handed sbottom scenario (a) and the right-handed sbottom scenario (b). The grey line show contours of fixed \tilde{t}_1 (if they exist) and \tilde{b}_1 masses, and the dark turquoise lines show contours of fixed $\tilde{\chi}_1^0$ or $\tilde{\chi}_2^0$ mass [1]

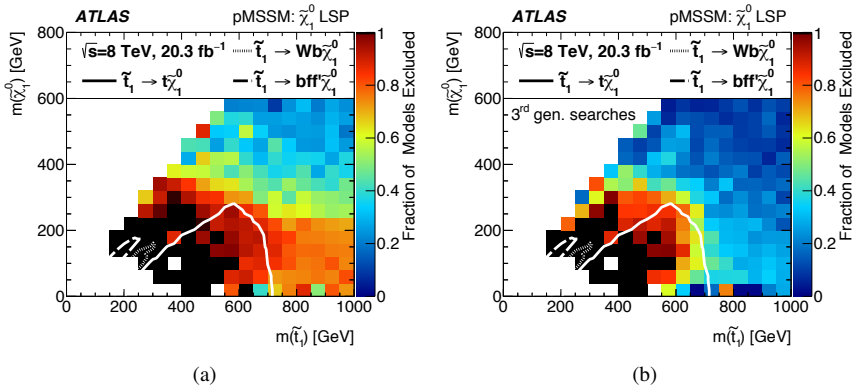


Figure 10.14: Fraction of models excluded by all SUSY searches (a), and excluded by third generation squark searches (b) [4].

10.5 Conclusions

The stop searches, in a final state with exactly one electron or muon, jets and large missing transverse energy using 20.3 fb^{-1} of data, described in Chapter 9, are interpreted in various pMSSM models. The results show that the sensitivity to pMSSM models is weaker than to simplified models where a larger area in the stop-neutralino mass plane is excluded. This is mainly due to two effects. Firstly, many pMSSM models have compressed mass spectra, and secondly, the pMSSM models include additional decay channels which are not included in the simplified models.

11 Search for Gluino-Mediated and Direct Stop Pair Production with Run 2 Data

11.1 Signal Models and Analysis Strategies

Direct gluino pair production has a higher production cross section than direct stop pair production in the pp collision at the LHC; it is about 50 times higher at the same mass (see Section 2.8). An increase in production cross section can compensate the sensitivity loss due to a low integrated luminosity from the early LHC Run 2 period.

In this chapter, a search for both gluino-mediated and direct stop pair production using 2.3 fb^{-1} of Run 2 data [5] is presented. The pair-produced gluinos are assumed to further decay into two stops and $t\bar{t}$. The stops further decay into SM particles and the LSP. In models where the stop and the LSP are mass degenerate ($m_{\tilde{t}_1} - m_{\tilde{\chi}_1^0} \lesssim 5 \text{ GeV}$), the decay products of the stop cannot be reconstructed in the detector, leading to a $t\bar{t} + E_{\text{T}}^{\text{miss}}$ signature (see Section 2.6.2). The direct stop production search has sensitivity for this subset of gluino-mediated stop production models.

In the analysis, three signal regions are constructed, targeting high gluino and stop masses. These are described in detail in Section 11.2. The dominant SM backgrounds in this analysis are $t\bar{t}$, single top (Wt channel), W +jets and $t\bar{t} + Z$. These backgrounds are estimated using dedicated control regions described in Section 11.3. Smaller backgrounds are estimated entirely from simulated events. The sources of systematic uncertainties include experimental and theoretical uncertainties which are described in Section 11.4. The results of the analysis are presented in Section 11.5. The results are interpreted in both the gluino-mediated stop and the direct stop pair production scenarios in Section 11.5. Also, a vector-like top quark (T) model, $T \rightarrow tZ$ with $Z \rightarrow \nu\bar{\nu}$, is used to interpret the results since this model has the same final state as the stop models considered.

11.2 Event Selection

11.2.1 Preselection Criteria

Each event should be triggered by an E_T^{miss} trigger which requires at least 70 GeV of E_T^{miss} , calibrated to the electromagnetic energy scale. The trigger efficiency is nearly 100% for events with at least 200 GeV of E_T^{miss} as computed off-line, which is required as a preselection criterion to all event candidates. The event candidates are further required to have at least one primary vertex, exactly one isolated charged lepton, and four or more jets. The lepton has to be an electron or muon candidate (described in Chapter 6) have $p_T > 25$ GeV, and further satisfy the signal lepton criteria. The jets must have $p_T > 25$ GeV; for jets with $p_T < 50$ GeV, an additional requirement on the jet-vertex-tagger (JVT) [170] is applied to reject pileup jets. In addition, $|\Delta\phi(\text{jet}_i, \vec{p}_T^{\text{miss}})| > 0.4$ and $m_T > 30$ GeV are applied to each event to reduce QCD multijet processes down to a negligible level. The τ veto rejects the $t\bar{t}$ events where one of the top quark decays involves a hadronically decaying τ lepton. This requirement is a modified version of the veto described in Chapter 9. The event is rejected if a reconstructed τ candidate exists and $m_{T2}^\tau < 80$ GeV, where m_{T2}^τ is calculated using the signal lepton and the signal jet originating from the hadronically decaying τ lepton. Combined with $E_T^{\text{miss}} > 200$ GeV, this cut removes a significant amount of $t\bar{t}$ events with a hadronically decaying τ lepton with a negligible impact on the signal efficiency. The preselection criteria are summarized in Table 11.1. The events which pass the preselection criteria are further selected using various signal region selections which are constructed by cutting on the discriminating variables (described in Section 8.2) to reduce SM background processes.

Preselections	Description
Trigger	E_T^{miss} trigger
Lepton	Exactly one charged lepton
Jets	At least four jets
E_T^{miss} [GeV]	> 200
$ \Delta\phi(\text{jet}_i, \vec{p}_T^{\text{miss}}) $	> 0.4 , where index i takes 1 and 2.
m_T [GeV]	> 30
m_{T2}^τ [GeV]	< 80

Table 11.1: Preselection criteria common to all the signal, control and validation regions except the dileptonic $t\bar{t}$ validation regions.

11.2.2 Signal Regions

Three signal regions are constructed to target high gluino masses (1.1 - 1.4 TeV) and high stop masses (600 - 800 GeV). The signal regions are optimized to yield the best discovery potential on the benchmark signal models. A summary of the three signal regions is shown in Table 11.2. All signal regions require larger E_T^{miss} since this is

a characteristic of all signal models. The $H_{T,\text{sig}}^{\text{miss}}$ and m_T cuts can further reduce the SM backgrounds. The am_{T2} and topness kinematic variables help to reject dileptonic $t\bar{t}$ events where the second lepton is not identified or it is a hadronically decaying τ lepton. Requiring at least one b -tagged jet can reduce the W +jets and diboson backgrounds.

SR1 is the loosest signal region and primarily targets direct stop production. In SR1, the m_{top}^χ variable is used to further suppress dileptonic $t\bar{t}$. The SR2 and SR3 signal regions target gluino-mediated stop production in a boosted topology where the t quarks have large p_T . In this case, all decay products of the hadronically decaying t quark can be captured by the single large- R jet, something which has been shown to provide better discrimination. In SR2, $R = 1.2$ jets are used while $R = 1.0$ jets were found more optimal for SR3.

Variable	SR1	SR2	SR3
≥ 4 jets with p_T [GeV]	$> (80,50,40,40)$	$> (120,80,50,25)$	$> (120,80,50,25)$
E_T^{miss} [GeV]	> 260	> 350	> 480
$H_{T,\text{sig}}^{\text{miss}}$	> 14	> 20	> 14
m_T [GeV]	> 170	> 200	> 190
am_{T2} [GeV]	> 175	> 175	> 175
topness	> 6.5	–	> 9.5
m_{top}^χ [GeV]	< 270	–	–
$\Delta R(b, l)$	< 3.0	< 2.5	< 2.8
Number of b -tagged jets	≥ 1	≥ 1	≥ 1
Leading large- R jet p_T [GeV]	–	> 200	> 280
Leading large- R jet mass [GeV]	–	> 140	> 70
$ \Delta\phi(\vec{p}_T^{\text{miss}}, 2^{\text{nd}} \text{ large-}R \text{ jet}) $	–	> 1.0	–

Table 11.2: Summary of the SR1, SR2 and SR3 signal regions.

11.3 Control and Validation Regions

The dominant backgrounds arise from $t\bar{t}$, single top (Wt channel), W +jets and $t\bar{t} + Z$. These dominant backgrounds are normalized in corresponding control regions and extrapolated to the signal regions to estimate the expected number of background events in each signal region. The extrapolation relies on transfer factors (TFs) which are obtained from the simulation. More details on this procedure are given in Section 8.4. Smaller backgrounds originate from the diboson, $t\bar{t} + W$ and Z +jets processes. They are estimated entirely from the simulation by normalizing them with the theoretical cross section.

$t\bar{t}$ Control Regions

The $t\bar{t}$ control regions (TCRs) for the three signal regions are summarized in Table 11.3. They are constructed to be orthogonal to the signal regions by requiring $30 \text{ GeV} < m_T < 90 \text{ GeV}$, while $m_T > 170 \text{ GeV}$ or higher is required for the signal regions. Some other kinematic variables are also relaxed to increase the purity of $t\bar{t}$ events in the TCRs. Also, the $am_{T2} < 200 \text{ GeV}$ requirement is added to establish orthogonality between the TCRs and the single top Wt control regions (STCRs).

Variable	TCR1	TCR2	TCR3
≥ 4 jets with p_T [GeV]	$> (80, 50, 40, 40)$	$> (120, 80, 50, 25)$	$> (120, 80, 50, 25)$
E_T^{miss} [GeV]	> 200	> 250	> 280
$H_{T,\text{sig}}^{\text{miss}}$	> 5	> 15	> 8
m_T [GeV]	[30,90]	[30,90]	[30,90]
am_{T2} [GeV]	[100,200]	[100,200]	[100,200]
topness	> 6.5	–	> 0
m_{top}^χ [GeV]	< 270	–	–
$\Delta R(b, l)$	–	–	–
Number of b -tagged jets	≥ 1	≥ 1	≥ 1
Leading large-R jet p_T [GeV]	–	> 200	> 200
Leading large-R jet mass [GeV]	–	> 140	> 70
$ \Delta\phi(\vec{p}_T^{\text{miss}}, 2^{\text{nd}} \text{ large-R jet}) $	–	> 1.0	–

Table 11.3: Summary of the TCRs corresponding to SR1, SR2 and SR3 signal regions.

Single Top Wt Control Regions

The dominant single top process contributing to the background in the signal regions is Wt . The three single top Wt control regions (STCRs) are summarized in Table 11.4. They are constructed by requiring two or more b -tagged jets which reduces the contamination from $t\bar{t}$ events in the STCRs. In addition, a $\Delta R(b_1, b_2) > 1.2$ requirement is added to the STCRs to increase the purity of Wt events. In order to increase the number of events in the STCRs, a $30 \text{ GeV} < m_T < 120 \text{ GeV}$ requirement is used instead of $30 \text{ GeV} < m_T < 90 \text{ GeV}$.

$t\bar{t} + Z$ Control Regions

The $t\bar{t} + Z$ events can not be estimated using a CR in which the Z boson decays into charged leptons since the branching ratio is too small and the number of events in the

Variable	STCR1	STCR2	STCR3
≥ 4 jets with p_T [GeV]	$> (80, 50, 40, 40)$	$> (120, 80, 50, 25)$	$> (120, 80, 50, 25)$
E_T^{miss} [GeV]	> 200	> 200	> 200
$H_{T,\text{sig}}^{\text{miss}}$	> 5	> 5	> 5
m_T [GeV]	[30,120]	[30,120]	[30,120]
am_{T2} [GeV]	> 200	> 200	> 200
topness	> 6.5	–	> 9.5
m_{top}^χ [GeV]	< 270	–	–
$\Delta R(b, l)$	–	–	–
$\Delta R(b_1, b_2)$	> 1.2	> 1.2	> 1.2
Number of b -tagged jets	≥ 2	≥ 2	≥ 2
Leading large-R jet p_T [GeV]	–	> 200	> 200
Leading large-R jet mass [GeV]	–	> 0	> 70
$ \Delta\phi(\vec{p}_T^{\text{miss}}, 2^{\text{nd}} \text{ large-R jet}) $	–	> 1.0	–

Table 11.4: Summary of the STCRs corresponding to SR1, SR2 and SR3.

simulation is limited. Therefore, a similar process, $t\bar{t} + \gamma$, is used to estimate the $t\bar{t} + Z$ indirectly. The CRs are constructed in such a way that they reduce the differences between these two processes. The events in the CRs are selected requiring a high p_T photon that is added to the E_T^{miss} to mimic the $Z \rightarrow \nu\bar{\nu}$ process. The high p_T photon is a good replacement for the Z boson in $t\bar{t} + Z$ events in the signal regions since most of them have high p_T Z bosons. The higher boson p_T requirement also reduces the differences originating from the fact that the Z boson is very massive while the photon is massless.

The two $t\bar{t} + Z$ CRs are constructed for SR1 and SR2/SR3 respectively with the following requirements:

- At least one signal photon.
- $\tilde{E}_T^{\text{miss}} > 120$ GeV, where $\tilde{E}_T^{\text{miss}} = |\vec{p}_T^{\text{miss}} + \vec{p}_T^\gamma|$.
- $\tilde{m}_T > 100$ GeV, where \tilde{m}_T is the same as m_T but calculated using $\tilde{E}_T^{\text{miss}}$.
- $\tilde{H}_{T,\text{sig}}^{\text{miss}} > 5$, where $\tilde{H}_{T,\text{sig}}^{\text{miss}}$ is the same as $H_{T,\text{sig}}^{\text{miss}}$ but calculated using $\tilde{E}_T^{\text{miss}}$.
- $E_T^{\text{miss}} < 200$ GeV. This requirement keeps the $t\bar{t} + Z$ CRs orthogonal to the SRs and other CRs.

The other requirements are the same as in the SRs. The constructed CRs are about 90% pure in $t\bar{t} + \gamma$ events. The observed data in the CRs is about 40% higher than the

prediction from simulation, but there is no significant evidence of mis-modelings of the shape of important observables in any of the backgrounds. A 4% correction factor to the theory cross section of the $t\bar{t} + \gamma$ process is applied to take into account differences in the PDF set, factorization/renormalization scale and the number of partons from the matrix element between the simulated $t\bar{t} + \gamma$ and $t\bar{t} + Z$ samples.

W+jets Control Regions

The three W+jets control regions (WCRs), shown in Table 11.5, are constructed in the same way as the TCRs, except for the application of a b -jet veto. This requirement reduces the number of $t\bar{t}$ events in the WCRs, resulting in about a 75% purity of W+jets events. There is also no upper cut on the am_{T2} in the WCRs while it exists in the TCRs.

Variable	WCR1	WCR2	WCR3
≥ 4 jets with p_T [GeV]	$> (80,50,40,40)$	$> (120,80,50,25)$	$> (120,80,50,25)$
E_T^{miss} [GeV]	> 200	> 250	> 280
$H_{T,\text{sig}}^{\text{miss}}$	> 5	> 15	> 8
m_T [GeV]	[30,90]	[30,90]	[30,90]
am_{T2} [GeV]	> 100	> 100	> 100
topness	> 6.5	–	> 0
m_{top}^{χ} [GeV]	< 270	–	–
$\Delta R(b, l)$	–	–	–
Number of b -tagged jets	$= 0$	$= 0$	$= 0$
Leading large-R jet p_T [GeV]	–	> 200	> 200
Leading large-R jet mass [GeV]	–	> 140	> 70
$ \Delta\phi(\vec{p}_T^{\text{miss}}, 2^{\text{nd}} \text{ large-R jet}) $	–	> 1.0	–

Table 11.5: Summary of the WCRs corresponding to SR1, SR2 and SR3.

Validation Regions

The validation regions (VRs) are built to monitor the normalizations of the $t\bar{t}$ and W+jets events obtained from the CRs. The VRs are constructed using the same event selections as in the TCRs and WCRs but within the m_T range of 90-120 GeV which makes the VRs orthogonal to both the CRs and SRs. In all VRs, the signal contamination is negligible.

Several additional validation regions are created for general monitoring purposes. In order to monitor dileptonic $t\bar{t}$ events, a validation region with two signal leptons (e or μ) or one signal lepton and one τ lepton is constructed. Since the dileptonic $t\bar{t}$ events only have two jets from the t quark decay, the event must have additional jets from initial or

final state radiation in order to pass the jet requirements. The modeling of these extra jets is validated in the VR. Another validation region requiring high E_T^{miss} and low am_{T2} is built to monitor the dileptonic $t\bar{t}$ events where the second lepton is not identified. A control region based on high m_T and b jet veto is constructed to examine the tail of the m_T distribution in W +jets events. No significant mis-modeling is found in any of the VRs.

11.4 Systematic Uncertainties

11.4.1 Experimental Uncertainties

The dominant experimental uncertainties arise from the calibration of the jet energy scale (JES), the modeling of the jet energy resolution (JER) [171], the modeling of the b -tagging efficiencies for b , c and light-flavor jets [158, 159], and the contributions to the E_T^{miss} soft-term from pileup and tracks which are not associated with any reconstructed objects. The assigned uncertainties on the transfer factors are about 4% to 15% from the JES, 0% to 9% from the JER, 0% to 6% from the b -tagging and 0% to 3% from the E_T^{miss} soft-term. The other experimental uncertainties are found to have a small impact on the results.

11.4.2 Theoretical Uncertainties

The theoretical uncertainties include the uncertainties on the theoretical cross sections and the uncertainties from the modeling of the SM processes.

Uncertainties on the $t\bar{t}$ and single top Wt processes

The sources of modeling uncertainties for the $t\bar{t}$ and single top Wt processes are shown in Tables 11.6 and 11.7 respectively. The uncertainty from the choice of MC generator (Hard Scatter) is estimated by comparing the POWHEG-Box+HERWIG++ and the MC5-aMC-2+HERWIG++ generators. The uncertainty from the hadronization and fragmentation modeling (Had/Frag) is estimated by comparing Pythia 6 and HERWIG++. The uncertainty from the modeling of the initial and final state radiation (Radiation) [172] is estimated from the POWHEG-Box+Pythia 6 samples with different choices for the factorization and renormalization scales. In addition, the uncertainty on the Wt background estimate from the modeling of the interference between $t\bar{t}$ and Wt is included, by comparing the prediction from an inclusive $WWbb$ sample generated with MG5-aMC-2 to the sum of the $t\bar{t}$ and Wt predictions [172]. The total theory uncertainties of 19% to 26% for the $t\bar{t}$ and 38% to 57% for the Wt processes are obtained on the transfer factors from the TCRs/STCRs to the SRs. The large uncertainty on the Wt transfer factors mainly comes from the interference between $t\bar{t}$ and Wt .

source	SR1	SR2	SR3
	Uncertainties on the TF to the SR [%]		
Hard Scatter	18 ± 6	9.2 ± 0.6	13.2 ± 1.1
Radiation	1.00 ± 0.10	22.0 ± 0.3	22.2 ± 0.4
Had/Frag	8.5 ± 1.5	11.6 ± 0.4	3.5 ± 0.2
Total	20 ± 6	26.5 ± 0.8	26.1 ± 1.2
	Uncertainties on the TF to the STCR [%]		
Hard Scatter	13.4 ± 1.5	5.1 ± 0.6	4.1 ± 0.2
Radiation	9.4 ± 0.3	19.6 ± 0.3	18.4 ± 0.2
Had/Frag	3.6 ± 0.2	3.60 ± 0.10	2.80 ± 0.10
Total	16.7 ± 1.5	29.9 ± 0.7	19.1 ± 0.2
	Uncertainties on the TF to the WCR [%]		
Hard Scatter	20 ± 2	28.4 ± 1.6	30 ± 2
Radiation	7.0 ± 0.2	18.1 ± 0.2	15.8 ± 0.2
Had/Frag	10.3 ± 0.6	20.9 ± 0.6	19.6 ± 0.7
Total	24 ± 3	39.6 ± 1.7	39 ± 2
	Uncertainties on the TF to the TVR [%]		
Hard Scatter	6.7 ± 0.2	7.7 ± 0.4	15.3 ± 0.8
Radiation	1.30 ± 0.01	0.30 ± 0.01	0.37 ± 0.01
Had/Frag	10.50 ± 0.10	8.8 ± 1.0	9.00 ± 0.10
Total	12.6 ± 0.2	11.7 ± 1.1	17.8 ± 0.9
	Uncertainties on the TF to the WVR [%]		
Hard Scatter	21.7 ± 1.0	35 ± 3	38 ± 4
Radiation	24.4 ± 0.6	24.2 ± 0.8	24.6 ± 1.1
Had/Frag	16.8 ± 0.2	17.5 ± 0.3	16.8 ± 0.3
Total	36.7 ± 1.2	46 ± 3	48 ± 4

Table 11.6: The uncertainties from the modeling of the $t\bar{t}$ background, on the transfer factors (TF s) from the TCRs to the SRs, other CRs and VRs. The precision on each estimated uncertainty is also provided.

Uncertainties on the W +jets process

As shown in Table 11.8, systematic uncertainties on the W +jets process arise from the merging of the matrix elements (CKKW), the parton shower modeling in SHERPA (QSF) and the variation of the renormalization (Renorm) and factorization (Fac) scales. In addition, the uncertainty from the choice of MC generator is also considered and estimated by comparing the SHERPA and MadGraph+Pythia 8 samples. Since the W +jets background is normalized in a b -jet veto CR, the uncertainty from the flavor composition of the W +jets events [162] in the signal region is also taken into account. The overall theory uncertainties on the transfer factors from the WCRs to SRs are estimated to be about 36-41%.

source	SR1	SR2	SR3
Uncertainties on the TF to the SR [%]			
Radiation	3.7 ± 0.2	5.1 ± 0.2	5.8 ± 0.3
Had/Frag	5.4 ± 0.4	8.5 ± 0.8	13.9 ± 1.5
Interference	37 ± 4	49 ± 6	56 ± 8
Total	38 ± 4	50 ± 6	58 ± 8
Uncertainties on the TF to the TCR [%]			
Radiation	3.69 ± 0.10	4.50 ± 0.10	6.3 ± 0.2
Had/Frag	3.17 ± 0.10	5.0 ± 0.2	2.00 ± 0.10
Interference	38.9 ± 1.4	29.6 ± 1.0	25.2 ± 0.9
Total	39.2 ± 1.4	30.3 ± 1.0	26.1 ± 0.9
Uncertainties on the TF to the WCR [%]			
Radiation	2.30 ± 0.10	4.1 ± 0.2	4.6 ± 0.3
Had/Frag	2.3 ± 0.2	12.8 ± 1.5	11.0 ± 1.7
Interference	31.9 ± 1.1	22.0 ± 0.7	17.4 ± 0.6
Total	32.1 ± 1.1	25.8 ± 1.7	21.1 ± 1.8
Uncertainties on the TF to the TVR [%]			
Radiation	5.9 ± 0.7	20 ± 4	9 ± 2
Had/Frag	1.30 ± 0.10	2.4 ± 0.2	3.9 ± 0.4
Interference	6.6 ± 0.3	16.4 ± 1.0	27 ± 2
Total	8.9 ± 0.8	26 ± 4	29 ± 3
Uncertainties on the TF to the WVR [%]			
Radiation	3.2 ± 0.4	10.5 ± 1.6	12 ± 3
Had/Frag	9.5 ± 0.5	1.30 ± 0.10	0.50 ± 0.10
Interference	10.4 ± 0.5	22.1 ± 1.2	32 ± 2
Total	14.4 ± 0.8	25 ± 2	34 ± 3

Table 11.7: The uncertainties from the modeling of the single t background, on the transfer factors (TF s) from the STCR to the SR, other CRs and VRs. Statistical precision on each estimated uncertainty is also provided.

Uncertainties on the other backgrounds

The $t\bar{t} + Z$ background is normalized in dedicated control regions with $t\bar{t} + \gamma$ events. Therefore, additional uncertainties from the correction factor applied to the $t\bar{t} + \gamma$ cross section, and from the k -factor difference between the two processes are taken into account. The total theory uncertainty is estimated to be 12% on the transfer factors from CRs to SRs.

The diboson process is estimated entirely from simulated events. Therefore, the theory uncertainty is derived from the difference in the expected number of diboson events in the SRs. Only the uncertainties on the cross section and the choice of MC generator are taken into account. The total estimated theory uncertainty is found to be 53-55%.

source	SR1	SR2	SR3
Uncertainties on the TF to the SR [%]			
CKKW	0.9	3.1	0.8
Fac	4.1	10.3	3.5
QSF	1.0	5.2	1.4
Renorm	1.9	4.7	1.1
Alternative generator	19 \pm 9	25 \pm 10	23 \pm 9
Total	19 \pm 9	28 \pm 10	24 \pm 9
Uncertainties on the TF to the STCR [%]			
CKKW	0.5	2.5	1.1
Fac	1.6	7.5	0.3
QSF	0.6	6.02	1.0
Renorm	1.1	3.1	0.2
Alternative generator	11 \pm 3	11 \pm 3	11 \pm 3
Total	11 \pm 3	15 \pm 3	11 \pm 3
Uncertainties on the TF to the TCR [%]			
CKKW	0.0	2.5	0.3
Fac	1.1	9.9	2.2
QSF	0.2	5.7	1.4
Renorm	0.5	4.9	1.2
Alternative generator	10 \pm 3	10 \pm 3	10 \pm 3
Total	10 \pm 3	16 \pm 3	11 \pm 3
Uncertainties on the TF to the WVR [%]			
CKKW	3.0	2.5	0.1
Fac	6.8	10.0	2.3
QSF	1.9	5.6	1.8
Renorm	3.4	4.8	1.0
Alternative generator	7 \pm 3	10 \pm 3	10 \pm 3
Total	11 \pm 3	16 \pm 3	10 \pm 3
Uncertainties on the TF to the TVR [%]			
CKKW	10.6	2.2	0.2
Fac	18.1	9.7	3.1
QSF	5.1	5.8	1.8
Renorm	10.2	4.8	1.4
Alternative generator	12 \pm 4	14 \pm 4	14 \pm 4
Total	27 \pm 4	19 \pm 4	14 \pm 4

Table 11.8: The uncertainties from the modeling of the W +jets background, on the transfer factors (TF s) from the WCRs to the SRs, other CRs and VRs. The first four sources of uncertainty have no statistical precision associated with them as they are evaluated by reweighting the nominal samples, while the statistical precision of the “Alternative generator” uncertainty estimated is provided.

Uncertainties on the signal models

The sources of uncertainty on the SUSY signal models comes from the prediction of the theory cross section using different PDF sets and from the variation of factorization and renormalization scales [169]. The assigned theory uncertainties are 13%-23%. For the vector-like top quark model, a total uncertainty of 10% is assigned [107].

11.5 Results

The expected number of background events in each signal region is obtained from the background-only fit using HistFitter (see Section 8.5). The expected number of background events are compared to the observed number in the data in each signal region. The expected and observed numbers of events and the corresponding p_0 value from the background-only fit are given in Table 11.9. A good agreement between the prediction and the observed data is found in SR2 and SR3. However, in SR1, 5.50 events are expected while 12 events are observed. This excess corresponds to 2.3 standard deviations above the expectation. The comparison of the data and the expected backgrounds in SR1 are shown in Figure 11.1. The observed data tend to have low E_T^{miss} and higher m_T while the signal tends to accumulate at the high end of the spectrum.

Signal region	SR1	SR2	SR3
Observed	12	1	1
Total bkg	5.50 ± 0.72	1.25 ± 0.26	1.03 ± 0.18
$t\bar{t}$	2.21 ± 0.60	0.29 ± 0.10	0.20 ± 0.07
(1L, 1L1 τ , 2L) in %	(6, 48, 46)	(0, 58, 42)	(0, 36, 64)
Single Top	0.46 ± 0.39	0.09 ± 0.08	0.10 ± 0.09
W+jets	0.71 ± 0.43	$0.15^{+0.19}_{-0.15}$	0.20 ± 0.09
$t\bar{t} + V$	1.90 ± 0.42	0.61 ± 0.14	0.41 ± 0.10
Diboson	0.23 ± 0.15	0.11 ± 0.07	0.12 ± 0.07
p_0	0.01 (2.3 σ)	0.50 (0.0 σ)	0.50 (0.0 σ)
$N_{\text{non-SM}}^{\text{limit}} \text{ exp. (95\% CL)}$	$6.4^{+3.2}_{-2.0}$	$3.6^{+2.3}_{-1.3}$	$3.5^{+2.2}_{-1.2}$
$N_{\text{non-SM}}^{\text{limit}} \text{ obs. (95\% CL)}$	13.3	3.4	3.4

Table 11.9: The observed and expected number of events in each SR, the expected number of events for each SM background, the p_0 value for the background-only hypothesis and the corresponding number of standard deviations, and the expected and observed upper limits ($N_{\text{non-SM}}^{\text{limit}}$) at 95% CL on the number of BSM events [5].

Since no significant excess is observed, the results are translated into model-independent upper limits on new physics, and into exclusion limits on the gluino-mediated stop and

direct stop production scenarios as described in Section 8.5.

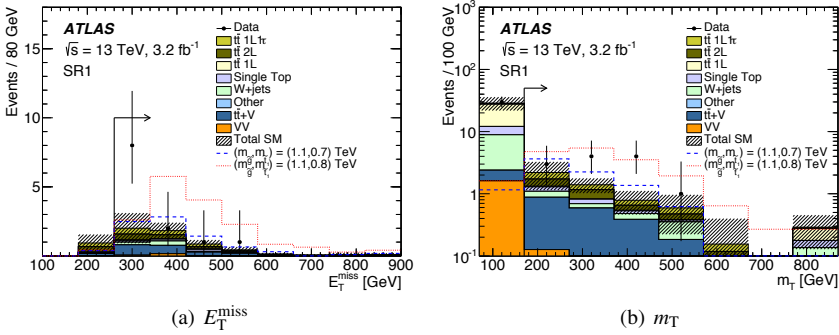


Figure 11.1: The E_T^{miss} (a) and m_T (b) distributions in SR1 for the predicted backgrounds and observed data. The full signal region selection is applied except the requirement on the plotted variable. In each plot, all statistical and experimental systematic uncertainties are included in the uncertainty band. The last bin contains the overflow. Two benchmark signal models are overlaid for comparison [5].

The model-independent upper limits at 95% CL are derived from a model-independent likelihood ratio fit by assuming no signal contribution in the CRs. The predicted and observed upper limits are shown in Table 11.9. The exclusion limits are obtained from a model-dependent fit to the SR and each CR simultaneously. The excluded mass space at 95% CL is shown in Figure 11.2. In the gluino-mediated stop production scenario, gluino masses up to about 1460 GeV are excluded for a wide range of $\tilde{\chi}_1^0$ masses. In the direct stop production scenario, there is a gap between the expected and observed exclusions. This is a consequence of the excess observed in the SR1 signal region, which is optimized to have the best sensitivity for stop masses up to 750 GeV. However, the 2.3σ discrepancy reduces the observed exclusion limits down to below stop masses of 650 GeV.

The analysis is also applied to the vector-like top quark (T) model. In this model, the T quark decays via the $T \rightarrow tZ$, $T \rightarrow tH$ and $T \rightarrow bW$ channels. The analysis described here is, however, mostly sensitive to the $T \rightarrow tZ$ channel where the $Z \rightarrow \nu\bar{\nu}$ decays results in large E_T^{miss} in the final state. The corresponding exclusion limit on the cross section times the square of the branching ratio, $\sigma \times \text{BR}(T \rightarrow tZ)^2$, as a function of the T quark mass, m_T , is shown in Figure 11.3. When the branching ratio is 100%, T quark masses up to 850 GeV are excluded.

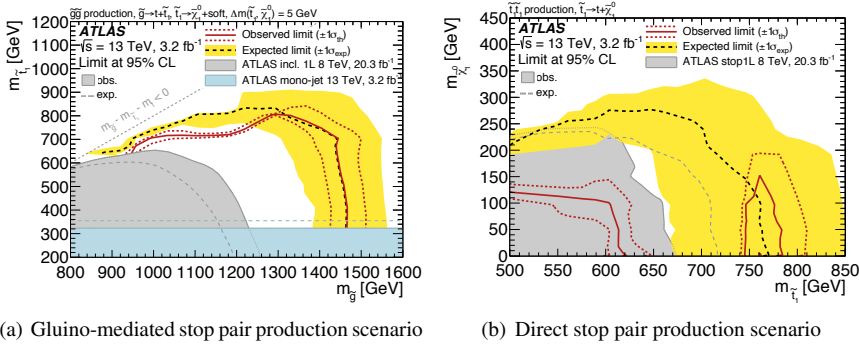


Figure 11.2: The expected and observed exclusion limits for the gluino-mediated stop pair production scenario (a) and for the direct stop pair production scenario (b) [5]. The results from the inclusive one lepton SUSY search at $\sqrt{s} = 8$ TeV [173] and the results from the monojet analysis at $\sqrt{s} = 13$ TeV [174] are also shown.

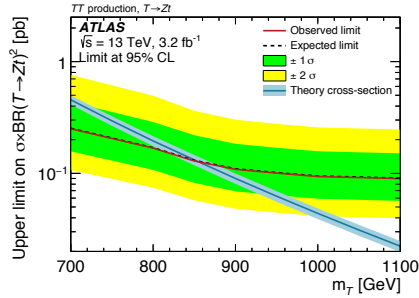


Figure 11.3: The expected and observed limits on the cross section times the square of the branching ratio of the $T \rightarrow tZ$ channel ($\sigma \times BR(T \rightarrow tZ)^2$) as a function of the T quark mass, m_T [5].

11.6 Conclusions

In this chapter, a search for gluino-mediated stop production is presented. In the scenario considered here the stop and the neutralino have a small mass difference, $m_{\tilde{t}_1} - m_{\tilde{\chi}_1^0} \lesssim 5$ GeV, resulting in the stop decay products not being reconstructed in the detector. Direct stop pair production models are also considered. The analysis uses the early Run 2 data corresponding to an integrated luminosity of 3.2 fb^{-1} collected with the ATLAS detector at $\sqrt{s} = 13$ TeV. A 2.3σ difference is seen between the expected and observed

numbers of events in SR1 while a good agreement is observed in SR2 and SR3. As a consequence, the exclusion limits on the gluino-mediated stop and direct stop production scenarios are derived at 95% CL. The results further extend the exclusion limits from Run 1 analyses up to gluino masses of 1460 GeV. In the direct stop production scenario, stop masses between 745 and 780 GeV are excluded which goes beyond the Run 1 limits shown in Chapter 9. The results are also interpreted in vector-like top quark models, where T quark masses are excluded up to 850 GeV for the $T \rightarrow tZ$ channel with 100% branching ratio.

12 Search for Direct Stop Production with Run 2 Data

12.1 Signal Models and Analysis Strategies

With the 13.2 fb^{-1} of data at $\sqrt{s} = 13 \text{ TeV}$ (including the 3.2 fb^{-1} of data from 2015) collected by July 2016, the sensitivity to direct stop pair production is expected to significantly exceed that of Run 1. Specifically, the $\tilde{t}_1 \rightarrow b\tilde{\chi}_1^\pm$ decay, which was not included in the first Run 2 analysis described in Chapter 11, can be probed for the first time at $\sqrt{s} = 13 \text{ TeV}$.

This chapter presents a search for the stop in the $\tilde{t}_1 \rightarrow b\tilde{\chi}_1^\pm$ decay mode at $\sqrt{s} = 13 \text{ TeV}$ [6]¹⁾. The simplified models considered have the mass of the $\tilde{\chi}_1^\pm$ fixed to be twice the mass of the $\tilde{\chi}_1^0$ ($m_{\tilde{\chi}_1^\pm} = 2 \times m_{\tilde{\chi}_1^0}$), and also assume 100% branching ratio of the $\tilde{t}_1 \rightarrow b\tilde{\chi}_1^\pm$ decay mode. A range of signal models, generated in a grid in the \tilde{t}_1 - $\tilde{\chi}_1^0$ - $\tilde{\chi}_1^\pm$ mass space, are simulated.

Two signal regions are constructed to cover the high stop mass regions in the \tilde{t}_1 - $\tilde{\chi}_1^0$ mass plane, with the exception of the diagonal regions. The event selections are described in Section 12.2. The dominant SM background processes are $t\bar{t}$, $t\bar{t} + V$, single top (Wt channel), and W +jets, and the numbers of events of these processes in the signal regions are estimated using control regions described in Section 12.3. The smaller backgrounds are estimated entirely from simulated events. The sources of systematic uncertainties are discussed in Section 12.4. The results and conclusions are given in Sections 12.5 and 12.6.

¹⁾The reference also includes searches for the stop in the $\tilde{t}_1 \rightarrow t\tilde{\chi}_1^0$ as well as searches for Dark Matter production in association with top quarks. These analyses are not part of this thesis.

12.2 Event Selection

12.2.1 Preselection Criteria

Event candidates are first required to fulfill a set of preselection criteria which are identical to those described in Section 11.2.1, with the exception of the trigger requirement. An E_T^{miss} trigger with a threshold of 80 GeV is used for 2015 data, while E_T^{miss} triggers with 80 GeV and 100 GeV thresholds are used for 2016 data. Additional data corresponding to the $t\bar{t} + \gamma$ process are selected with a photon trigger requiring $p_T > 140$ GeV.

The events that pass the preselection criteria are further subject to constraints corresponding to two signal regions. The signal regions are constructed using various kinematic variables that are already described in Sections 8.2 and 11.2.

12.2.2 Signal Regions

Two signal regions, bC2x_med and bC2x_diag, are constructed to cover a wide range of masses in the \tilde{t}_1 - $\tilde{\chi}_1^0$ mass plane. The bC2x_med signal region covers the space where the mass of the $\tilde{\chi}_1^\pm$ lies right in between the masses of the \tilde{t}_1 and the $\tilde{\chi}_1^0$. In this mass space, both b jets have high p_T . Therefore, the bC2x_med signal region requires at least two high- p_T b jets. The bC2x_diag signal region covers the mass space where the mass difference between the \tilde{t}_1 and the $\tilde{\chi}_1^\pm$ is smaller. In this mass space, both b jets have lower p_T , but still high enough for them to be reconstructed in the detector. Therefore, the bC2x_diag signal region requires at least two b jets with moderate p_T requirements.

The exact signal region definitions are given in Table 12.1. Compared to the signal regions targeting the $\tilde{t}_1 \rightarrow t\tilde{\chi}_1^0$ final state, described in Chapter 11, some kinematic requirements are looser. For example, the E_T^{miss} cuts are 210 GeV and 230 GeV in bC2x_med and bC2x_diag respectively. This is because of the $\tilde{\chi}_1^0$ not originating directly from the \tilde{t}_1 . The m_T is slightly higher in the bC2x_diag signal region since the $\tilde{\chi}_1^\pm$ and $\tilde{\chi}_1^0$ have a larger mass difference which results in a boost of the W boson.

Both of the signal regions are optimized to have good discovery significance over the desired mass space, assuming an integrated luminosity of 10 fb^{-1} . The significance is calculated using the BinomialExpZ function in the RooStats package [175], and is shown for each signal model point in Figure 12.1. In addition to the targeted regions, the bC2x_med signal region is found to also have reasonable sensitivity in the low $\tilde{\chi}_1^0$ mass region where the $\tilde{\chi}_1^\pm$ and the $\tilde{\chi}_1^0$ are closer in mass ($m_{\tilde{\chi}_1^\pm} - m_{\tilde{\chi}_1^0} \lesssim m_W$).

12.3 Control and Validation Regions

12.3.1 $t\bar{t}$ Control Regions

The $t\bar{t}$ control regions (TCRs) are constructed by altering the m_T and am_{T2} requirements; $30 \text{ GeV} < m_T < 90 \text{ GeV}$ and $100 \text{ GeV} < am_{T2} < 210 \text{ GeV}$ ($100 \text{ GeV} <$

Variable	bC2x_med	bC2x_diag
Number of b -tagged jets	≥ 2	≥ 2
≥ 4 jets with p_T [GeV]	$> (170, 110, 25, 25)$	$> (70, 60, 55, 25)$
≥ 2 b jets with p_T [GeV]	$> (105, 100)$	$> (25, 25)$
E_T^{miss} [GeV]	> 210	> 230
$ \Delta\phi(\text{jet}_1, \vec{p}_T^{\text{miss}}) $	> 1.0	> 1.2
$ \Delta\phi(\text{jet}_2, \vec{p}_T^{\text{miss}}) $	> 0.8	> 0.8
m_T [GeV]	> 140	> 170
am_{T2} [GeV]	> 210	> 170
$H_{T,\text{sig}}^{\text{miss}}$	> 7	> 14

Table 12.1: Summary of the selection criteria defining the two signal regions. The common event preselection as defined in Section 12.2.1 is applied in all cases.

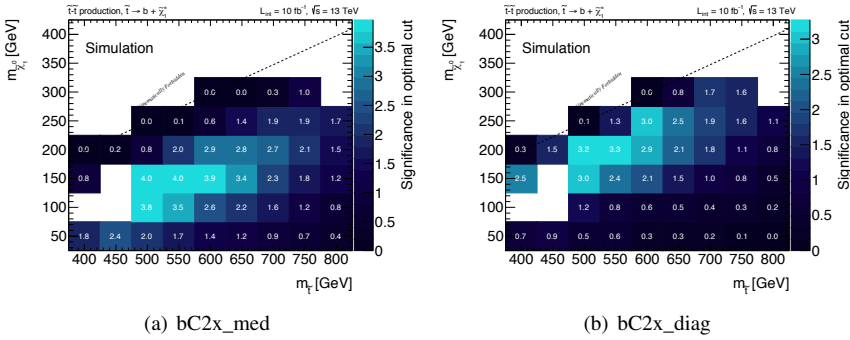


Figure 12.1: The expected discovery significance of the bC2x_med (a) and bC2x_diag (b) signal regions. A 20% systematic uncertainty and the full statistical uncertainty is included in the significance calculation.

$am_{T2} < 200$ GeV for the bC2x_diag TCR). The am_{T2} cut is applied to ensure orthogonality between the TCR and single top Wt control region (STCR). The full set of selection criteria for the TCRs are given in Table 12.2.

12.3.2 Single top Wt Control Regions

The single top Wt control regions (STCRs) require $30 \text{ GeV} < m_T < 120 \text{ GeV}$. They are made orthogonal to the TCRs by means of an altered am_{T2} requirement. In addition, a

Variable	bC2x_med_TCR	bC2x_diag_TCR
Number of b -tagged jets	≥ 2	≥ 2
≥ 4 jets with p_T [GeV]	$> (170, 110, 25, 25)$	$> (70, 60, 55, 25)$
≥ 2 b jets with p_T [GeV]	$> (105, 100)$	$> (25, 25)$
$ \Delta\phi(\text{jet}_1, \vec{p}_T^{\text{miss}}) $	> 1.0	> 1.2
$ \Delta\phi(\text{jet}_2, \vec{p}_T^{\text{miss}}) $	> 0.8	> 0.8
E_T^{miss} [GeV]	> 210	> 230
m_T [GeV]	[30, 90]	[30, 90]
am_{T2} [GeV]	[100, 210]	[100, 200]
$H_{T,\text{sig}}^{\text{miss}}$	> 7	> 14

Table 12.2: The $t\bar{t}$ control region definitions for the bC2x_med and bC2x_diag signal regions.

$\Delta R(b_1, b_2)$ requirement is introduced to suppress the $t\bar{t}$ events, and hence increase the purity of single top Wt events. Other cuts are kept the same as in the SRs. The full lists of selection criteria are shown in Table 12.3.

Variable	bC2x_med_STCR	bC2x_diag_STCR
Number of b -tagged jets	≥ 2	≥ 2
≥ 4 jets with p_T [GeV]	$> (170, 110, 25, 25)$	$> (70, 60, 55, 25)$
≥ 2 b jets with p_T [GeV]	$> (105, 100)$	$> (25, 25)$
$ \Delta\phi(\text{jet}_1, \vec{p}_T^{\text{miss}}) $	> 1.0	> 1.2
$ \Delta\phi(\text{jet}_2, \vec{p}_T^{\text{miss}}) $	> 0.8	> 0.8
E_T^{miss} [GeV]	> 210	> 230
m_T [GeV]	[30, 120]	[30, 120]
am_{T2} [GeV]	> 210	200
$H_{T,\text{sig}}^{\text{miss}}$	> 7	> 5
$\Delta R(b_1, b_2)$	> 1.2	> 1.4

Table 12.3: The single top Wt control region definitions for the bC2x_med and bC2x_diag signal regions.

12.3.3 W +jets Control Regions

The W +jets control regions (WCRs) are constructed by requiring exactly zero b -jets in the events (b veto). The W +jets events are dominant in the b veto region since the $t\bar{t}$ and

other backgrounds are significantly suppressed. In addition, a $30 \text{ GeV} < m_T < 90 \text{ GeV}$ requirement is made. Other cuts are kept the same as in the SRs. The full lists of selection criteria are given in Table 12.4.

Variable	bC2x_med_WCR	bC2x_diag_WCR
Number of b tagged jets	= 0	= 0
≥ 4 jets with p_T [GeV]	$> (170, 110, 25, 25)$	$> (70, 60, 55, 25)$
≥ 2 b -jets with p_T [GeV]	–	–
$ \Delta\phi(\text{jet}_1, \vec{p}_T^{\text{miss}}) $	> 1.0	> 1.2
$ \Delta\phi(\text{jet}_2, \vec{p}_T^{\text{miss}}) $	> 0.8	> 0.8
E_T^{miss} [GeV]	> 210	> 230
m_T [GeV]	[30, 90]	[30, 90]
am_{T2} [GeV]	> 210	170
$H_{T,\text{sig}}^{\text{miss}}$	> 7	> 14

Table 12.4: The W +jets control region definitions for the bC2x_med and bC2x_diag signal regions.

12.3.4 $t\bar{t} + Z$ Control Regions

The $t\bar{t} + Z$ background is estimated using $t\bar{t} + \gamma$ events in the $t\bar{t} + Z$ control regions, analogous to what is described in Section 11.3. The $t\bar{t} + Z$ CRs are constructed by requiring at least one photon with $p_T > 140 \text{ GeV}$, and applying the kinematic cuts shown in Table 12.5. The rest of the requirements are the same as in the SRs.

Variable	Cut
$\tilde{E}_T^{\text{miss}}$	$> 120 \text{ GeV}$
\tilde{m}_T	$> 110 \text{ GeV}$
$\tilde{H}_{T,\text{sig}}^{\text{miss}}$	> 5
E_T^{miss}	$< 200 \text{ GeV}$

Table 12.5: Kinematic variables and cuts used to construct the $t\bar{t} + Z$ CRs. The variables are described in Section 11.3.

12.3.5 Validation Regions

For each SR, an associated top validation region (TVR) and a W +jets validation region (WVR) are built to monitor the normalization of the top and W +jets events in the TCR and WCR. The validation regions are identical to the TCRs and WCRs except that the

m_T requirement is $90 \text{ GeV} < m_T < 120 \text{ GeV}$. Other validation regions, which are not associated to any SR, are used for general monitoring purposes as discussed in Section 11.3.

12.4 Systematic Uncertainties

Systematic uncertainties have both experimental and theoretical origin. The sources of these uncertainties and the techniques used to estimate them are already described in Section 11.4. As the MC modeling only affects the extrapolation from CRs to SR, the uncertainties on the transfer factors are estimated. The dominant sources of experimental uncertainties arise from JES and JER [171], modeling of b -tagging [158, 159] and the E_T^{miss} soft-term. The uncertainty ranges for the JES and JER are 4-15% and 0-9%, for the modeling of b -tagging is 0-6% and for the E_T^{miss} soft-term the range is estimated to 0-3%. Uncertainties from the other sources of experimental uncertainty such as the modeling of lepton- and photon-related quantities and the uncertainty in the integrated luminosity are small and thus have a small impact on the results.

The theoretical uncertainties arise from the choice of the MC generator, modeling of hadronization and fragmentation, the modeling of the initial- and final-state radiations and the calculation of the cross section. For the W +jets events, the total uncertainty also includes the uncertainty that arise from the flavor composition in the signal regions [162]. Table 12.6 shows total theoretical uncertainties on the transfer factors for the dominant backgrounds.

Sample	bC2x_med [%]	bC2x_diag [%]
$t\bar{t}$	17	17
single top Wt	14	25
W +jets	40	40
$t\bar{t} + V$	12	12

Table 12.6: Total theoretical uncertainties on the transfer factors for the dominant backgrounds.

The uncertainty on the diboson background is estimated in each SR. The total theoretical uncertainty on the number of events is 27% in the bC2x_med signal region and 29% in the bC2x_diag signal region. Uncertainties on the SUSY signal models are 13% to 23% as discussed in Section 11.4.

12.5 Results

The observed numbers of events and SM predictions are shown in Table 12.7. For each SR, the observed numbers of events in the corresponding CRs are obtained using a background-only fit to CRs, while the numbers of events in the SR and the correspond-

Signal region	bC2x_diag	bC2x_med
Observed	37	14
Total background	22 ± 3	13 ± 2
$t\bar{t}$	6.5 ± 1.5	4.3 ± 1.0
W +jets	1.2 ± 0.5	0.63 ± 0.29
Single top	5.3 ± 1.8	5.1 ± 1.6
$t\bar{t} + V$	8.3 ± 1.7	2.7 ± 0.7
Diboson	0.45 ± 0.17	0.42 ± 0.20
Z +jets	0.32 ± 0.29	0.08 ± 0.08
p_0 (σ)	0.00433 (2.6)	0.40 (0.26)
$N_{\text{non-SM}}^{\text{limit exp. (95\% CL)}}$	$12.4^{+5.4}_{-3.7}$	$9.0^{+4.2}_{-2.7}$
$N_{\text{non-SM}}^{\text{limit obs. (95\% CL)}}$	27.5	9.9

Table 12.7: The number of observed events, the SM background expectations, the probability (p_0) of the observed number of events being compatible with the SM expectation, and the expected and observed upper limits on the number of non-SM events are shown for each signal region. The uncertainties include both theoretical and experimental sources [6].

ing VRs are obtained using extrapolations from the CRs to the SR and VRs. Comparisons of the observed data and the SM predictions in the signal regions are shown in Figure 12.2. In the bC2x_diag signal region 37 events are observed while 22 events are predicted. This small excess corresponds to 2.6 standard deviations (σ) and is thus not significant. Therefore, model-independent upper limits on the number of non-SM events are derived at 95% CL for each signal region.

The results of this analysis are also interpreted in the $\tilde{t}_1 \rightarrow b\tilde{\chi}_1^\pm$ scenario. Figure 12.3 shows the excluded stop, chargino and neutralino masses at 95% CL. Although the expected exclusion limits extend up to stop masses of about 750 GeV for a neutralino mass of 150 GeV, the observed exclusion limits are much weaker for higher neutralino masses due to the excess in the bC2x_diag signal region.

12.6 Conclusions

In this chapter, a search for direct stop pair production in the $\tilde{t}_1 \rightarrow b\tilde{\chi}_1^\pm$ decay mode is performed with 13.2 fb^{-1} of data at $\sqrt{s} = 13 \text{ TeV}$. This data set includes 3.2 fb^{-1} of 2015 data and 10 fb^{-1} of 2016 data. The observed number of events in the bC2x_med signal region agrees well with the SM prediction, while the number of observed events

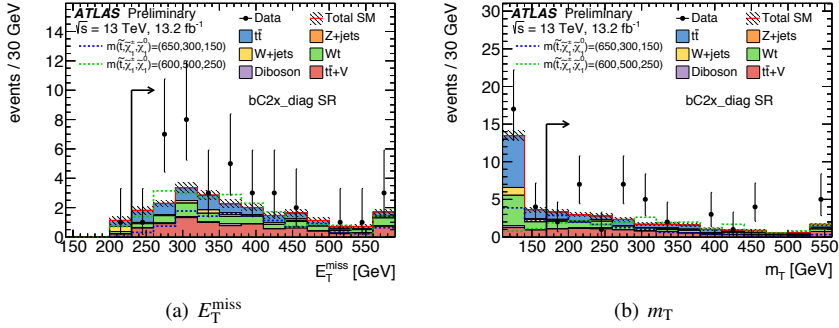


Figure 12.2: The E_T^{miss} (a) and m_T (b) distributions in the bc2x_diag signal region for the predicted backgrounds and observed data. The full signal region selection is applied except the requirement on the plotted variable. In each plot, all statistical and experimental systematic uncertainties are included in the uncertainty band. The last bin contains the overflow. Two benchmark signal models are overlaid for comparison [6].

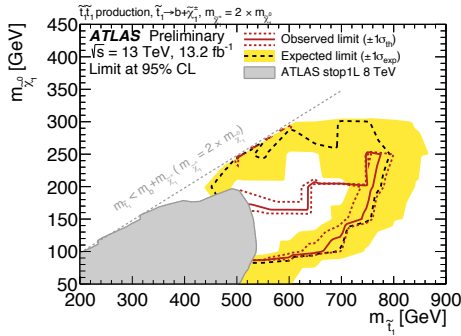


Figure 12.3: The expected (black dashed line) and observed (red solid line) exclusion contours in the $m_{\tilde{t}_1} - m_{\tilde{\chi}_1^0}$ plane for the $\tilde{t}_1 \rightarrow b\tilde{\chi}_1^\pm$ scenario [6]. In addition to bc2x_med and bc2x_diag, the plot also contains results from a signal region targeting the $m_{\tilde{t}_1} - m_{\tilde{\chi}_1^\pm} = 10$ GeV scenario which is not described in this thesis. The yellow band corresponds to the $\pm 1\sigma$ experimental uncertainty, and the gray area shows the Run 1 limits described in Chapter 9.

in the bc2x_diag signal region is larger than the SM background expectation by 2.6σ . This results in observed exclusion limits in the $\tilde{t}_1 - \tilde{\chi}_1^0$ mass plane which are weaker than

those expected.

Conclusion

If SUSY exists, it might be spontaneously broken. Such a broken symmetry would solve many problems, for example, the fine-tuning problem of the Higgs boson mass. A direct confirmation of the existence of SUSY would be the production of sparticles in the proton-proton collisions at the LHC. This thesis presents searches for a stop, the supersymmetric partner of the top quark, with data recorded by the ATLAS detector.

A well reconstructed primary vertex is important in essentially all physics analyses in the ATLAS experiment. This thesis includes a study of the primary vertex reconstruction performance in $\sqrt{s} = 7$ TeV data and simulation using $t\bar{t}$ and Z events in the final state containing two muons. One important performance measure is how often the tracks originating from a single proton-proton collision give rise to two reconstructed primary vertices (referred to as a split primary vertex). The fraction of events with a split primary vertex is estimated by counting the number of events where the two muons are associated to two different reconstructed primary vertices. The results of the study show that the fraction of split vertices is very small, and consistent between data and simulation within uncertainties.

A light stop is motivated by natural SUSY in which the stop should cancel the large radiative correction from the top quark to the Higgs boson mass. This thesis presents three searches for evidence for stop pair production at $\sqrt{s} = 8$ TeV and $\sqrt{s} = 13$ TeV, performed in final states containing exactly one isolated electron or muon, four or more jets and large missing transverse energy. Neither of the analyses show a significant excess in data over the SM predictions.

The first analysis is a search for direct stop pair production using Run 1 data at $\sqrt{s} = 8$ TeV and an integrated luminosity of 20.3 fb^{-1} . In this analysis several stop decay scenarios, $\tilde{t}_1 \rightarrow t\tilde{\chi}_1^0$, $\tilde{t}_1 \rightarrow bW\tilde{\chi}_1^0$ and $\tilde{t}_1 \rightarrow b\tilde{\chi}_1^\pm$ are considered. In the $\tilde{t}_1 \rightarrow t\tilde{\chi}_1^0$ scenario, stop masses below 670 GeV are excluded for models with a massless LSP, and stop masses below 600 GeV are excluded for LSP masses up to 230 GeV. In the $\tilde{t}_1 \rightarrow bW\tilde{\chi}_1^0$ scenario, stop masses between 100 GeV and 175 GeV are excluded for a massless LSP scenario and the exclusion is extended up to 300 GeV in the case of a more massive LSP. In the $\tilde{t}_1 \rightarrow b\tilde{\chi}_1^\pm$ scenario with $m_{\tilde{\chi}_1^\pm} = 2 \times m_{\tilde{\chi}_1^0}$, the stop mass range 200-500 GeV is excluded for an LSP mass of 50 GeV while for the $m_{\tilde{t}_1} - m_{\tilde{\chi}_1^\pm} = 10$ GeV mass hierarchy, stop masses below 390 GeV are excluded.

The sensitivity of the $\sqrt{s} = 8$ TeV analysis is also studied in various pMSSM models. The branching ratio dependence of the sensitivity of the analysis is investigated using 27 pMSSM models with fixed stop and LSP masses. The results of the analysis are also reinterpreted in 3rd generation-enriched pMSSM models and general pMSSM models. In general, the sensitivity is weaker in pMSSM models than in simplified models due to the more complex decay channels of the stop and the compressed mass spectra of the sparticles.

The second analysis is a search for both gluino-mediated and direct stop pair production scenarios using 3.2 fb^{-1} of data at $\sqrt{s} = 13$ TeV. In this analysis the $\tilde{t}_1 \rightarrow t\tilde{\chi}_1^0$ decay channel is considered. The analysis is also used to search for vector-like top quark production. In the gluino-mediated stop production scenario, the exclusion limits on the gluino mass from Run 1 are extended up to 1460 GeV. In the direct stop pair production scenario, stop masses between 745 GeV and 780 GeV are excluded. This leaves a gap between the Run 1 and Run 2 exclusion limits which is caused by a 2.3σ excess in one of the signal regions. In the vector-like top quark scenario, the sensitivity depends on the branching ratio of the $T \rightarrow tZ$ channel; vector-like top quark masses up to 850 GeV are excluded when assuming 100% branching ratio for the $T \rightarrow tZ$ channel.

The third analysis is a search for direct stop pair production in the $\tilde{t}_1 \rightarrow b\tilde{\chi}_1^\pm$ decay channel using 13.2 fb^{-1} of data at $\sqrt{s} = 13$ TeV. In this analysis, the Run 1 exclusion limits are extended up to stop masses of about 750 GeV for an LSP mass of 150 GeV. However, the observed exclusion limits are weaker than the expected ones at higher LSP masses due to a 2.6σ excess in one of the signal regions.

Although no significant excess of events has been observed in the analyses presented in this thesis, the sensitivity to large stop masses and more challenging regions of the parameter space will improve as more data is collected. So far, the ATLAS experiment has recorded approximately 16 fb^{-1} of data at $\sqrt{s} = 13$ TeV, while the expected integrated luminosity at the end of Run 3 is 300 fb^{-1} .

References

- [1] ATLAS Collaboration, *Search for top squark pair production in final states with one isolated lepton, jets, and missing transverse momentum in $\sqrt{s}=8$ TeV pp collisions with the ATLAS detector*, JHEP **11** (2014) 118, [arXiv:1407.0583 \[hep-ex\]](#).
- [2] A. Yiming, *Search for top squark pair production in final states with one isolated lepton, jets, and missing transverse momentum in pp collisions with the ATLAS detector*, Nuclear and Particle Physics Proceedings **273-275** (2016) 2415 – 2417. 37th International Conference on High Energy Physics (ICHEP).
- [3] ATLAS Collaboration, *ATLAS Run 1 searches for direct pair production of third-generation squarks at the Large Hadron Collider*, Eur. Phys. J. **C75** no. 10, (2015) 510, [arXiv:1506.08616 \[hep-ex\]](#). [Erratum: Eur. Phys. J. **C76**, no.3, 153 (2016)].
- [4] ATLAS Collaboration, *Summary of the ATLAS experiment's sensitivity to supersymmetry after LHC Run 1 - interpreted in the phenomenological MSSM*, JHEP **10** (2015) 134, [arXiv:1508.06608 \[hep-ex\]](#).
- [5] ATLAS Collaboration, M. Aaboud et al., *Search for top squarks in final states with one isolated lepton, jets, and missing transverse momentum in $\sqrt{s}=13$ TeV pp collisions with the ATLAS detector*, [arXiv:1606.03903 \[hep-ex\]](#). Submitted to PRD.
- [6] ATLAS Collaboration, *Search for top squarks in final states with one isolated lepton, jets, and missing transverse momentum in $\sqrt{s}=13$ TeV pp collisions with ATLAS data*, ATLAS-CONF-2016-050, CERN, Geneva, Jul, 2016, <http://cds.cern.ch/record/2206132>.
- [7] Y. Abulaiti, Licentiate thesis, <http://su.diva-portal.org/smash/get/diva2:731279/FULLTEXT01.pdf>.
- [8] S. Novaes, *Standard model: An Introduction*, [arXiv:hep-ph/0001283 \[hep-ph\]](#).

- [9] D. Roy, *Basic constituents of matter and their interactions: A Progress report*, arXiv:hep-ph/9912523 [hep-ph].
- [10] B. Martin and G. Shaw, *Particle Physics*. John Wiley & Sons Ltd, third ed., 2008.
- [11] F. Mandl and G. Shaw, *Quantum Field Theory*. John Wiley & Sons Ltd, second ed., 2010.
- [12] Particle Data Group Collaboration, K. A. Olive et al., *Review of Particle Physics*, Chin. Phys. **C38** (2014) 090001.
- [13] O. Cremonesi, *Neutrino masses*, PoS **EPS-HEP2013** (2014) 146.
- [14] K. Cahill, *Example of Color Screening*, Phys. Rev. Lett. **41** (1978) 599–601.
- [15] ATLAS Collaboration, *Observation of a new particle in the search for the Standard Model Higgs boson with the ATLAS detector at the LHC*, Phys.Lett. **B716** (2012) 1–29, arXiv:1207.7214 [hep-ex].
- [16] CMS Collaboration, *Observation of a new boson at a mass of 125 GeV with the CMS experiment at the LHC*, Phys.Lett. **B716** (2012) 30–61, arXiv:1207.7235 [hep-ex].
- [17] A. Salam and J. Ward, *Electromagnetic and weak interactions*, Physics Letters **13** no. 2, (1964) 168 – 171.
- [18] P. W. Higgs, *Broken Symmetries and the Masses of Gauge Bosons*, Phys. Rev. Lett. **13** (1964) 508–509.
- [19] F. Englert and R. Brout, *Broken Symmetry and the Mass of Gauge Vector Mesons*, Phys. Rev. Lett. **13** (1964) 321–323.
- [20] G. Bertone, D. Hooper, and J. Silk, *Particle dark matter: Evidence, candidates and constraints*, Phys.Rept. **405** (2005) 279–390, arXiv:hep-ph/0404175 [hep-ph].
- [21] G. 't Hooft, "Naturalness, Chiral Symmetry and Spontaneous Chiral Symmetry Breaking". In 't Hooft, G. *Recent Developments in Gauge Theories*. (Plenum, New York, 1980).
- [22] S. Weinberg, *Implications of Dynamical Symmetry Breaking*, Phys. Rev. **D13** (1976) 974–996.
- [23] E. Gildener, *Gauge Symmetry Hierarchies*, Phys. Rev. **D14** (1976) 1667.
- [24] S. Weinberg, *Implications of Dynamical Symmetry Breaking: An Addendum*, Phys. Rev. **D19** (1979) 1277–1280.

- [25] L. Susskind, *Dynamics of Spontaneous Symmetry Breaking in the Weinberg-Salam Theory*, Phys. Rev. **D20** (1979) 2619–2625.
- [26] S. Dimopoulos and H. Georgi, *Softly Broken Supersymmetry and SU(5)*, Nucl. Phys. **B193** (1981) 150.
- [27] E. Witten, *Dynamical Breaking of Supersymmetry*, Nucl. Phys. **B188** (1981) 513.
- [28] M. Dine, W. Fischler, and M. Srednicki, *Supersymmetric Technicolor*, Nucl. Phys. **B189** (1981) 575–593.
- [29] S. Dimopoulos and S. Raby, *Supercolor*, Nucl. Phys. **B192** (1981) 353.
- [30] N. Sakai, *Naturalness in Supersymmetric Guts*, Zeit. Phys. **C11** (1981) 153.
- [31] R. Kaul and P. Majumdar, *Cancellation of Quadratically Divergent Mass Corrections in Globally Supersymmetric Spontaneously Broken Gauge Theories*, Nucl. Phys. **B199** (1982) 36.
- [32] H. Miyazawa, *Baryon Number Changing Currents*, Prog. Theor. Phys. **36** (6) (1966) 1266–1276.
- [33] P. Ramond, *Dual Theory for Free Fermions*, Phys. Rev. **D3** (1971) 2415–2418.
- [34] Yu. A. Golfand and E. P. Likhtman, *Extension of the Algebra of Poincare Group Generators and Violation of p Invariance*, JETP Lett. **13** (1971) 323–326. [Pisma Zh. Eksp. Teor. Fiz. 13,452(1971)].
- [35] A. Neveu and J. H. Schwarz, *Factorizable dual model of pions*, Nucl. Phys. **B31** (1971) 86–112.
- [36] A. Neveu and J. H. Schwarz, *Quark Model of Dual Pions*, Phys. Rev. **D4** (1971) 1109–1111.
- [37] J. Gervais and B. Sakita, *Field theory interpretation of supergauges in dual models*, Nucl. Phys. **B34** (1971) 632–639.
- [38] D. V. Volkov and V. P. Akulov, *Is the Neutrino a Goldstone Particle?*, Phys. Lett. **B46** (1973) 109–110.
- [39] J. Wess and B. Zumino, *A Lagrangian Model Invariant Under Supergauge Transformations*, Phys. Lett. **B49** (1974) 52.
- [40] J. Wess and B. Zumino, *Supergauge Transformations in Four-Dimensions*, Nucl. Phys. **B70** (1974) 39–50.
- [41] S. P. Martin, *A Supersymmetry primer*, arXiv:hep-ph/9709356v6 [hep-ph].

- [42] K. Rolbiecki, J. Tattersall, and G. Moortgat-Pick, *Towards Measuring the Stop Mixing Angle at the LHC*, Eur.Phys.J. **C71** (2011) 1517, arXiv:0909.3196 [hep-ph].
- [43] H. Goldberg, *Constraint on the photino mass from cosmology*, Phys. Rev. Lett. **50** (1983) 1419.
- [44] J. Ellis, J. Hagelin, D. Nanopoulos, K. Olive, and M. Srednicki, *Supersymmetric relics from the big bang*, Nucl. Phys. **B238** (1984) 453–476.
- [45] R. Barbieri and G. Giudice, *Upper Bounds on Supersymmetric Particle Masses*, Nucl.Phys. **B306** (1988) 63.
- [46] B. de Carlos and J. Casas, *One loop analysis of the electroweak breaking in supersymmetric models and the fine tuning problem*, Phys.Lett. **B309** (1993) 320–328, arXiv:hep-ph/9303291 [hep-ph].
- [47] A. H. Chamseddine, R. Arnowitt, and P. Nath, *Locally Supersymmetric Grand Unification*, Phys. Rev. Lett. **49** (1982) 970.
- [48] G. L. Kane, C. F. Kolda, L. Roszkowski, and J. D. Wells, *Study of constrained minimal supersymmetry*, Phys. Rev. **D49** (1994) 6173–6210.
- [49] 2015. LEP SUSY Working Group (Aleph, Delphi, L3, Opal), Notes lepsusywg/01-03.1 and 04-02.1. (2004) Accessed 20 Oct, <http://lepsusy.web.cern.ch/lepsusy/>.
- [50] ALEPH Collaboration, A. Heister et al., *Absolute mass lower limit for the lightest neutralino of the MSSM from e^+e^- data at \sqrt{S} up to 209 GeV*, Phys.Lett. **B583** (2004) 247–263.
- [51] DELPHI Collaboration, J. Abdallah et al., *Searches for supersymmetric particles in e^+e^- collisions up to 208 GeV and interpretation of the results within the MSSM*, Eur. Phys. J. **C31** (2003) 421–479, arXiv:hep-ex/0311019 [hep-ex].
- [52] L3 Collaboration, M. Acciarri et al., *Search for charginos and neutralinos in e^+e^- collisions at $\sqrt{S} = 189$ GeV*, Phys. Lett. **B472** (2000) 420–433, arXiv:hep-ex/9910007 [hep-ex].
- [53] OPAL Collaboration, G. Abbiendi et al., *Search for chargino and neutralino production at $\sqrt{S} = 192$ -209 GeV at LEP*, Eur.Phys.J. **C35** (2004) 1–20, arXiv:hep-ex/0401026 [hep-ex].
- [54] MSSM Working Group Collaboration, A. Djouadi et al., *The Minimal supersymmetric standard model: Group summary report*, arXiv:hep-ph/9901246 [hep-ph].

- [55] B. Dumont, F. Guion, J. and S. Kraml, *Phenomenological MSSM in view of the 125 GeV Higgs data*, Phys. Rev. D **89** (2014) 055018.
- [56] M. Cahill-Rowley, J. Hewett, A. Ismail, and T. Rizzo, *pMSSM Studies at the 7, 8 and 14 TeV LHC*, arXiv:1307.8444 [hep-ph].
- [57] J. R. Ellis, K. Enqvist, D. V. Nanopoulos, and F. Zwirner, *Observables in Low-Energy Superstring Models*, Mod.Phys.Lett. **A1** (1986) 57.
- [58] M. Baak, M. Goebel, J. Haller, A. Hoecker, D. Kennedy, R. Kogler, K. Moenig, M. Schott, and J. Stelzer, *The Electroweak Fit of the Standard Model after the Discovery of a New Boson at the LHC*, Eur. Phys. J. **C72** (2012) 2205, arXiv:1209.2716 [hep-ph].
- [59] Heavy Flavor Averaging Group Collaboration, Y. Amhis et al., *Averages of B-Hadron, C-Hadron, and tau-lepton properties as of early 2012*, arXiv:1207.1158 [hep-ex].
- [60] K. De Bruyn, R. Fleischer, R. Knegjens, P. Koppenburg, M. Merk, A. Pellegrino, and N. Tuning, *Probing New Physics via the $B_s^0 \rightarrow \mu^+ \mu^-$ Effective Lifetime*, Phys. Rev. Lett. **109** (2012) 041801, arXiv:1204.1737 [hep-ph].
- [61] LHCb Collaboration, CMS Collaboration, *Observation of the rare $B_s^0 \rightarrow \mu^+ \mu^-$ decay from the combined analysis of CMS and LHCb data*, Nature **522** (2015) 68–72, arXiv:1411.4413 [hep-ex].
- [62] BaBar Collaboration, *A Search for $B^+ \rightarrow \ell^+ \nu_\ell$ Recoiling Against $B^- \rightarrow D^0 \ell^- \bar{\nu} X$* , Phys. Rev. **D81** (2010) 051101, arXiv:0912.2453 [hep-ex].
- [63] Belle Collaboration, *Evidence for $B^- \rightarrow \tau^- \bar{\nu}$ with a Semileptonic Tagging Method*, Phys. Rev. **D82** (2010) 071101, arXiv:1006.4201 [hep-ex].
- [64] Belle Collaboration, *Evidence for $B^- \rightarrow \tau^- \bar{\nu}_\tau$ with a Hadronic Tagging Method Using the Full Data Sample of Belle*, Phys. Rev. Lett. **110** no. 13, (2013) 131801, arXiv:1208.4678 [hep-ex].
- [65] BaBar Collaboration, *Evidence of $B^+ \rightarrow \tau^+ \nu$ decays with hadronic B tags*, Phys. Rev. **D88** no. 3, (2013) 031102, arXiv:1207.0698 [hep-ex].
- [66] T. Aoyama, M. Hayakawa, T. Kinoshita, and M. Nio, *Complete Tenth-Order QED Contribution to the Muon g-2*, Phys. Rev. Lett. **109** (2012) 111808, arXiv:1205.5370 [hep-ph].
- [67] K. Hagiwara, R. Liao, A. D. Martin, D. Nomura, and T. Teubner, *$(g-2)_\mu$ and $\alpha(M_Z^2)$ re-evaluated using new precise data*, J. Phys. **G38** (2011) 085003, arXiv:1105.3149 [hep-ph].

- [68] A. Nyffeler, *Hadronic light-by-light scattering in the muon g-2: A New short-distance constraint on pion-exchange*, Phys. Rev. **D79** (2009) 073012, arXiv:0901.1172 [hep-ph].
- [69] A. Czarnecki, W. J. Marciano, and A. Vainshtein, *Refinements in electroweak contributions to the muon anomalous magnetic moment*, Phys. Rev. **D67** (2003) 073006, arXiv:hep-ph/0212229 [hep-ph]. [Erratum: Phys. Rev.D73,119901(2006)].
- [70] Muon g-2 Collaboration, G. W. Bennett et al., *Measurement of the negative muon anomalous magnetic moment to 0.7 ppm*, Phys. Rev. Lett. **92** (2004) 161802, arXiv:hep-ex/0401008 [hep-ex].
- [71] Muon g-2 Collaboration, G. W. Bennett et al., *Final Report of the Muon E821 Anomalous Magnetic Moment Measurement at BNL*, Phys. Rev. **D73** (2006) 072003, arXiv:hep-ex/0602035 [hep-ex].
- [72] P. J. Mohr, B. N. Taylor, and D. B. Newell, *CODATA Recommended Values of the Fundamental Physical Constants: 2006*, Rev. Mod. Phys. **80** (2008) 633–730, arXiv:0801.0028 [physics.atom-ph].
- [73] B. L. Roberts, *Status of the Fermilab Muon (g-2) Experiment*, Chin. Phys. **C34** (2010) 741–744, arXiv:1001.2898 [hep-ex].
- [74] Planck Collaboration, P. A. R. Ade et al., *Planck 2015 results. XIII. Cosmological parameters*, arXiv:1502.01589 [astro-ph.CO].
- [75] LUX Collaboration, D. S. Akerib et al., *First results from the LUX dark matter experiment at the Sanford Underground Research Facility*, Phys. Rev. Lett. **112** (2014) 091303, arXiv:1310.8214 [astro-ph.CO].
- [76] COUPP Collaboration, E. Behnke et al., *First Dark Matter Search Results from a 4-kg CF₃I Bubble Chamber Operated in a Deep Underground Site*, Phys. Rev. **D86** no. 5, (2012) 052001, arXiv:1204.3094 [astro-ph.CO]. [Erratum: Phys. Rev.D90,no.7,079902(2014)].
- [77] XENON100 Collaboration, E. Aprile et al., *Limits on spin-dependent WIMP-nucleon cross sections from 225 live days of XENON100 data*, Phys. Rev. Lett. **111** no. 2, (2013) 021301, arXiv:1301.6620 [astro-ph.CO].
- [78] C. F. Berger, J. S. Gainer, J. L. Hewett, and T. G. Rizzo, *Supersymmetry Without Prejudice*, JHEP **02** (2009) 023, arXiv:0812.0980 [hep-ph].
- [79] SLD Electroweak Group, DELPHI, ALEPH, SLD, SLD Heavy Flavour Group, OPAL, LEP Electroweak Working Group, L3 Collaboration, S. Schael et al., *Precision electroweak measurements on the Z resonance*, Phys. Rept. **427** (2006) 257–454, arXiv:hep-ex/0509008 [hep-ex].

- [80] LEPSUSYWG, ALEPH, DELPHI, L3 and OPAL experiments note LEPSUSYWG/01-03.1,
<http://lepsusy.web.cern.ch/lepsusy/Welcome.html>.
- [81] ATLAS Collaboration, *SUSY searches with the ATLAS detector*, in Interplay between Particle and Astroparticle physics London, United Kingdom, August 18-22, 2014, arXiv:1412.2784 [hep-ex].
- [82] C. Borschensky, M. Krämer, A. Kulesza, M. Mangano, S. Padhi, T. Plehn, and X. Portell, *Squark and gluino production cross sections in pp collisions at $\sqrt{s} = 13, 14, 33$ and 100 TeV*, Eur. Phys. J. C **74** no. arXiv:1407.5066. MS-TP-14-25. CERN-PH-TH-2014-137. 12, (2014) 3174. 22 p. Comments: 22 pages, 16 figures. arXiv admin note: substantial text overlap with arXiv:1206.2892.
- [83] <https://atlas.web.cern.ch/Atlas/GROUPS/PHYSICS/CombinedSummaryPlots/SUSY/index.html>.
- [84] Lyndon Evans, *The Large Hadron Collider*, New J. Phys. **9** (2007) 335.
- [85] <http://arstechnica.com/science/2010/08/following-protons-on-a-trip-to-and-through-the-lhc/>.
- [86] ATLAS Collaboration, *Luminosity Determination in pp Collisions at $\sqrt{s} = 7$ TeV Using the ATLAS Detector at the LHC*, Eur. Phys. J. C **71** (2011) 1630, arXiv:1101.2185 [hep-ex].
- [87] https://twiki.cern.ch/twiki/bin/view/AtlasPublic/LuminosityPublicResultsRun2#2015_pp_Collisions.
- [88] ATLAS Collaboration, *The ATLAS Experiment at the CERN Large Hadron Collider*, JINST **3** (2008) S08003.
- [89] ATLAS Collaboration, *Studies of the performance of the ATLAS detector using cosmic-ray muons*, Eur. Phys. J. C **71** (2011) 1593, arXiv:1011.6665 [physics.ins-det].
- [90] J. Pequeno, *Event Cross Section in a computer generated image of the ATLAS detector*, CERN-GE-0803022, Mar, 2008.
- [91] <https://en.wikipedia.org/wiki/Pseudorapidity>.
- [92] <http://www.hep.lu.se/atlas/thesis/egede/thesis-node81.html>.
- [93] J. Pequeno, *Computer generated image of the ATLAS inner detector*, CERN-GE-0803014, Mar, 2008.

- [94] M. Capeans, G. Darbo, K. Einsweiler, M. Elsing, T. Flick, M. Garcia-Sciveres, C. Gemme, H. Pernegger, O. Rohne, and R. Vuillermet, *ATLAS Insertable B-Layer Technical Design Report*, CERN-LHCC-2010-013. ATLAS-TDR-19, CERN, Geneva, Sep, 2010.
- [95] A. Miucci, *The ATLAS Insertable B-Layer project*, Journal of Instrumentation **9** no. 02, (2014) C02018.
- [96] <https://gordonwatts.wordpress.com/category/trigger/>.
- [97] GEANT4 Collaboration, S. Agostinelli et al., *GEANT4: A simulation toolkit*, Nucl. Instrum. Meth. **A506** (2003) 250–303.
- [98] S. Frixione and B. R. Webber, *Matching NLO QCD computations and parton shower simulations*, JHEP **0206** (2002) 029, arXiv:hep-ph/0204244 [hep-ph].
- [99] J. M. Butterworth, J. R. Forshaw, and M. H. Seymour, *Multiparton interactions in photoproduction at HERA*, Z. Phys. **C72** (1996) 637–646, arXiv:hep-ph/9601371 [hep-ph].
- [100] T. Sjostrand, S. Mrenna, and P. Z. Skands, *PYTHIA 6.4 Physics and Manual*, JHEP **0605** (2006) 026, arXiv:hep-ph/0603175 [hep-ph].
- [101] S. Frixione, P. Nason, and C. Oleari, *Matching NLO QCD computations with Parton Shower simulations: the POWHEG method*, JHEP **11** (2007) 070, arXiv:0709.2092 [hep-ph].
- [102] M. Czakon, P. Fiedler, and A. Mitov, *Total Top-Quark Pair-Production Cross Section at Hadron Colliders Through $O(\alpha_s^4)$* , Phys. Rev. Lett. **110** (2013) 252004, arXiv:1303.6254 [hep-ph].
- [103] M. Czakon and A. Mitov, *NNLO corrections to top pair production at hadron colliders: the quark-gluon reaction*, JHEP **01** (2013) 080, arXiv:1210.6832 [hep-ph].
- [104] M. Czakon and A. Mitov, *NNLO corrections to top-pair production at hadron colliders: the all-fermionic scattering channels*, JHEP **12** (2012) 054, arXiv:1207.0236 [hep-ph].
- [105] P. Bärnreuther, M. Czakon, and A. Mitov, *Percent Level Precision Physics at the Tevatron: First Genuine NNLO QCD Corrections to $q\bar{q} \rightarrow t\bar{t} + X$* , Phys. Rev. Lett. **109** (2012) 132001, arXiv:1204.5201 [hep-ph].

- [106] M. Cacciari, M. Czakon, M. Mangano, A. Mitov, and P. Nason, *Top-pair production at hadron colliders with next-to-next-to-leading logarithmic soft-gluon resummation*, Phys. Lett. **B710** (2012) 612–622, arXiv:1111.5869 [hep-ph].
- [107] M. Czakon and A. Mitov, *Top++: A Program for the Calculation of the Top-Pair Cross-Section at Hadron Colliders*, Comput. Phys. Commun. **185** (2014) 2930, arXiv:1112.5675 [hep-ph].
- [108] ATLAS Collaboration, *Measurement of top-quark pair differential cross-sections in the $l+jets$ channel in pp collisions at $\sqrt{s} = 7$ TeV using the ATLAS detector*, ATLAS-CONF-2013-099, CERN, Geneva, Sep, 2013, <http://cds.cern.ch/record/1600778>.
- [109] B. P. Kersevan and E. Richter-Was, *The Monte Carlo event generator AcerMC versions 2.0 to 3.8 with interfaces to PYTHIA 6.4, HERWIG 6.5 and ARIADNE 4.1*, Comput. Phys. Commun. **184** (2013) 919–985, arXiv:hep-ph/0405247 [hep-ph].
- [110] J. Alwall, M. Herquet, F. Maltoni, O. Mattelaer, and T. Stelzer, *MadGraph 5 : Going Beyond*, JHEP **06** (2011) 128, arXiv:1106.0522 [hep-ph].
- [111] T. Gleisberg, S. Hoeche, F. Krauss, M. Schonherr, S. Schumann, F. Siegert, and J. Winter, *Event generation with SHERPA 1.1*, JHEP **02** (2009) 007, arXiv:0811.4622 [hep-ph].
- [112] S. Catani, L. Cieri, G. Ferrera, D. de Florian, and M. Grazzini, *Vector boson production at hadron colliders: a fully exclusive QCD calculation at NNLO*, Phys. Rev. Lett. **103** (2009) 082001, arXiv:0903.2120 [hep-ph].
- [113] J. M. Campbell and R. K. Ellis, *An Update on vector boson pair production at hadron colliders*, Phys. Rev. **D60** (1999) 113006, arXiv:hep-ph/9905386 [hep-ph].
- [114] A. D. Martin, W. J. Stirling, R. S. Thorne, and G. Watt, *Parton distributions for the LHC*, Eur. Phys. J. **C63** (2009) 189–285, arXiv:0901.0002 [hep-ph].
- [115] H.-L. Lai, M. Guzzi, J. Huston, Z. Li, P. M. Nadolsky, J. Pumplin, and C. P. Yuan, *New parton distributions for collider physics*, Phys. Rev. **D82** (2010) 074024, arXiv:1007.2241 [hep-ph].
- [116] J. Pumplin, D. R. Stump, J. Huston, H. L. Lai, P. M. Nadolsky, and W. K. Tung, *New generation of parton distributions with uncertainties from global QCD analysis*, JHEP **07** (2002) 012, arXiv:hep-ph/0201195 [hep-ph].

- [117] E. Re, *Single-top Wt-channel production matched with parton showers using the POWHEG method*, Eur. Phys. J. **C71** (2011) 1547, arXiv:1009.2450 [hep-ph].
- [118] S. Frixione, P. Nason, and G. Ridolfi, *A Positive-weight next-to-leading-order Monte Carlo for heavy flavour hadroproduction*, JHEP **09** (2007) 126, arXiv:0707.3088 [hep-ph].
- [119] R. Frederix, E. Re, and P. Torrielli, *Single-top t-channel hadroproduction in the four-flavour scheme with POWHEG and aMC@NLO*, JHEP **09** (2012) 130, arXiv:1207.5391 [hep-ph].
- [120] S. Alioli, P. Nason, C. Oleari, and E. Re, *NLO single-top production matched with shower in POWHEG: s- and t-channel contributions*, JHEP **09** (2009) 111, arXiv:0907.4076 [hep-ph]. [Erratum: JHEP02,011(2010)].
- [121] T. Sjostrand, S. Mrenna, and P. Z. Skands, *PYTHIA 6.4 Physics and Manual*, JHEP **05** (2006) 026, arXiv:hep-ph/0603175 [hep-ph].
- [122] T. Sjostrand, S. Mrenna, and P. Z. Skands, *PYTHIA 6.4 Physics and Manual*, JHEP **05** (2006) 026, arXiv:hep-ph/0603175 [hep-ph].
- [123] J. A. Aguilar-Saavedra, *Identifying top partners at LHC*, JHEP **11** (2009) 030, arXiv:0907.3155 [hep-ph].
- [124] L. Lonnblad and S. Prestel, *Matching Tree-Level Matrix Elements with Interleaved Showers*, JHEP **03** (2012) 019, arXiv:1109.4829 [hep-ph].
- [125] R. D. Ball et al., *Parton distributions with LHC data*, Nucl. Phys. **B867** (2013) 244–289, arXiv:1207.1303 [hep-ph].
- [126] M. Bahr et al., *Herwig++ Physics and Manual*, Eur. Phys. J. **C58** (2008) 639–707, arXiv:0803.0883 [hep-ph].
- [127] J. A. Aguilar-Saavedra, *Protos - PROgram for TOP Simulations*, <http://jaguilar.web.cern.ch/jaguilar/protos/>.
- [128] ATLAS Collaboration, *Performance of the ATLAS Inner Detector Track and Vertex Reconstruction in the High Pile-Up LHC Environment*, ATLAS-CONF-2012-042, CERN, Geneva, Mar, 2012, <http://cds.cern.ch/record/1435196>.
- [129] ATLAS Collaboration, *Early Inner Detector Tracking Performance in the 2015 data at $\sqrt{s} = 13$ TeV*, ATL-PHYS-PUB-2015-051, CERN, Geneva, Dec, 2015, <http://cds.cern.ch/record/2110140>.

- [130] G. Piacquadio, K. Prokofiev, and A. Wildauer, *Primary vertex reconstruction in the ATLAS experiment at LHC*, J.Phys.Conf.Ser. **119** (2008) 032033.
- [131] F. Meloni, *Track and vertex reconstruction in the ATLAS experiment*, Nuclear Instruments and Methods in Physics Research Section A: Accelerators, Spectrometers, Detectors and Associated Equipment **718** no. 0, (2013) 334 – 335. Proceedings of the 12th Pisa Meeting on Advanced Detectors La Biodola, Isola d’Elba, Italy, May 20-26, 2012.
- [132] M. Cacciari, G. P. Salam, and G. Soyez, *The Anti-k(t) jet clustering algorithm*, JHEP **0804** (2008) 063, arXiv:0802.1189 [hep-ph].
- [133] A. Schwartzman, *Jet energy calibration at the LHC*, Int. J. Mod. Phys. **A30** no. 31, (2015) 1546002, arXiv:1509.05459 [hep-ex].
- [134] ATLAS Collaboration, *Performance of jet substructure techniques for large-R jets in proton-proton collisions at $\sqrt{s} = 7$ TeV using the ATLAS detector*, JHEP **1309** (2013) 076, arXiv:1306.4945 [hep-ex].
- [135] ATLAS Collaboration, *Commissioning of the ATLAS high-performance b-tagging algorithms in the 7 TeV collision data*, ATLAS-CONF-2011-102, CERN, Geneva, Jul, 2011, <http://cds.cern.ch/record/1369219>.
- [136] ATLAS Collaboration, *Expected performance of the ATLAS b-tagging algorithms in Run-2*, ATL-PHYS-PUB-2015-022, CERN, Geneva, Jul, 2015, <http://cds.cern.ch/record/2037697>.
- [137] ATLAS Collaboration, *Electron performance measurements with the ATLAS detector using the 2010 LHC proton-proton collision data*, Eur.Phys.J. **C72** (2012) 1909, arXiv:1110.3174 [hep-ex].
- [138] ATLAS Collaboration, *Electron identification measurements in ATLAS using $\sqrt{s} = 13$ TeV data with 50 ns bunch spacing*, ATL-PHYS-PUB-2015-041, CERN, Geneva, Sep, 2015, <http://cds.cern.ch/record/2048202>.
- [139] ATLAS Collaboration, *Muon reconstruction performance of the ATLAS detector in proton-proton collision data at $\sqrt{s}=13$ TeV*, Eur. Phys. J. C **76** no. arXiv:1603.05598. CERN-EP-2016-033, (2016) 292. 45 p.
- [140] ATLAS Collaboration, *Performance of the Reconstruction and Identification of Hadronic Tau Decays in ATLAS with 2011 Data*, ATLAS-CONF-2012-142, CERN, Geneva, Oct, 2012, <http://cds.cern.ch/record/1485531>.
- [141] ATLAS Collaboration, *Reconstruction, Energy Calibration, and Identification of Hadronically Decaying Tau Leptons in the ATLAS Experiment for Run-2 of the LHC*, ATL-PHYS-PUB-2015-045, CERN, Geneva, Nov, 2015, <https://cds.cern.ch/record/2064383>.

- [142] ATLAS Collaboration, *Measurement of the inclusive isolated prompt photon cross section in pp collisions at $\sqrt{s} = 7$ TeV with the ATLAS detector*, Phys. Rev. **D83** (2011) 052005, arXiv:1012.4389 [hep-ex].
- [143] ATLAS Collaboration, *Expected photon performance in the ATLAS experiment*, ATL-PHYS-PUB-2011-007, CERN, Geneva, Apr, 2011, <http://cds.cern.ch/record/1345329>.
- [144] K. Grimm, E. Guido, F. Meloni, S. P. Griso, K. Prokofiev, M. Rudolph, and A. Wildauer, *Methods to quantify the performance of the primary vertex reconstruction in the ATLAS experiment under high luminosity conditions*, Journal of Physics: Conference Series **396** no. 2, (2012) 022041.
- [145] G. Cowan, *Statistical Data Analysis*. Oxford University Press, 1998.
- [146] J. Smith, W. L. van Neerven, and J. A. M. Vermaseren, *Transverse Mass and Width of the W Boson*, Phys. Rev. Lett. **50** (1983) 1738–1740.
- [147] B. Nachman and C. G. Lester, *Significance Variables*, Phys.Rev. **D88** (2013) 075013, arXiv:1303.7009 [hep-ph].
- [148] Y. Bai, H.-C. Cheng, J. Gallicchio, and J. Gu, *Stop the Top Background of the Stop Search*, JHEP **1207** (2012) 110, arXiv:1203.4813 [hep-ph].
- [149] M. L. Graesser and J. Shelton, *Hunting Mixed Top Squark Decays*, Phys.Rev.Lett. **111** no. 12, (2013) 121802, arXiv:1212.4495 [hep-ph].
- [150] G. J. Besjeses, M. Baak, D. Côté, A. Koutsman, J. M. Lorenz, and D. Short, *HistFitter: a flexible framework for statistical data analysis*, Journal of Physics: Conference Series **664** no. 7, (2015) 072004.
- [151] ATLAS Collaboration, *Search for supersymmetry in final states with jets, missing transverse momentum and one isolated lepton in $\sqrt{s} = 7$ TeV pp collisions using 1 fb^{-1} of ATLAS data*, Phys. Rev. **D85** no. 1, (2012) 012006, arXiv:1109.6606 [hep-ex]. [Erratum: Phys. Rev.D87,099903(2013)].
- [152] A. Read, *Presentation of search results: the CLs technique*, Journal of Physics G: Nucl. Part. Phys. **28** (2002) 2693–2704.
- [153] ATLAS Collaboration, *Jet energy measurement with the ATLAS detector in proton-proton collisions at $\sqrt{s} = 7$ TeV*, Eur. Phys. J. **C73** no. 3, (2013) 2304, arXiv:1112.6426 [hep-ex].
- [154] ATLAS Collaboration, *Jet energy measurement and its systematic uncertainty in proton-proton collisions at $\sqrt{s} = 7$ TeV with the ATLAS detector*, Eur. Phys. J. **C75** (2015) 17, arXiv:1406.0076 [hep-ex].

- [155] ATLAS Collaboration, *Jet energy resolution in proton-proton collisions at $\sqrt{s} = 7$ TeV recorded in 2010 with the ATLAS detector*, Eur. Phys. J. **C73** no. 3, (2013) 2306, arXiv:1210.6210 [hep-ex].
- [156] ATLAS Collaboration, *Jet mass and substructure of inclusive jets in $\sqrt{s} = 7$ TeV pp collisions with the ATLAS experiment*, JHEP **05** (2012) 128, arXiv:1203.4606 [hep-ex].
- [157] ATLAS Collaboration, *Measurement of the Mistag Rate with 5 fb^{-1} of Data Collected by the ATLAS Detector*, ATLAS-CONF-2012-040, CERN, Geneva, Mar, 2012, <http://cds.cern.ch/record/1435194>.
- [158] ATLAS Collaboration, *Calibration of b -tagging using dileptonic top pair events in a combinatorial likelihood approach with the ATLAS experiment*, ATLAS-CONF-2014-004, CERN, Geneva, Feb, 2014, <http://cds.cern.ch/record/1664335>.
- [159] ATLAS Collaboration, *Measurement of the b -tag Efficiency in a Sample of Jets Containing Muons with 5 fb^{-1} of Data from the ATLAS Detector*, ATLAS-CONF-2012-043, CERN, Geneva, Mar, 2012, <http://cds.cern.ch/record/1435197>.
- [160] ATLAS Collaboration, *b -jet tagging calibration on c -jets containing D^{*+} mesons*, ATLAS-CONF-2012-039, CERN, Geneva, Mar, 2012, <http://cds.cern.ch/record/1435193>.
- [161] M. Botje et al., *The PDF4LHC Working Group Interim Recommendations*, arXiv:1101.0538 [hep-ph].
- [162] ATLAS Collaboration, *Measurement of the cross-section for W boson production in association with b -jets in pp collisions at $\sqrt{s} = 7$ TeV with the ATLAS detector*, JHEP **06** (2013) 084, arXiv:1302.2929 [hep-ex].
- [163] N. Kidonakis, *Next-to-next-to-leading-order collinear and soft gluon corrections for t -channel single top quark production*, Phys. Rev. **D83** (2011) 091503, arXiv:1103.2792 [hep-ph].
- [164] N. Kidonakis, *Two-loop soft anomalous dimensions for single top quark associated production with a W^- or H^-* , Phys. Rev. **D82** (2010) 054018, arXiv:1005.4451 [hep-ph].
- [165] N. Kidonakis, *NNLL resummation for s -channel single top quark production*, Phys. Rev. **D81** (2010) 054028, arXiv:1001.5034 [hep-ph].
- [166] J. M. Campbell and R. K. Ellis, *$t\bar{t}W^\pm$ production and decay at NLO*, JHEP **07** (2012) 052, arXiv:1204.5678 [hep-ph].

- [167] M. V. Garzelli, A. Kardos, C. G. Papadopoulos, and Z. Trocsanyi, *$t \bar{t} W^\pm$ and $t \bar{t} Z$ Hadroproduction at NLO accuracy in QCD with Parton Shower and Hadronization effects*, JHEP **11** (2012) 056, arXiv:1208.2665 [hep-ph].
- [168] J. M. Campbell, R. K. Ellis, and C. Williams, *Vector boson pair production at the LHC*, JHEP **07** (2011) 018, arXiv:1105.0020 [hep-ph].
- [169] M. Kramer, A. Kulesza, R. van der Leeuw, M. Mangano, S. Padhi, T. Plehn, and X. Portell, *Supersymmetry production cross sections in pp collisions at $\sqrt{s} = 7$ TeV*, arXiv:1206.2892 [hep-ph].
- [170] ATLAS Collaboration, *Performance of pile-up mitigation techniques for jets in pp collisions with the ATLAS detector*, Nucl. Instrum. Meth. **A824** (2016) 367–370, arXiv:1510.03823 [hep-ex].
- [171] ATLAS Collaboration, *Jet Calibration and Systematic Uncertainties for Jets Reconstructed in the ATLAS Detector at $\sqrt{s} = 13$ TeV*, ATL-PHYS-PUB-2015-015, CERN, Geneva, Jul, 2015, <http://cds.cern.ch/record/2037613>.
- [172] ATLAS Collaboration, *Simulation of top quark production for the ATLAS experiment at $\sqrt{s} = 13$ TeV*, ATL-PHYS-PUB-2016-004, CERN, Geneva, Jan, 2016, <http://cds.cern.ch/record/2120417>.
- [173] ATLAS Collaboration, *Search for squarks and gluinos in events with isolated leptons, jets and missing transverse momentum at $\sqrt{s} = 8$ TeV with the ATLAS detector*, JHEP **04** (2015) 116, arXiv:1501.03555 [hep-ex].
- [174] ATLAS Collaboration, *Search for new phenomena in final states with an energetic jet and large missing transverse momentum in pp collisions at $\sqrt{s} = 13$ TeV using the ATLAS detector*, arXiv:1604.07773 [hep-ex].
- [175] https://root.cern.ch/root/html/tutorials/roostats/rs_numbercountingutils.C.html.